Inlet and Outlet Shape Design of Natural Circulation Building Ventilation Systems

by

Jacobus Johannes Swiegers

Thesis presented in partial fulfilment of the requirements for the degree of Master of Engineering (Mechanical) in the Faculty of Engineering at Stellenbosch University

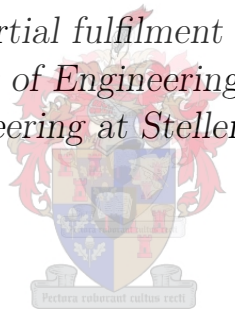

Supervisor: Mr. Robert Thomas Dobson

March 2015

Declaration

By submitting this thesis electronically, I declare that the entirety of the work contained therein is my own, original work, that I am the sole author thereof (save to the extent explicitly otherwise stated), that reproduction and publication thereof by Stellenbosch University will not infringe any third party rights and that I have not previously in its entirety or in part submitted it for obtaining any qualification.

Date: .....

Abstract

Inlet and Outlet Shape Design of Natural Circulation Building Ventilation Systems

J.J. Swiegers

Thesis: MEng (Mech)

Increased awareness of environmental problems has awakened interest in renewable energy systems. Natural ventilation systems are especially of interest, as people spend most of their time indoors. Indoor air quality is an important consideration when human health and occupant comfort is to be maintained.

This study focusses on determining the best inlet and outlet shape for a natural ventilation system from a chosen set of configurations. The inlet and outlet configurations were tested on a PDEC (Passive Downdraught Evaporative Cooling) shaft and solar chimney. The PDEC incorporated an evaporative cartridge made from cotton cloth. Independent models of the PDEC and solar chimney were built in a thermally controlled space where the configurations were tested at different wind speeds. The configurations were tested on a wet or dry PDEC shaft and on a hot or cold solar chimney.

One-dimensional finite difference models, accounting for some two-dimensional effects in the evaporative cartridge, of the cartridge and solar chimney were developed. CFD (Computational Fluid Dynamics) models were further constructed in FLUENT®, simulating operating conditions for each inlet and outlet test. The CFD models were constructed to obtain numerical comparisons for the experimental data. The ability of the one-dimensional and CFD models to predict the performance of the PDEC and solar chimney were investigated.

The results indicated that an inlet configuration called a TFI (Turbine Fan Inlet) performed the best at the tested wind speeds. The TFI was further able to significantly increase volumetric flow rate in the PDEC shaft for the dry evaporative cartridge tests. The outlet that performed best under the tests is a Windmaster Tornado Wind Turbine, or *Whirlybird*, which is a commercially available configuration.

The one-dimensional models were not able to accurately predict conditions during start-up. The CFD models were highly accurate in predicting the

experimental values. It is recommended that a two-dimensional theoretical model be developed to better predict start-up conditions.

Uittreksel

Inlaat en Uitlaat Vorm Ontwerp van Natuurlike Sirkulasie Gebou Ventilasie Sisteme

("Inlet and Outlet Shape Design of Natural Circulation Building Ventilation Systems")

J.J. Swiegers

Tesis: MIng (Meg)

Verhoogde bewustheid van omgewings probleme het belangstelling in hernubare energie stelsels ontwaak. Natuurlike ventilasie stelsels is veral van belang, sedert mense die meeste van hul tyd binnenshuis spandeer. Binnenshuise lug kwaliteit is 'n belangrike oorweging wanneer menslike gesondheid en insittendes se gemak in stand gehou moet word.

Hierdie studie fokus op die bepaling van die beste inlaat en uitlaat vorm van 'n gekose stel konfigurasies vir 'n natuurlike ventilasie-stelsel. Die inlaat- en uitlaat-konfigurasies is op 'n PDEC (Passive Downdraught Evaporative Cooling) skag en sonkrag skoorsteen getoets. Die PDEC het 'n verdampings doek, gemaak van katoen, ingesluit. Onafhanklike modelle van die PDEC en sonkrag skoorsteen is in 'n termies-beheerde ruimte en die konfigurasies is by 'n onveranderende wind spoed getoets. Die konfigurasies is op 'n nat of droog PDEC skag en op 'n warm of koue son skoorsteen getoets.

Een-dimensionele eindige verskil modelle, wat sommige twee-dimensionele effekte in ag neem in die verdampings doek, van die doek en sonkrag skoorsteen is ontwikkel. CFD (Computational Fluid Dynamics) modelle is verder gebou in FLUENT®, wat die werkstoestande vir elke inlaat en uitlaat toets simuleer. Die CFD modelle is ontwikkel om die eksperimentele data met numeriese waardes te vergelyk. Die vermoë van die een-dimensionele en CFD modelle om die verrigting van die PDEC en sonkrag skoorsteen te voorspel, is ondersoek.

Die resultate dui daarop dat 'n inlaat opset genoem TFI (Turbine Fan Inlet) die beste vaar by die elke getoetsde wind spoed. Die TFI was verder in staat om die volumetriese vloeitempo in die PDEC skag aansienlik te verhoog vir die toetse met 'n droë verdamping doek. Die uitlaat wat die beste presteer

het in die toetse is 'n Windmaster Tornado Wind Turbine, of *Whirlybird*, wat 'n kommersieel beskikbare konfigurasie is.

Die een-dimensionele modelle was nie in staat om die toestande tydens die begin-fase akkuraat te voorspel nie. Die CFD modelle was hoogs akkuraat in die voorspelling van die eksperimentele waardes. Dit word aanbeveel dat 'n twee-dimensionele teoretiese model ontwikkel word om die toestande tydens begin-fase beter te voorspel.

Acknowledgements

I would like to express my sincere gratitude to Mr R.T. Dobson for his support throughout the entire duration of this project.

Dedications

Hierdie tesis word opgedra aan Anina en aan my ouers, wat my bygestaan het gedurende die projek.

Contents

List of Figures

List of Tables

Nomenclature

Constants

g =	$9.81\,\mathrm{m/s^2}$

Variables

A	Area, m^2
A_s	Surface area, m^2
A_x	Cross sectional area, m^2
a	Outside radius, m
b	Inside radius, m
c_v	Specific heat at constant volume J/kgK
C	Roughness coefficient
D	Diameter, m
D_{va}	Mass diffusivity of water vapour in air, m^2/s
Eff	Efficiency
F	Force N
f	Friction factor
G	Volumetric flow rate, m^3/s
Gr	Grashof number
h	Specific enthalpy, J/kg
h_{ht}	Convection heat transfer coefficient, $\mathrm{W/m^2K}$
h_{mt}	Mass transfer coefficient, m/s
k	Coverage factor
k	Loss coefficient
k	Thermal conductivity, W/mK
L	Length, m
m	Mass, kg
$\dot{m}$	Mass flow rate, kg/s
Nu	Nusselt number
P	Pressure, Pa

p	Perimeter, m
$\dot{Q}$	Heat transfer rate, W
Pr	Prandtl number
R	Thermal resistance, K/W
Re	Reynolds number
Sc	Schmidt number
Sh	Sherwood number
T	Temperature, ^{o}C
t	Time, s
v	Velocity, m/s
V	Volume, m^3

Greek Symbols

ζ	Reynolds number correction factor
θ	Angle
μ	Dynamic viscosity, kg/ms
ρ	Density, kg/m^3
τ	Shear stress, N/m^2
ϕ	Relative humidity
σ	Standard deviation

Vectors and Tensors

$\bar{V}$	Average velocity, m/s

Superscripts

new	Property at t + Δt
old	Property at t

Subscripts

a	Air
acr	Acrylic
avg	Average
$conf$	Configuration
$conv$	Convection
c	Contact
db	Dry bulb
eq	Equivalent

e	Environment or Exit
ht	Heat transfer
in	Incoming
i	Inlet or Inside
i	Lengthwise control volume
j	Radial control volume
l	Liquid
m	Mixture
max	Maximum
ms	Mass transfer
oe	Open ended
out	Outgoing
o	Outside
p	Pipe
pr	Probe
rel	Relative
sat	Saturated
v	Vapour
ven	Vendor
w	Water
w	Wind
wb	Wet bulb

Abbreviations

CFD	Computational Fluid Dynamics
DSI	Dobson Swiegers Inlet
DSO	Dobson Swiegers Outlet
HVAC	Heating, Ventilation and Air-conditioning
UDF	User Defined Function
MRF	Multiple Reference Frame
SAWS	South African Weather Service
Stdev,σ	Standard Deviation
PDEC	Passive Downdraught Evaporative Cooling
PV	Photovoltaic
SCAPDEC	Solar Chimney Augmented Passive Downdraught Evaporative Cooling
TFI	Turbine Fan Inlet
TFO	Turbine Fan Outlet

1 Introduction

1.1 Project Inception

Buildings account for about 40 percent of energy consumption in most developed countries and an even higher percentage in developing countries, as stated by Elzaidabi (2008). Elzaidabi found that a major energy demand in the domestic sector includes heating and cooling of buildings. The domestic sector includes the household, business and government sectors in which the energy loads on buildings is largely due to the amount of energy required to operate the air-conditioning systems. Air-conditioning systems often use conventional HVAC (heating, ventilation, and air-conditioning) systems to achieve thermal tempering. Natural ventilation differs from HVAC systems as it uses natural driving forces, such as wind pressure and buoyancy, to move air through an enclosed space. A study by Allard and Ghiaus (2005) states that in arid countries natural ventilation systems have been incorporated into buildings to protect occupants from extreme outdoor conditions, while providing a good indoor environment. An arid country is generally associated with abundant solar resources.

The use of natural ventilation systems to achieve thermal tempering in building structures is therefore an existing strategy in air-conditioning systems. This strategy is however not yet capable of challenging HVAC systems on a global scale as the approach is not efficient enough and often requires external power to operate pumps and fans. It is therefore a challenge to optimise this system to become viable, both economically and performance-wise.

1.2 Project Background

The number of studies on natural ventilation systems have increased in the past decade. These studies mainly focus on a particular aspect of a natural ventilation system and are generally not aimed to optimise the efficiency of the entire system. le Grange (2009) researched the feasibility of using evaporative pads made from porous material in a PDEC (Passive Downdraught Evaporative Cooling) tower. Botha (2010) researched the feasibility of a SCAPDEC (Solar Chimney Augmented Passive Downdraught Evaporative Cooling) sys-

tem and compiled design guidelines for such a system. It was found that the system was insensitive to changes in ambient wind speed and air had to be forced into the system in order to obtain reasonable results. It was suggested that further research be done on the inlet and outlet of the SCAPDEC system in order to maximise airflow through the system for a wider range of environmental conditions.

Figure 1.1 shows the major components of the SCAPDEC system. Swiegers (2012) conducted a study to optimise the inlet and outlet shape design for a SCAPDEC system. In this study, open-ended inlet and outlet configurations were tested and compared with two conventional designs and a new design to optain an optimised shape for each case. These new designs were named the DSI (Dobson Swiegers Inlet) and DSO (Dobson Swiegers Outlet) configurations, as shown in Figure 1.2.

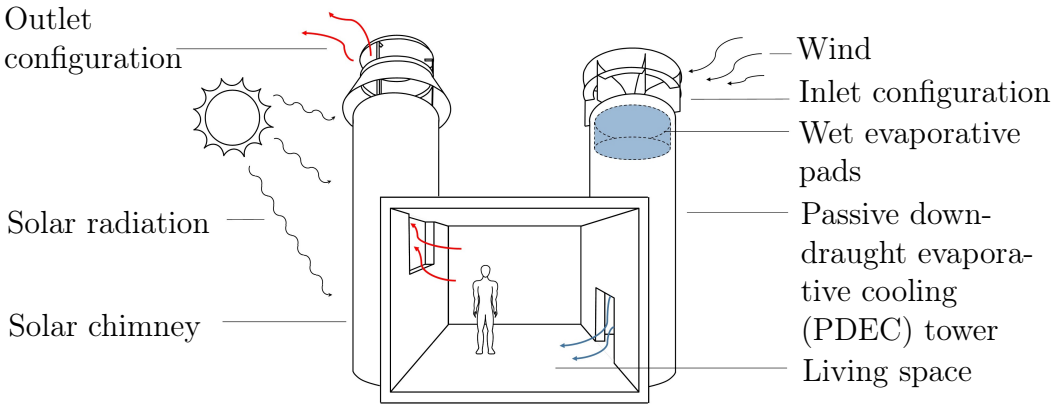

Figure 1.1: Layout of Solar Chimney Augmented Passive Evaporative Downdraught Cooling (SCAPDEC)

Swiegers (2012) tested the configurations in a wind tunnel testing setup and determined energy loss coefficients for each configuration. The loss coefficients were then incorporated into a one-dimensional theoretical model that was developed in Fortran (Fortran (2014)). The theoretical model was then compared with experimental results obtained from a laboratory SCAPDEC system.

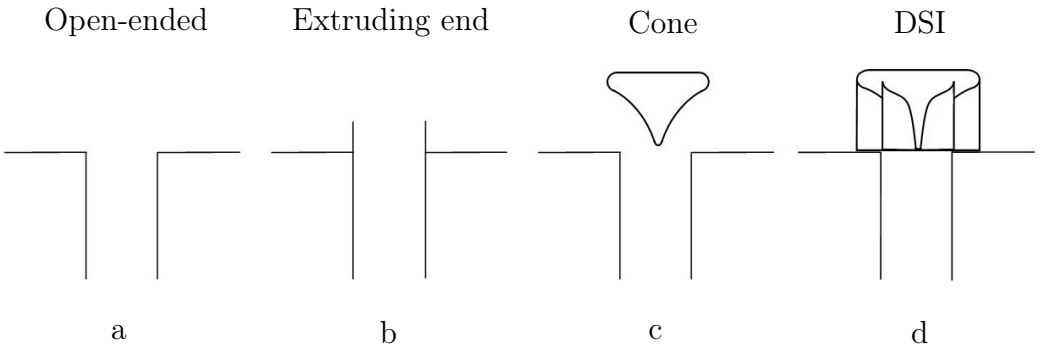

(a) Inlet Configurations

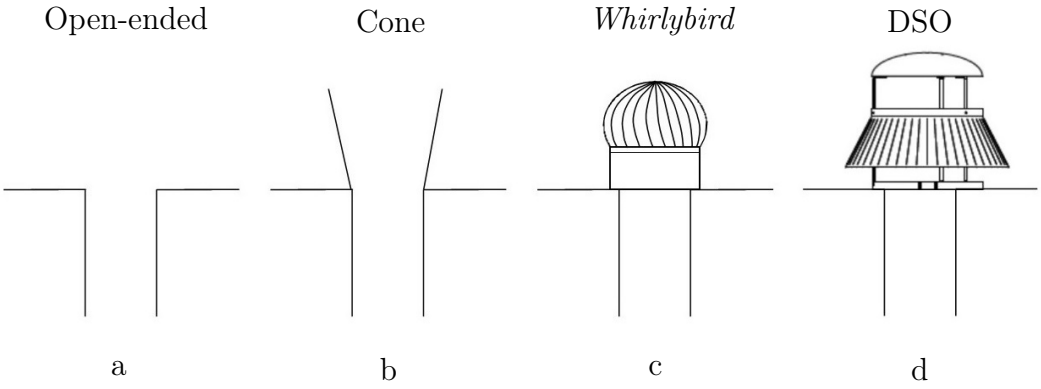

(b) Outlet Configurations

Figure 1.2: Configurations tested by Swiegers (2012)

Figure 1.3 shows the laboratory SCAPDEC model that was used to validate the theoretical model. It was concluded that the one-dimensional model was adequate in predicting system flow rates and temperatures for a small scale system. The model was however not accurate in predicting results when the diameters of the laboratory model increased. The model was also inadequate in that it was not capable of predicting accurate results in a multidirectional flow field. This was deemed acceptable as the volumetric flow rate could still be captured accurately on the laboratory model. The model could not predict entry effects due to wind, as this occurred in a multidirectional space. The influence of the boundary layer was also ignored in the one-dimensional model. It was concluded that further research be done and a CFD (Computational Fluid Dynamics) model be developed to further validate the data.

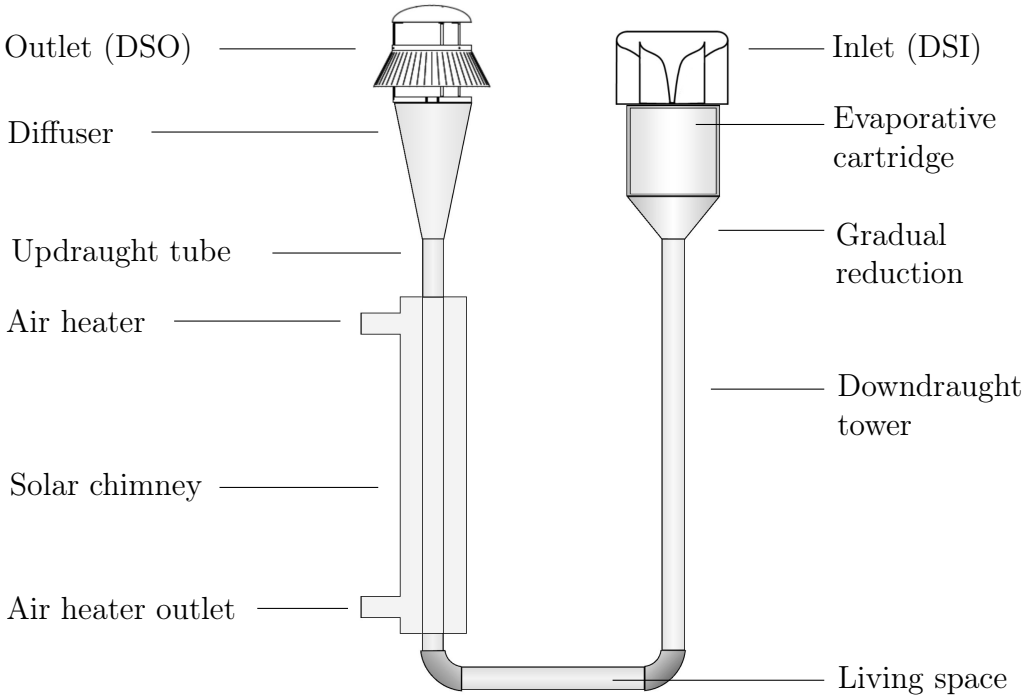

Figure 1.3: SCAPDEC laboratory model layout

1.3 Aims and Methods

This study aimed to theoretically and experimentally determine the best inlet and outlet shape for a SCAPDEC system. This was done by building large-scale PDEC and solar chimney models with similar dimensions. The models were built in a thermally controlled enclosed space, where tests were conducted. The models were limited by the dimensions of the enclosed space. Different inlet and outlet configurations were tested at various wind speeds and operating conditions to determine the best shape. Data was obtained through theoretical models, CFD analysis and experimental tests.

1.4 Objectives

The objetives of this study are to

- determine the best inlet and outlet configuration for a natural ventilation system consisting of a PDEC shaft and solar chimney.
- investigate the ability of a one-dimensional model to predict the performance of a full-scale evaporative cartridge and solar chimney.

- use CFD models to supplement the experimental data and one-dimensional models of a full-scale PDEC shaft and solar chimney for each inlet and outlet configuration.
- suggest an inlet and outlet design suitable for both still and windy conditions.

1.5 Layout of the Thesis

A literature survey is presented in Section 2 to gain an understanding of existing solutions in natural ventilation systems. The theory involved in a one-dimensional evaporative cartridge and solar chimney is then investigated in Section 3. Optimised evaporative cartridge dimensions are then chosen before experimental work is done. The experimental work involved in building a PDEC, solar chimney, and the various inlet and outlet configurations are then discussed in Section 4. The results obtained from the tests conducted on each configuration for the PDEC and solar chimney are then given and compared with theoretical data in Section 5. A discussion and conclusion on the results of the study is then presented in Section 6. Finally in Section 7, recommendations are made for possible further studies.

2 Literature Survey

In this section the results from previous studies and existing literature are investigated in order to gain a clear understanding of the problem and existing solutions. The feasibility of natural ventilation and climate suitability, thermal comfort and ventilation strategies are investigated. The climate suitability study focused on the wind and solar resource of South Africa.

2.1 Feasibility of Natural Ventilation and Climate Suitability

The driving forces in natural ventilation are temperature differences and wind. Temperature induced density gradients results in unbalanced pressures. This unbalance corrects itself resulting in so-called buoyancy forces, which is a driving force for natural ventilation. Wind can further be harnessed to induce airflow in a natural ventilation system. Outdoor conditions are therefore an important factor whenever natural ventilation is investigated. This section investigates the wind and solar resource, building shape and surrounding environment of a building in South Africa. Appendix A shows an environmental impact/ amelioration implications study.

2.1.1 Wind Resource

Wind arises from pressure differences between two adjacent parcels of air. The air moves from the high pressure to the low pressure parcel so as to decrease the pressure gradient, causing wind. The Coriolis force caused by rotation of the Earth causes this wind to flow to the left in the Southern and right in the Northern Hemisphere. According to Hagemann (2008) geostrophic wind then occurs when a balance between the two forces is reached once the flow follows the isobars, which are lines of constant pressure. Due to the nature of evolution of such large scale occurrences, geostrophic wind varies with low frequency (order of days).

Hagemann (2008) states that there are dynamic mesoscale characteristics of wind with medium frequency (order of hours) which are of major importance when wind energy is extracted. The most important phenomenon is therefore

the 24 hour cycle of wind which are land/sea breezes and topographical induced (slope) winds.

Land and sea breezes are caused when a large water body is adjacent to a large land mass. The ocean's surface temperature stays relatively constant and cool due to its large specific heat. The surface temperature of the land varies during the day and night and causes positive or negative pressure gradients, and therefore wind, between the land and the sea. The pressure gradients are caused because air temperature is inversely proportional to air density and the denser air is heavier and therefore sinks to a lower domain. Topographical induced winds occur when air at high altitudes is heated while air at lower altitudes are not. Table 2.1 shows the 17 SAWS (South African Weather Service) stations with all-time mean wind speed and standard deviation.

Table 2.1: All-time mean of wind speeds, $\bar{v}$, with standard deviation, σ, as recorded by the 17 10 m South African Weather Service (SAWS) weather stations. Height is given in metres above mean sea level (amsl)

City or Town	Latitude	Longitude	Height (m)	$\bar{v}$, m/s	σ
Alexander Bay	28.57° S	16.53° E	29	4.45	3.36
Beaufort West	32.35° S	22.55° E	902	4.16	2.58
Bloemfontein	29.10° S	26.30° E	1359	2.64	2.11
Cape Town	33.97° S	18.60° E	42	5.24	3.21
Durban	29.97° S	30.95° E	8	4.22	2.56
East London	33.03° S	27.83° E	124	4.57	2.45
George	34.02° S	22.38° E	191	3.25	2.18
Irene	25.92° S	28.22° E	1524	3.20	1.74
Kimberley	28.80° S	24.77° E	1197	3.78	2.28
Lamberts Bay	32.03° S	18.33° E	93	3.72	1.93
Langebaanweg	32.97° S	18.17° E	31	3.83	2.31
Nelspruit	25.50° S	30.92° E	883	1.94	1.11
Pietersburg	23.87° S	29.45° E	1237	3.37	2.01
Port Alfred	33.60° S	26.88° E	36	3.80	2.23
Port Elizabeth	33.98° S	25.62° E	59	5.34	3.36
Thabazimbi	24.58° S	27.42° E	977	1.69	1.19
Vryheid	27.78° S	30.80° E	1163	2.25	1.52

The table indicates that the station with the highest mean wind speed is at Port Elizabeth. High standard deviations are noted in the table. Herbst and Lalk (2014) states that a number of studies based on circulation models have found changes in wind speeds over an extended period. These changes might be due to climate change. It is necessary to consult an accurate wind atlas before building a system that requires, at least in part, a sufficient wind resource to operate effectively. Hagemann (2008) constructed a wind atlas

for South Africa, shown in Figure 2.1, that is free of data voids and provides detailed, seamless and continuous coverage of the entire country. The wind atlas was contructed at a resolution of 18 km. The atlas shows that average wind speeds, measured at 10 m above ground level, are between 4 m/s and 5 m/s for South Africa.

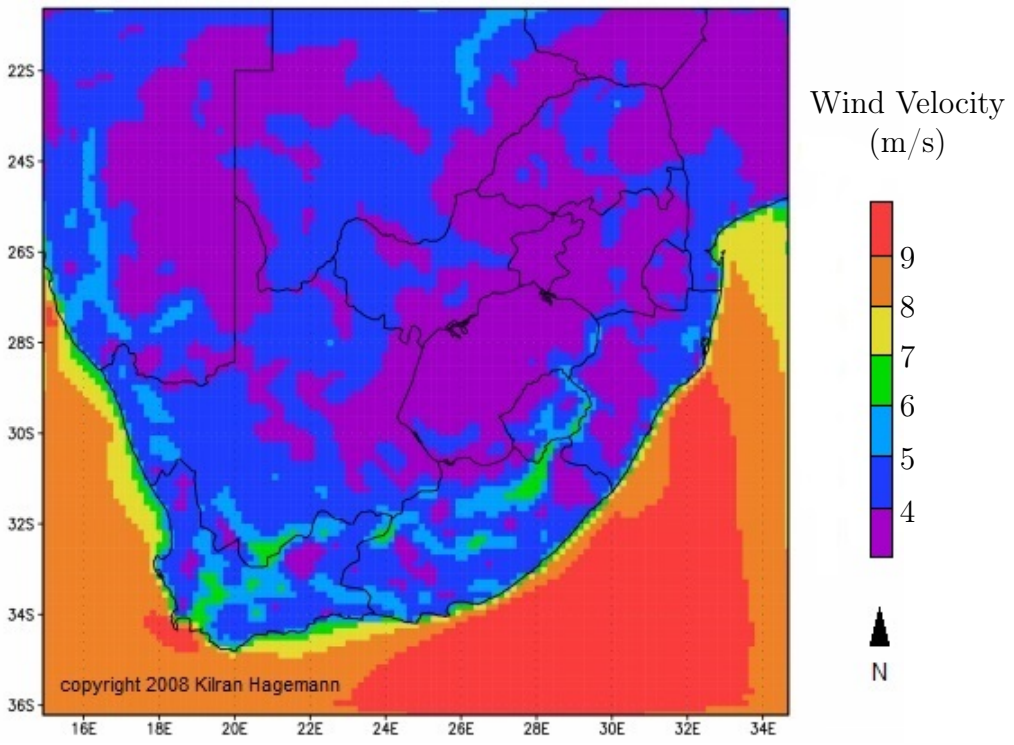

Figure 2.1: Average annual wind speeds at 10 m above ground in m/s (modified from Hagemann (2008))

2.1.2 Solar Resource

Larson (2006) states that natural ventilation is driven by pressure differences, created by either temperature differences, wind over a building, or a combination of the two. Pressure differences is induced by density differences in warm and cold air. This is often the case between the inside and the outside of a building.

Iqbal (1983) states that radiation from the sun causes thermal motion of particles in the Earth's atmosphere which causes thermal radiation. Temperature is the measurement of degree or intensity of heat present in a substance, such as the Earth's atmosphere. Low and high pressure systems in the Earth's atmosphere is caused by varying temperature gradients between two points,

generally between the equator and the poles, and the rotation of the planet. Air moving from a high to a low pressure system is what constitutes wind. Understanding the solar resource, on a local and global scale, of a site when installing a natural ventilation system is important.

To access the solar resource it is important to know what the intended application is. For the purpose of this study it is of interest to access all the available solar energy in South Africa. One such a solar resource measurement is Global Horizontal Irradiance (GHI), which is the total amount of radiation received from above by a surface horizontal to the ground (Gauché (2010)).

$$GHI = DHI + DNI \cos\theta \tag{2.1}$$

where θ is the solar zenith angle. Diffuse Horizontal Irradiance (DHI) is radiation per unit area on a surface that has been scattered by molecules in the atmosphere and that has not arrived in a direct path from the sun. Direct Normal Irradiance (DNI) is the radiation per unit area of a surface perpendicular to the incoming rays from the sun. Figure 2.2 shows a GHI map of South Africa.

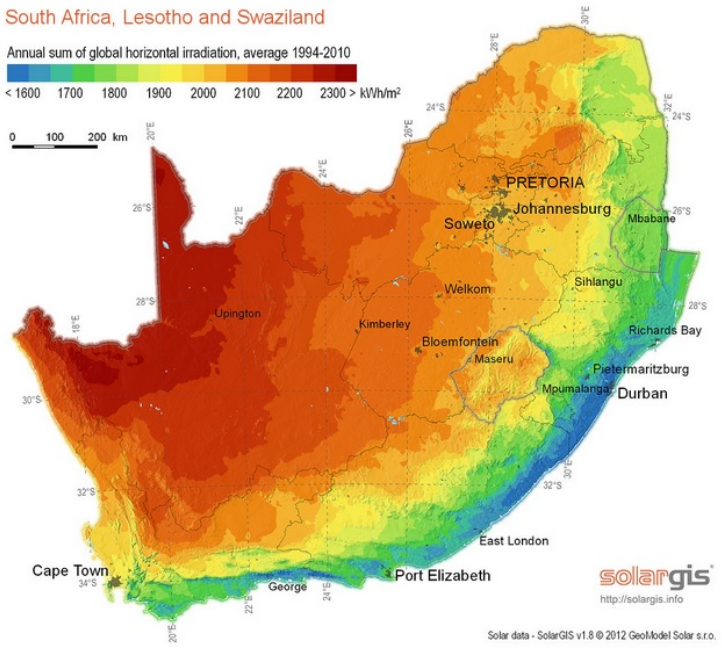

Figure 2.2: Map showing the Global Horizontal Irradiation (GHI) resource of South Africa (kWh/m^2)[Geosun, 02-11-2013, geosun.co.za/solar-maps]

From the figure it is clear that South Arica has a significant solar resource, with north-easterly parts reaching over 2300 kWh/m^2. A solar resource map showing GHI should be consulted before building a stationary structure that

requires solar energy to function, as it takes both DNI and DHI into account. DNI resource maps should be consulted when building a structure (for example a Concentrated Solar Power (CSP) plant that operates with solar radiation in a direct path from the sun).

2.1.3 Building Shape and Surrounding Environment

The building shape and the surrounding environment determines the airflow around the building and therefore the pressure generated on its surface by wind. The surface pressure distribution and the velocity field is important when choosing a location for an inlet and an outlet for a natural ventilation system. Figure 2.3 shows two cases of flow over an (i) isolated building and a (ii) densely packed array of buildings (Etheridge (2011)).

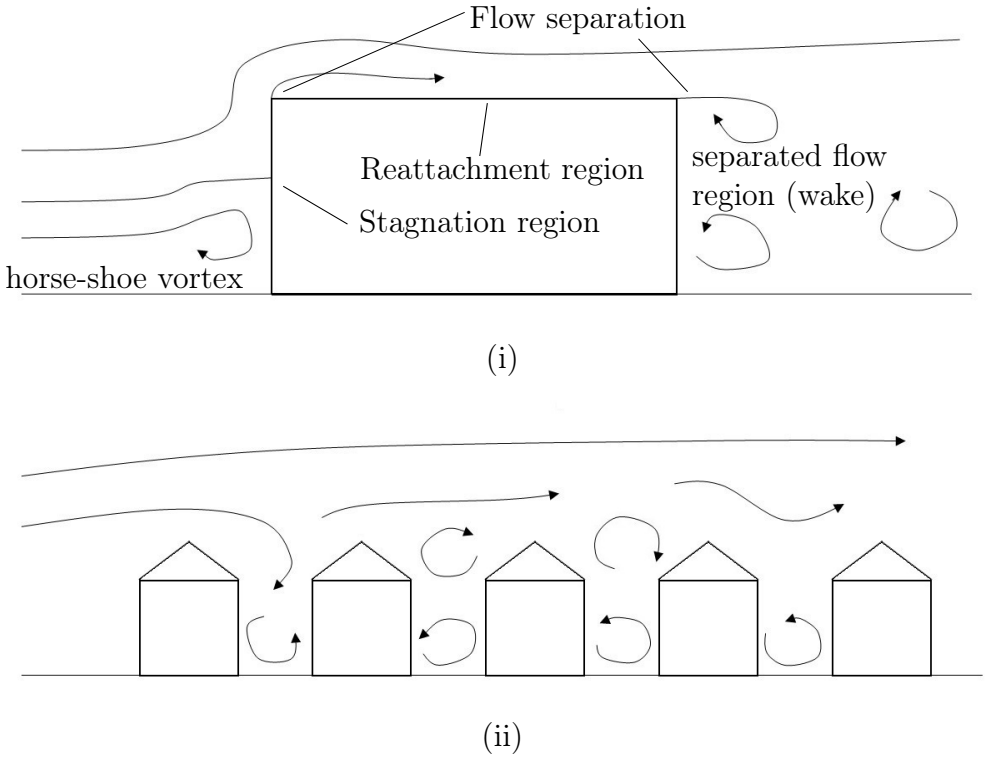

Figure 2.3: Flow patterns of two extreme cases, modified from Etheridge (2011), with (i) Isolated building showing edges and (ii) Skimming flow over densely packed buildings.

The figures show separation regions at sharp edges. Dynamic pressure from the flow of wind around a building causes positive pressures on the windward surfaces and negative pressures on the leeward side and in regions of flow separation. Building orientation, shape and environment therefore influence

optimum location for building inlets or outlets if maximum flow of fresh air at this location is required. Location of inlets and outlets in areas of positive and negative pressures can be used to harness wind to drive flow in the interior. The inherent variability of the magnitude and direction of the wind are factors to be considered when choosing an inlet and outlet location.

2.2 Thermal Comfort

Larson (2006) states that people experience more comfort in a naturally ventilated than in a mechanically ventilated room. It is however questionable whether this is psychological, where the natural air seems more clean and healthy than the air coming from a mechanically ventilated room. Larson (2006) also states that naturally moving air is often more fluctuant in its behaviour with different velocities and frequencies. This raises a futher question, namely whether the feeling of comfort is due to a physical difference in the air striking occupants.

Holm and Engelbrecht (2005) conducted a study to establish a thermal comfort range for naturally ventilated buildings in South Africa. It was found that thermal comfort is dependent on dry bulb temperature, relative air humidity, air movement, radiation, the body's metabolic rate, clothing, acclimatisation, age, body type/condition, health condition and air ions. There is therefore no single instrument that is capable of measuring all of the variables.

Holm and Engelbrecht (2005) states that there is an element of adaptation to indoor climate. The adaptation includes adjustment (behavioural/technological changes to heat balance), habitation (psychological adaptation, changing expectations) and acclimatisation (long-term physosiological adaptation to climate). The study found that a model that allows temperature adaptation to outdoor climate was the most accurate in establising occupant thermal comfort. Gauché (2010) states that this can be determined as follows,

$$Tn = 17.6 + 0.31(To_{ave}) \quad for \quad 17.8°C < Tn < 29.5°C \tag{2.1}$$

where Tn is the neutrality temperature (where occupants do not feel too hot or too cold) and To_{ave} is the average outdoor dry bulb temperature of the day, month or year. The study found that for a 90 % acceptable level for occupants cooling is required at outdoor temperatures exceeding 29.1 °C and heating is required at temperatures below 21.9 °C. Relative humidity can be ignored in Equation (2.1) between the upper and lower temperature limits. Hanley *et al.* (1995) provide a standard for relative humidity which is dependent on seasonal change and is further investigated in Section 5.1.

2.3 Ventilation Strategies

Natural ventilation can be classified as being either controlled or infiltration based. It is therefore either a controlled process using natural driving forces to intentionally displace air through an enclosed space or uncontrolled flow through openings such as windows or doors.

Elzaidabi (2008) categorises natural ventilation into four groups, namely single sided ventilation, single sided double opening, wind-driven cross ventilation and buoyancy-driven stack ventilation. Single-sided ventilation typically serves single rooms and thus provides a local ventilation solution. Inflow and outflow of air occurs through the same opening and is driven by room-scale buoyancy effects and pressure differences. Single sided double opening operates with the same principles as single sided ventilation, but with two openings that separates the inflow and outflow location. Wind-driven cross ventilation occurs if the inflow and outflow locations are on opposite sides of the enclosed space. This ventilation strategy works best if minimal internal resistance to flow is present. Buoyancy-driven stack ventilation relies on density differences to draw cool, outdoor air into an enclosed space and to exhaust the warm, indoor air out through separate openings.

Buoyancy-driven stack ventilation often utilises PDEC and solar chimneys to increase volume flow rate through the ventilation system and to assist in thermal tempering of the enclosed space. A combination of buoyancy-driven stack ventilation and wind-driven cross ventilation is often used depending on the building envelope and available wind resource.

2.3.1 Evaporative Cooling

Ibrahim *et al.* (2003) investigates two forms of evaporative cooling namely direct and indirect, illustrated in Figure 2.4. Direct evaporative cooling refers to lowering the temperature of air through the latent heat of evaporation by changing liquid water to water vapour. The air is in direct contact with the free water surface and heat from the air is used to evaporate water. The total energy in the air does not change. Indirect evaporative cooling uses a heat exchanger to cool air. Nearly no moisture is added to the incoming air, although the relative humidity does rise a little.

According to Li (2005) the heat and mass transfer processes by evaporation from a free water surface take place because of diffusion and advection. Diffusion is the heat and mass transfer by the molecular motion and advection is the heat and mass transfer by the gross motion of the fluid over the water surface. At the fluid-surface interface diffusion is predominant. Molecular diffusion causes a thin layer of vapour directly above the surface. This air-vapour mixture undergoes an increase in density and therefore the buoyant forces increase. Buoyancy is the sum of the pressure that a particle exerts on

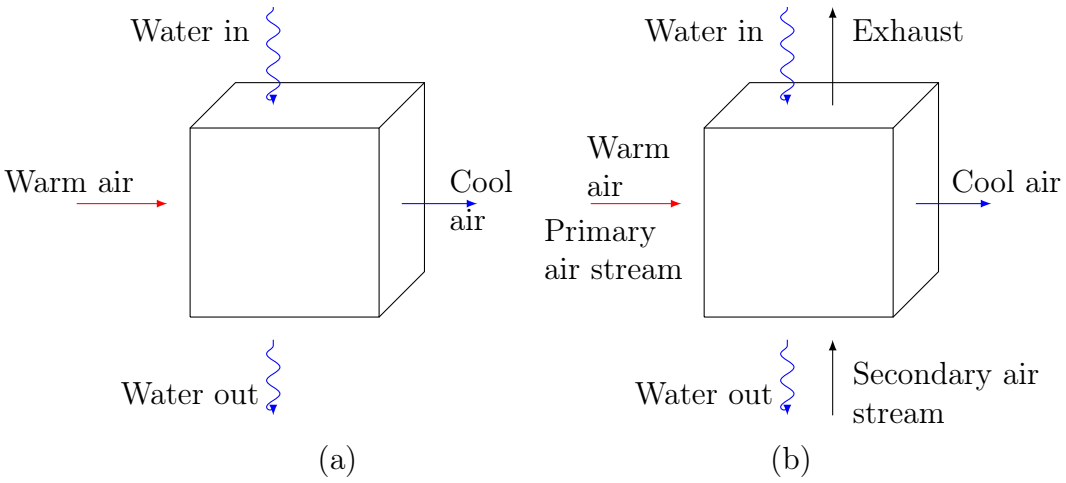

Figure 2.4: Direct (a) and indirect (b) evaporative cooling

its surroundings and the gravitational forces acting on it (Bahrami (2009)). The cooled mixture then travels downwards, creating a downdraught.

Elzaidabi (2008) states that when dry air passes over a free water surface some of the water will be absorbed by the air. Evaporative cooling therefore occurs naturally near waterfalls, rivers, lakes and oceans. Evaporation occurs because the temperature and the vapour pressure of the water and the air attempt to equalise. The wet-bulb temperature compared to the air's dry-bulb temperature is a measure of the potential for evaporative cooling.

Elzaidabi (2008) further states that evaporative cooling is a common form of cooling for thermal comfort since it is relatively cheap and requires less energy than many other forms of cooling. The drawback is that evaporative cooling requires a significant supply of water as an evaporate source and is only efficient when relative humidity is low. It is therefore restricted to dry climates, where water is often not abundant.

Cunningham *et al.* (1987) developed a theoretical model to calculate volumetric flow rate through a SCAPDEC system. The buoyancy driven flow rate was calculated as a function of ambient temperature and the average temperatures in the PDEC and solar chimneys. The influence of wind on the system was incorporated through dimensionless wind pressure coefficients, depending on the geometry of the inlet or outlet. The results were not compared with theoretical results.

Chalfoun (1997) developed a computer program called "Cool T". The program simulated conditions in a PDEC shaft with evaporative pads. Chalfoun (1997) determines the volumetric flow rate in the PDEC, by the sum of the density of air and wind forces with wind (Equation (2.1)) and with no wind (Equation (2.2)),

$$\left(\frac{\rho_t {V_t}^2}{2g_c}\right)\Sigma K = \left(\frac{g}{g_c}\right) Z \triangle\rho + \triangle C_{wp}\left(\frac{\rho_a {V_w}^2}{2g_c}\right) \tag{2.1}$$

$$V_t = \sqrt{\left(\frac{2gZ}{\Sigma K}\right)\left(1 - \frac{\rho_a}{\rho_t}\right)} \tag{2.2}$$

where ρ is air density, ρ_t is the average density in the tower, ρ_a is the average outdoor density and $\triangle\rho$ is the difference between the tower and ambient air densities. V_t is the tower velocity, V_w is the wind velocity, ΣK is the sum of the pressure loss coefficients in the tower, g_c is Newton's law conversion factor, g is gravitational acceleration, and Z is the distance from the bottom of the evaporative pads to the top of the outlet at the bottom of the tower. Chalfoun (1997) calculates the efficiency of the evaporative pads as shown in Equation(2.3).

$$\eta = \frac{t_a - t_t}{t_a - t_{wb}} \tag{2.3}$$

where $t_a - t_t$ is drop in dry bulb temperature of the air passing through the pads and $t_a - t_{wb}$ is the difference between the dry and wet-bulb air temperatures.

2.3.2 Solar Updraught Tower

A solar updraught tower or solar chimney is a passive element that makes use of solar energy to induce buoyancy-driven airflow that naturally ventilates a building (Gontikaki *et al.* (2010)). Solar radiation enters into the chimney through one or more transparent wall. The radiation travels through the glazed part, heating up the chimney walls, which in turn heat up the air inside the chimney through heat transfer. The resulting buoyancy drives the airflow through the channel. The solar chimney pulls air from the interior of the building, which is replaced by fresh air through other openings. Performance of a solar chimney is prescribed by volumetric flow rates, which are induced by a solar resource.

2.3.3 Wind Induced Natural Ventilation

Natural ventilation systems generally have slower moving air when compared with conventional heating, ventilation and air-conditioning (HVAC) systems. This is because it uses, at least to some extent, buoyancy effects to move air through an enclosed space. In natural ventilation systems the volumetric flow rate of air is often dependent on temperature and pressure differences and, in the case of a PDEC system, it is dependent on the availability of water for evaporation to occur.

In wind induced natural ventilation systems wind energy, or the kinetic energy of air in motion, is used to create a flow of air through the ventilation system, often instead of or in addition to buoyancy induced flow. These systems utilise wind catchers and/or wind extractors.

A wind cowl is an example of a wind extractor that uses wind energy, as shown in Figure 2.5. The wind cowl uses wind energy and air flowing around a guide blade turns the air outlet away from incoming wind. Wind flowing around the cowl will create a low pressure point on the outlet side, according to Bernoulli's principle. This low pressure helps to suck stale air out of the enclosed space on which the wind cowl is installed. Some wind cowls have an inlet that faces into incoming wind to force fresh outside air into the enclosed space, therefore further acting as a wind catcher.

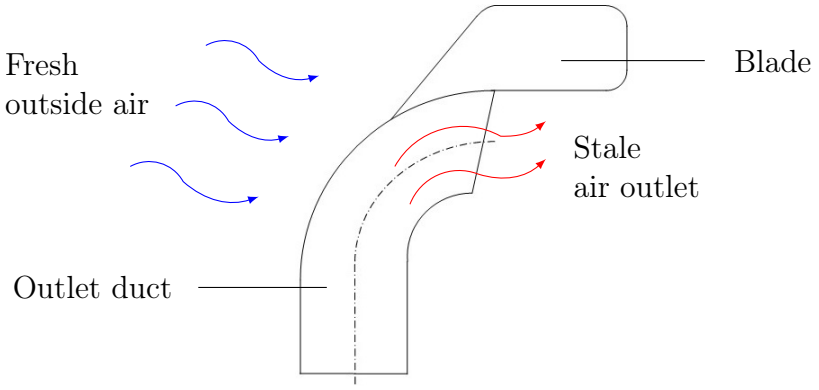

Figure 2.5: Schematic of wind cowl

Figure 2.6 shows a wind catcher in a tower that has both an inlet and an outlet. This low energy wind catcher was studied by Elzaidabi (2008). The system draws in fresh outside air through a wind catcher. The air then flows through an indirect evaporative cooler and into the enclosed space. Stale air is exhausted out on the opposite side of the tower. This system is designed to operate with extraction fans if wind energy cannot create a sufficient flow rate.

Modern wind catchers often make use of stacked inlets and outlets, as shown with stacks of louvers in Figure 2.6. Air flow in these systems is often induced by a fan with electrical energy from coal or gas fired boilers. A fan is used when wind energy is not sufficient to create the desired flow rate. It is therefore a hybrid system, as it uses both natural ventilation and energy derived from fossil fuels or another source that leaves a significant carbon footprint. If the system uses energy from a photovoltaic solar panel it may be deemed a natural ventilation system, but this may result in a more expensive solution.

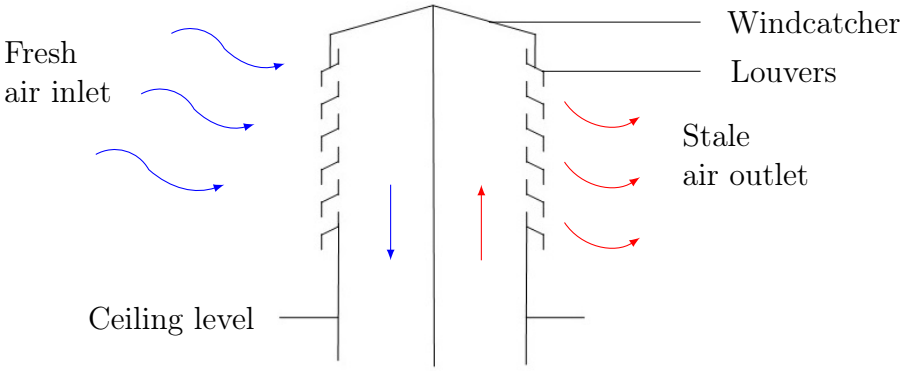

Figure 2.6: Schematic of wind-catcher tower

Pearlmutter *et al.* (1996) built a cooling tower with a water spray system in the courtyard of a building in the south of Israel. Before construction a one-third scale model was first built to predict the ability of the system to provide sufficient cooling power. Air speed, temperature and humidity measurements were taken and the cooling power of the tower was calculated as follows,

$$P = \rho A v c_p \triangle T \tag{2.4}$$

where ρ is the density of air, A is the cross-sectional area of the tower, v is air velocity, c_p is the specific heat of air and $\triangle T$ is the temperature drop between the inlet and the outlet. It was found that the air flow rate through the tower provided insufficient cooling power. A full-scale model was then built which incorporated the ability to mechanically force air through the system. Bi-directional wind capturing devices, shown in Figure 2.7, were tested on the full-scale model to try and decrease the need for a forced draught. The configurations were tested at wind speeds of up to 5 m/s.

Configuration (a) to (c) in Figure 2.7 uses inwards facing swinging louvers of varying size. Pearlmutter *et al.* (1996) defined the wind capture efficiency as the ratio between the velocity in the cooling tower and the wind speed normal to the opening of the wind catcher. It was found that these devices were not capable of capturing enough wind to increase flow rate through the system. Configurations (d) and (e) employed fixed deflectors which increased the capture efficiency. Configurations (f) and (g) had swinging panels at the centre of the configuration. The measured flow rates increased from the tests conducted on configurations (a) to (c), but did not improve on configurations (d) and (e).

Elzaidabi (2008) conducted a study where a Computational Fluid Dynamics (CFD) analysis was conducted to investigate the airflow in a low energy, wind catcher assisted, indirect evaporative cooling system. Varying wind speeds and different channels widths of the wind catcher were simulated to

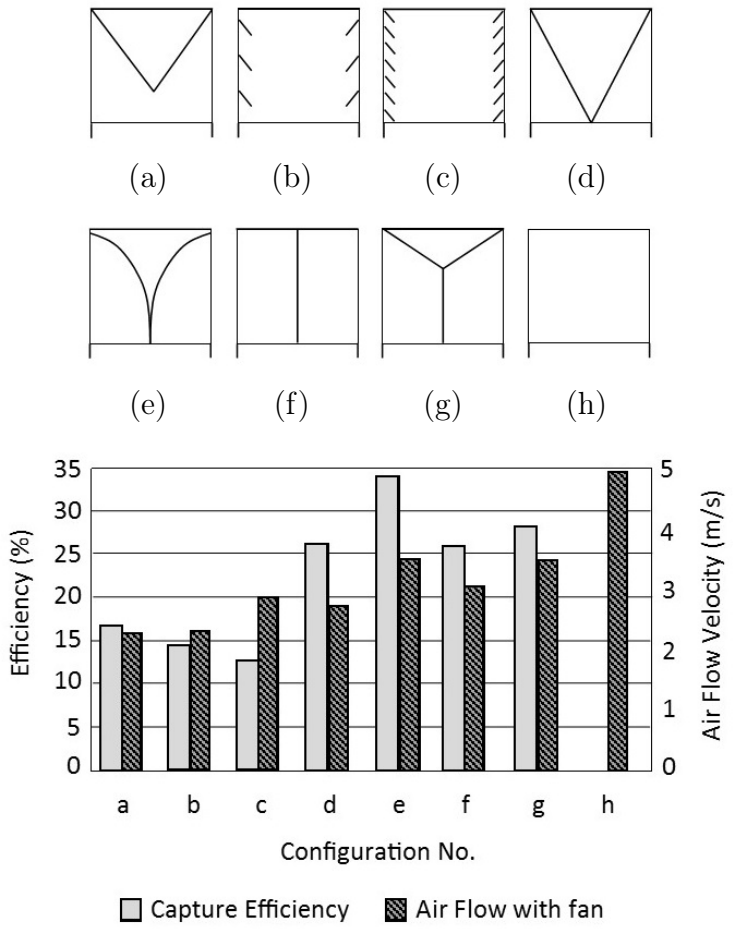

Figure 2.7: Bi-directional wind catchers (Pearlmutter *et al.* (1996))

determine how the configuration responded to changes in design. The results were further used to investigate where possible design improvements could be made to the wind catcher.

The literature survey conducted for the current study suggests that both empirical methods and CFD packages have been used to design passive cooling systems. It is therefore proposed that an empirical model of a natural ventilation system be developed, to gain an understanding of the airflow in such a system. It is further proposed that a CFD analysis be done on the same system and compared to the empirical model. CFD can additionally be used to simulate airflow around an inlet or outlet configuration installed on the ventilation system. The CFD and empirical models can assist in determining the best inlet and outlet configuration for a natural ventilation system.

3 Theory

In this section the theory used for this study is discussed. Theory regarding PDEC and solar chimney operation are investigated. Influence of evaporative cartridge dimensions are investigated and design parameters are chosen. The procedure followed and theory involved in the developement of a one-dimensional theoretical model as well as a three-dimensional CFD model is discussed. The procedure focusses on investigating the transfer of mass, energy and momentum in the PDEC and solar chimney.

3.1 Evaporative Cartridge

Evaporation occurs when the water vaporises into a surrounding gaseous phase that is not saturated. Water molecules near the surface will evaporate if they have sufficient kinetic energy to overcome intermolecular forces of liquid-phase. The molecules left behind have lower kinetic energy, which causes the temperature of the water to drop. The enthalpy change required to change water from a liquid to a gaseous phase, at a constant pressure, is known as the latent heat of vaporisation. The enthalpy is taken from the air by converting sensible into latent heat in an adiabatic process. The reduction in sensible heat of the mixture causes the temperature to decrease while the latent heat increases due to the phase change of the water from a liquid to a gaseous phase.

The water vapour mass of the air-vapour mixture increases as evaporation occurs. The relative humidity and density of the air-vapour mixture increases and molecules will start returning to the liquid phase. When the molecules escape and return to the liquid phase at the same rate the air-vapour mixture is said to be saturated. The buoyant forces of the particles, which is the sum of the pressure it exerts on its surroundings and the gravitational forces acting on it, increases. This results in buoyancy driven flow and the colder and more dense air flows in the direction of gravity. Evaporation theory suggests that evaporation occurs at the surface between the liquid and the gaseous phase. Maximising surface area in an evaporator is therefore important in air humidification.

The evaporator cartridge section is shown in Figure 3.1 and the porous material is wetted with water. Concentric pads are used in a cartridge design.

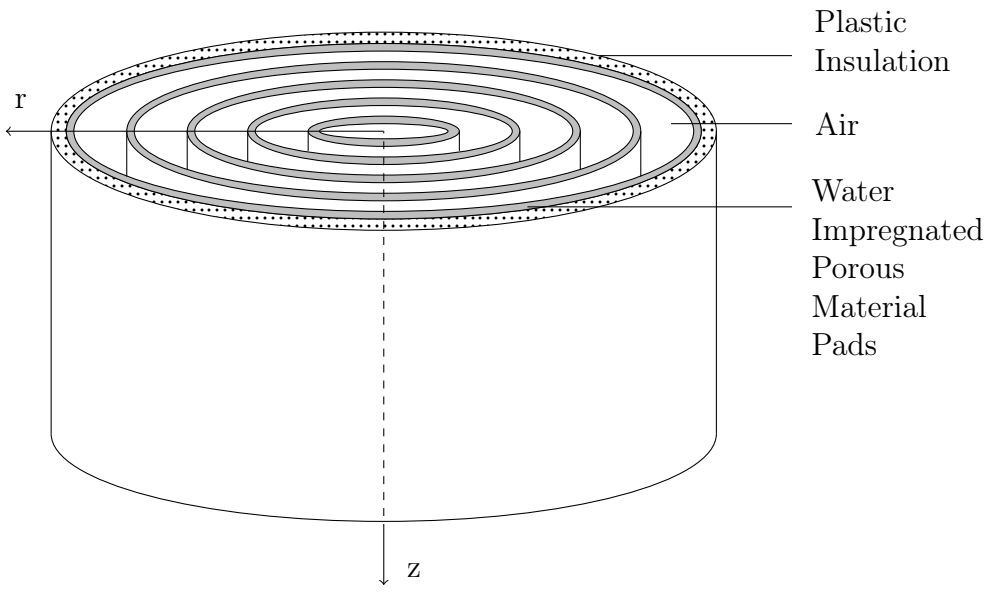

Figure 3.1: Evaporative cartridge

The cartridge forms part of the PDEC and is situated near the shaft inlet.

A discretisation scheme is used to divide the cartridge domain into annular air-vapour control volumes. Each control volume is modelled to have two adjacent liquid control volumes representing evaporator pads. Each control volume has a specific length dz, which is the total length L divided by the specified number of control volumes in the flow direction. An explicit solution method is used to solve the finite difference equation for the conservation of mass, energy and momentum for each control volume. New conditions for each control volume is then calculated at the next time step Δt.

It is assumed that each control volume has a uniform property distribution. The discretisation scheme of the one-dimensional axi-symmetric model of evaporative cartridge is shown in Figure 3.2.

3.1.1 Heat Transfer

Sensible heat transfer will take place between the liquid surface and air if there is a temperature gradient in the distance between them. A positive or negative sensible heat transfer will occur between the surface and the air from a high to a low temperature. If the air temperature is higher than the water temperature, heat will be added to the liquid and water vapour will start diffusing into the air. This added latent heat of evaporation does not increase the temperature of the water. Energy is removed from the surrounding water molecules at the surface during evaporation, which causes the water temperature to decrease. The water vapour becomes part of the air-vapour mixture, which will have

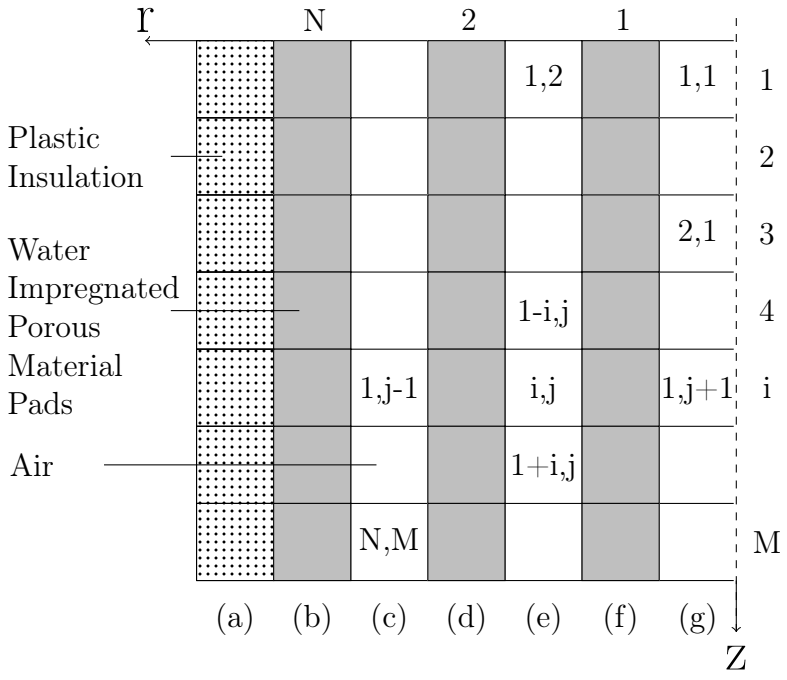

Figure 3.2: Axi-symmetric discretisation of evaporative cartridge showing air (c), (e) and (g), water impregnated porous material (b), (d) and (f) and plastic insulation control volumes (a)

a lower temperature than the initial air temperature. This colder, and more dense air will then sink downwards. In this process ambient air, entering the PDEC shaft, will be cooled due to heat transfer from the air to the liquid in the pads. Newton's law of cooling can be used to calculate the rate of heat transfer from the air to the liquid (O/Sullivan(1990)).

$$\dot{Q}_{ml(i,j)} = h_{(i,j)} A_{s(i,j)} (T_{m(i,j)} - T_{l(i,j)}) \tag{3.1}$$

where $h_{(i,j)}$ is the convection heat transfer coefficient, $A_{s(i,j)}$ is the heat transfer surface area, $T_{m(i,j)}$ is the air mixture temperature and $T_{l(i,j)}$ is the liquid temperature.

In order to calculate the convection heat transfer coefficient, the flow in the annulus has to be classified as being developing or fully developed flow. Dou *et al.* (2005) state that for annular flow with a small volume flow rate and low Reynolds number, the flow will be below the critical point of instability and can be considered as being fully developed. The ratio of the energy gradient in the transverse direction to that of the streamwise direction should be small. Assuming fully developed flow, as the channel between the pads is relatively small, the heat transfer coefficient for the inside and outside surfaces bordering the annular flow space can be calculated.

$$h_i = \frac{Nu_i k}{D_{(i,j+1)} - D_{(i,j)}} \tag{3.2}$$

$$h_o = \frac{Nu_o k}{D_{(i,j+1)} - D_{(i,j)}} \tag{3.3}$$

where Nu_i and Nu_o are the Nusselt numbers and $D_{(i,j)}$ and $D_{(i,j+1)}$ are the inner and outer diameters. The Nusselt number for fully developed flow can be calculated for laminar and turbulent flow as shown in

$$Nu = 3.66 \tag{3.4}$$

$$Nu = 0.023 Re_{eff}^{0.8} Pr^{0.3} \tag{3.5}$$

where,

$$Re_{eff} = \frac{\rho_{m(i,j)} v_{avg} D_{h(i,j)}}{\zeta \mu_m} \tag{3.6}$$

and for annular flow

$$\zeta = \frac{(a-b)^2(a^2-b^2)}{a^4 - b^2 - (a^2-b^2)^2 / ln(a/b)} \tag{3.7}$$

with $a = \frac{D_(i,j)}{2}$ and $b = \frac{D_(i,j+1)}{2}$ being the outer and inner radii of the evaporation surfaces bordering the annular control volume.

There is further heat transfer from the environment through the insulation to the evaporative pads and mixture. Figure 3.3 shows the thermal resistance network between the environment and control volumes bordering the plastic insulation. Newton's law of convective cooling is used to calculate this heat transfer, as shown in Equation (3.8).

$$\dot{Q}_{em(i,j)} = \frac{T_e - T_{m(i,N)}}{R_{em}} \tag{3.8}$$

where T_e is the environmental temperature, $T_{m(i,N)}$ is the mixture temperature and R_{em} is the total thermal resistance.

$$R_{em} = R_{ew} + R_{wl} + R_{lm} \tag{3.9.a}$$

$$= \left(\frac{1}{h_e A} + \frac{\Delta r_{wall}}{2 k_{wall} A}\right) + \left(\frac{\Delta r_{wall}}{2 k_{wall} A} + \frac{\Delta r_{liquid}}{2 k_{liquid} A}\right) + \left(\frac{\Delta r_{liquid}}{2 k_{liquid} A} + \frac{1}{h_i A}\right) \tag{3.9.b}$$

where h_e is the convection heat transfer coefficient outside the insulation, A is the constant radial area, Δr_{wall} is the thickness of the wall, k_{wall} and k_{liquid} are the wall and liquid conduction heat transfer coefficients, Δr_{liquid} is the thickness of the liquid control volume and h_i is the mixture convection heat transfer coefficient.

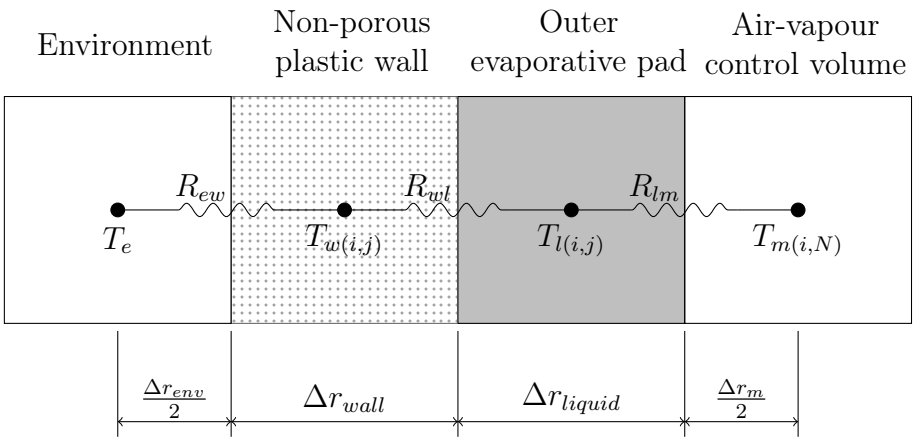

Figure 3.3: Thermal resistance diagram of control volumes bordering plastic insulation

3.1.2 Mass Transfer

During evaporation liquid molecules diffuse from the evaporative cartridge into the surrounding mixture. This diffusion of water vapour results in a transfer of mass from the liquid to the mixture. From the discretisation scheme, shown in Figure 3.2, it can be seen that each air-vapour mixture control volume is surrounded by two liquid control volumes so that mass diffusion occurs from both sides.

$$\dot{m}_{lm} = h_{lm} A_{lm} (\rho_{vsat@Tl} - \rho_{v@Tm}) \tag{3.10}$$

where

$$h_{lm} = \frac{Sh D_{va}}{D} \tag{3.11}$$

$$A_{lm} = \pi D dz \tag{3.12}$$

$$\rho_{vsat@Tl} = \frac{P_{vsat@T_l}}{R_v T_l} \tag{3.13}$$

where D is the inner and outer diameter for each mixture control volume. To calculate the heat transfer coefficient h_{lm}, the Sherwood number and mass diffusivity of water vapour in air needs to be calculated. The Sherwood number or mass transfer Nusselt number is calculated for laminar or turbulent flow.

$$Sh = 3.66 \quad for \quad Re_{eff} < 2300 \tag{3.14}$$

$$Sh = 0.023 Re_{eff}^{0.8} Sc^{0.35} \quad for \quad Re_{eff} > 2300 \tag{3.15}$$

where

$$Sc = \frac{\mu_m}{\rho_m D_{va}} \tag{3.16}$$

and

$$D_{va} = \frac{1.87 \times 10^{-10} T^{2.072} P}{P_v + P_a} \tag{3.17}$$

White (2005) specifies the effective Reynolds number to be,

$$R_{eff} = \frac{\rho_{m(i,j)} v_{avg(i,j)} D_{h(i,j)}}{\zeta \mu_m} \tag{3.18}$$

where

$$\zeta = \frac{(a-b)^2(a^2-b^2)}{a^4 - b^4 - (a^2-b^2)^2 / ln(a/b)} \tag{3.19}$$

where a and b is the inner and outer radii of the annular air-vapour control volume.

3.1.3 Conservation of Mass

The one-dimensional flow field only allows for one non-zero flow direction component (Lagoudas and Haisler (2002)). In the flow field mass transfer occurs from the liquid to the adjacent mixture control volume. It is not in the flow direction, but is taken into consideration. The law of conservation of mass states,

$$\frac{dm_{cv}}{dt} = \Sigma \dot{m}_{in} - \Sigma \dot{m}_{out} \tag{3.20}$$

where $\dot{m}_{in}$ and $\dot{m}_{out}$ are the mass flow rates in and out of a control volume and are calculated as follows:

$$\dot{m} = \rho A v \tag{3.21}$$

Figure 3.4 shows the mixture control volume which consists of air and water vapour. The coordinates were defined in Figure 3.2. The control volume shown is surrounded by liquid control volumes on either side and is not situated next to the axis.

The new mixture mass is calculated at time $t+\Delta t$ using the explicit solution method.

$$m_{m(new)} = m_{a(new)} + m_{v(new)} \tag{3.22}$$

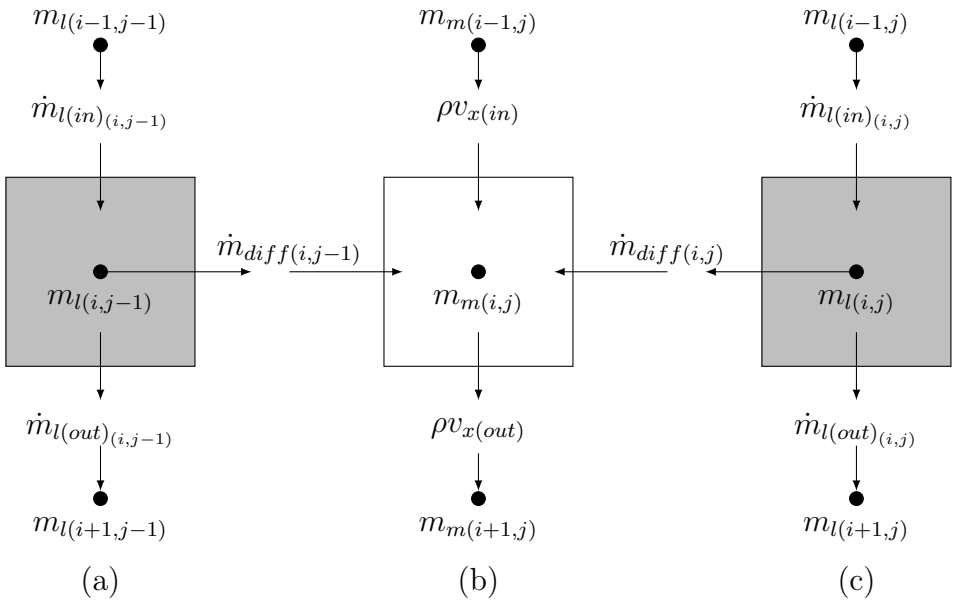

Figure 3.4: Conservation of mass control volumes for liquid (a) and (c), and air-water vapour mixture (b)

where

$$m_{a(new)} = m_{a(old)} + \Delta t(\dot{m}_{ain(i-1,j)} - \dot{m}_{aout(i,j)}) \tag{3.23}$$

$$m_{v(new)} = m_{v(old)} + \Delta t(\dot{m}_{vin(i-1,j)} - \dot{m}_{vout(i,j)}) \tag{3.24}$$

3.1.4 Conservation of Energy

The law of conservation of energy is known as the first law of thermodynamics and can be written as a rate equation:

$$\frac{dE}{dt} = \dot{Q} - \dot{W} \tag{3.25.a}$$

$$= \lim_{dt\to 0}\left(\frac{\delta Q}{dt}\right) + \lim_{dt\to 0}\left(\frac{\delta W}{dt}\right) \tag{3.25.b}$$

where $\dot{Q}$ is the rate of total heat transfer to the control volume and $\dot{W}$ is the rate of total work done by the control volume. Figure 3.5 shows the law of conservation of energy applied to adjacent liquid and mixture control volumes.

If it is assumed that mass enters the liquid control volume at the same rate it exits or evaporates, then the liquid control volume has a constant mass.

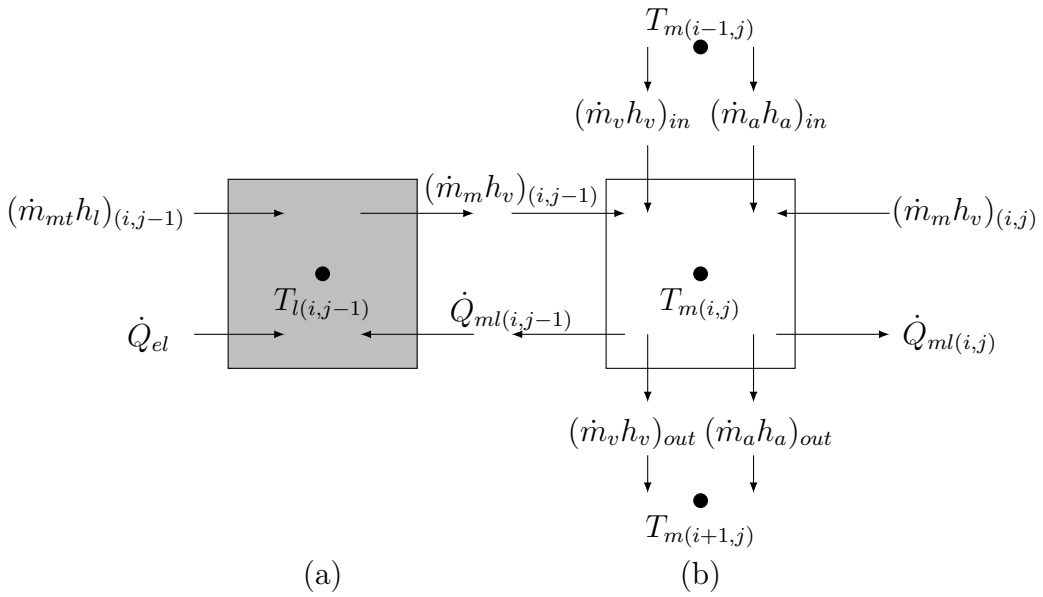

Figure 3.5: Conservation of energy control volume for liquid (a) and air-water vapour mixture (b)

Equation (3.26.a) shows the law of conservation of energy applied to a liquid control volume.

$$\frac{dE}{dt} = \frac{d}{dt}(m_l c_v T_l) \tag{3.26.a}$$

$$= \dot{Q}_{el} + \dot{Q}_{ml} + (\dot{m}_{mt} h_l)_{(i,j)} - (\dot{m}_{mt} h_v)_{(i,j)} \tag{3.26.b}$$

where $\dot{Q}_{el}$ is the rate of heat transfer from the environment to the liquid, $\dot{Q}_{ml}$ is the rate of heat transfer from the mixture to the liquid, h_l is the enthalpy of the water flowing into the volume and h_v is the enthalpy of the vapour. Applying an explicit solution scheme allows for the new liquid temperature to be calculated.

$$T_{lnew(i,j)} = T_{lold(i,j)} + \Delta t \left(\frac{\dot{Q}_{ml} + \dot{Q}_{el} + (\dot{m}_{mt} h_l)_{(i,j)} - (\dot{m}_{mt} h_v)_{(i,j)}}{m_{l(i,j)} c_v} \right) \tag{3.27}$$

The law of conservation of energy is applied to the mixture control volume with the assumption that only heat is transferred and no work is done. The mixture control volume undergoes a change in mass and temperature as shown in Equation (3.28).

$$\frac{dE}{dt} = \frac{d}{dt}(m_m c_v T_m) \tag{3.28.a}$$

$$= m_m c_v \frac{dT}{dt} + c_v T_m \frac{dm}{dt} \tag{3.28.b}$$

$$= (\dot{m}_a h_a)_{in} + (\dot{m}_v h_v)_{in} - (\dot{m}_a h_a)_{out} - (\dot{m}_v h_v)_{out} + (\dot{m}_{mt} h_v)_{i,j-1} + (\dot{m}_{mt} h_v)_{i,j} - \dot{Q}_{me} - \dot{Q}_{ml} \tag{3.28.c}$$

Heat is transferred between each mixture control volume and its surrounding mixture and liquid volumes. If it is assumed that there is a positive flow rate through the volume, as shown in Figure 3.5, everything entering and exiting the control volume can be summed.

$$(\dot{m}h)_{in} = (\dot{m}_a h_a)_{in} + (\dot{m}_v h_v)_{in} - (\dot{m}_a h_a)_{out} - (\dot{m}_v h_v)_{out} + (\dot{m}_{mt} h_v)_{i,j-1} \tag{3.29}$$

$$(\dot{m}h)_{out} = (\dot{m}_{mt} h_v)_{i,j} - \dot{Q}_{me} - \dot{Q}_{ml} \tag{3.30}$$

Equations (3.29) and (3.30) assumes an upwind differencing scheme. The explicit solution scheme can now be applied to calculate the new air-vapour mixture temperature.

$$T_{mnew(i,j)} = T_{mold(i,j)} + \Delta t \left(\frac{(\dot{m}h)_{in} - (\dot{m}h)_{out} - c_v T_{mold} \frac{dm}{dt}}{m_{m(i,j)} c_v} \right) \tag{3.31}$$

3.1.5 Conservation of Momentum

Linear momentum is a vector with both direction and magnitude. The law of conservation of momentum as applied to a one-dimensional control volume is given by Equation (3.32).

$$\frac{\Delta mv}{\Delta t} = \dot{m}v_{in} - \dot{m}v_{out} + \Sigma F \tag{3.32}$$

The momentum conservation law applied to the control volume in Figure 3.6 is given by Equation (3.33).

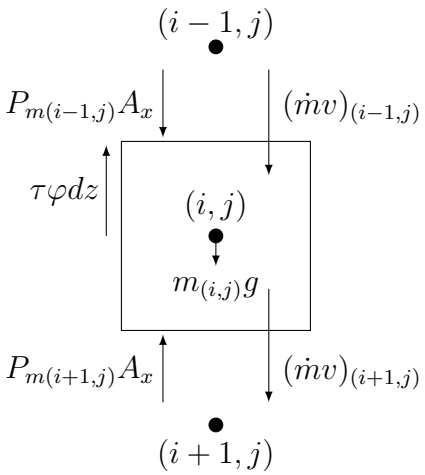

Figure 3.6: Conservation of momentum control volume

$$\frac{\Delta(mv)_{(i,j)}}{\Delta t} = (P_{m(i-1,j)} - P_{m(i+1,j)})A_x + ((\dot{m}v)_{(i,j)} - (\dot{m}v)_{m(i+1,j)}) + mgsin\theta - \tau\varphi dz \quad (3.33)$$

where A_x is the area in the radial direction, $\dot{m} = \rho A_x v$, and $\varphi = \pi D$. The shear stress is given by $\tau = \frac{\rho C_f (g/A_x)^2}{2}$, where $v = G/A_x$ and $f = 4C_f$. These values can be substituted into Equation (3.33) and divided by A_x, which results in Equation (3.34).

$$\frac{\Delta(mG/A_x{}^2)_{(i,j)}}{\Delta t} = (P_{m(i-1,j)} - P_{m(i+1,j)}) + \left(\frac{\rho_{i-1,j}G^2}{A_x A_{x(i-1,j)}} - \frac{\rho_{i+1,j}G^2}{A_x A_{x(i+1,j)}}\right) + \rho g dz sin\theta - f\frac{\rho\pi D(G/A_x)^2 dz}{8A_x} \quad (3.34)$$

The equation can be integrated for all the control volumes along the evaporative cartridge. dx is replaced with $L_{(i,j)}$ and the minor losses are acounted for by the use of equivalent lengths (Yildirim (2008)). For a sharp inlet the equivalent length was taken as $L_{eq} = 18D_h$ (Batty and Folkman (1983a)). Equation (3.34) can further be simplified by applying the Boussinesq approximation. The density is then essentially constant except in the buoyancy term. The density in each term is then calculated by means of the ideal gas approximation.

$$\sum_{i=1}^{N} \frac{\Delta(mG/{A_x}^2)_{(i,j)}}{\Delta t} = \bar{\rho}g(L_0 - L_{N+1}) + \sum_{i=1}^{N} \left(\frac{\rho_{i-1,j}G^2}{A_x A_{x(i-1,j)}} - \frac{\rho_{i+1,j}G^2}{A_x A_{x(i+1,j)}} \right) + \sum_{i=1}^{N} \rho_{(i,j)} g L_{(i,j)} sin\theta - \sum_{i=1}^{N} f \frac{\rho\pi D(G/A_x)^2 (L_{(i,j)} + L_{eq(i,j)})}{8A_x} \quad (3.35)$$

3.1.6 Solution Procedure of One−Dimensional Model for the Evaporative Cartridge

The stepwise solution procedure for the evaporative cartridge theoretical model is outlined below.

1 Define matrix sizes, fluid properties, time step, number of control volumes, cartridge length and diameter and set boundary conditions.
2 Calculate the rates of heat transfer between the liquid and mixture control volumes as well as heat transfer from environment.
3 Use Equations (3.23) and (3.24) to calculate the new air and vapour masses.
4 Use Equation (3.31) to calculate the new mixture temperature.
5 Calculate the Reynolds number for each control volume.
6 Calculate the mass transfer rates from the liquid to the mixture control volumes with Equation (3.10).
7 Use Equation (3.27) to calculate the new liquid temperature.
8 Apply the finite difference formulation of Equation (3.35) to determine the volumetric flow rate.
9 Set the old values at time t equal to the new values at time $t + \Delta t$.
10 Repeat steps 2 to 9 until the preset stoppage time is reached.

3.2 Solar Chimney

A solar chimney is used to evacuate stale air from an enclosed area. One or more of the solar chimney walls are heated with solar radiation, which then heats the air inside the chimney. The process of heating walls with solar radiation is transient and for this study a steady state solution is required. The air inside the solar chimney is therefore heated by a temperature difference existing across the wall of the chimney. Convergence testing of the finished one-dimensional model is shown in Appendix B.2.

3.2.1 Heat Transfer

The initial temperature of the air inside the chimney is expected to be lower than the environmental temperature, as the environment around the chimney is heated to ensure a temperature gradient across the chimney wall. The thermal resistance diagram is shown in Figure 3.7. The heat transfer rate from the environment to the air can be calculated with Equation (3.1).

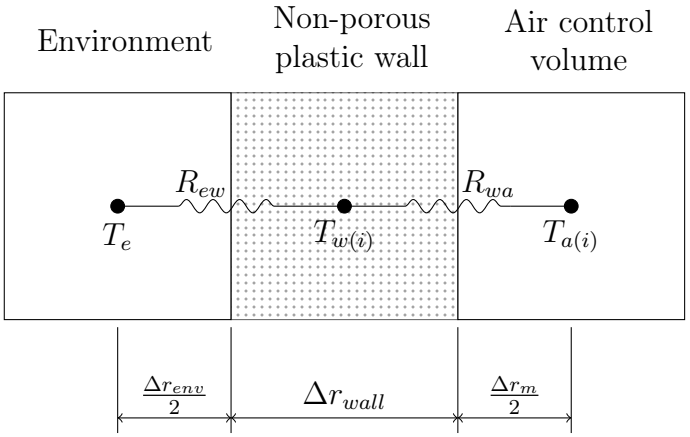

Figure 3.7: Thermal resistance network of control volume and bordering walls

$$\dot{Q}_{em(i)} = \frac{T_e - T_{a(i)}}{R_{em}} \tag{3.1}$$

where T_e is the environmental temperature, $T_{a(i)}$ is the air temperature inside the chimney and R_{em} is the total thermal resistance.

$$R_{em} = R_{ew} + R_{wa} \tag{3.2.a}$$

$$= \left(\frac{1}{h_o A_o} + \frac{ln(\frac{r_o}{(r_o+r_i)/2})}{4\pi dz k_{plas}}\right) + \left(\frac{ln(\frac{(r_o+r_i)/2}{r_i})}{4\pi dz k_{acr}} + \frac{1}{h_i A_i}\right) \tag{3.2.b}$$

where h_o and h_i are the outside and inside convection coefficients, A_o and A_i are the outside and inside areas, r_o and r_i are the outside and inside radii, dz is the length of one control volume and k_{plas} is the plastic conduction coefficient.

Cengel (2006) provides a way to calculate the inside heat transfer coefficient for laminar and turbulent flow.

$$h_{i,laminar} = 3.66 \tag{3.3}$$

$$h_{i,turbulent} = 0.023 Re^{0.8} Pr^{0.4} \tag{3.4}$$

The outside heat transfer coefficient can be calculated with Equation (3.5) (Wong (1997)).

$$h_o = \frac{Nu_z k}{L} = C{Ra_L}^n K = CGr_z Pr^n K = C\left(\frac{g\beta\rho^2(T_e - T_s)L^3 c_p}{\mu k}\right)^n K \quad (3.5)$$

where Nu_z is the Nusselt number in the z direction, L is the characteristic length, k is the thermal conductivity of the air, C is the flow constant, n is a constant taken as 0.25 for turbulent flow and 0.33 for laminar flow, Ra_L is the Rayleigh number which is a function of the Grashoff and the Prandtl number where g is gravitational acceleration, ρ is air density, β is the coefficient of thermal expansion, μ is viscosity, T_e is the environment temperature, T_s is the surface temperature and c_p is the specific heat of air. K is a dimensionless correction factor that can be calculated for laminar and turbulent flow.

$$K_{laminar} = \left[1 + \left(1 + \frac{1}{\sqrt{Pr}}\right)^2\right]^{-\frac{1}{4}} \quad (3.6)$$

$$K_{turbulent} = \left[\frac{Pr^{\frac{1}{6}}}{1 + Pr^{\frac{2}{3}}}\right]^{\frac{2}{5}} \quad (3.7)$$

3.2.2 Conservation of Mass

If it is assumed that no condensation occurs in the solar chimney the mass of the air entering a control volume will equal the mass of the air going out. The air exiting the solar chimney is lost to the environment. The volume mass of the exiting air is not a major factor in the design as it is not reused in the system.

Figure 3.8 shows a control volume with the mass of the air mixture. An explicit solution method is used to solve the new air and vapour masses.

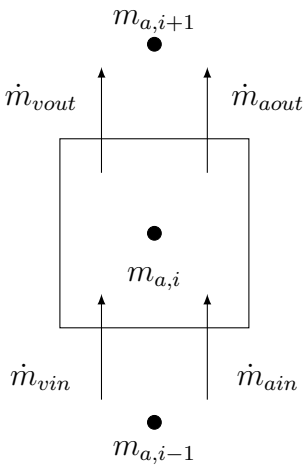

Figure 3.8: Conservation of mass control volume

$$m_{a,i}{}^{new} = m_{a,i} + \Delta t(\dot{m}_{ain} - \dot{m}_{aout})^{old} \tag{3.8}$$

$$m_{v,i}{}^{new} = m_{v,i} + \Delta t(\dot{m}_{vin} - \dot{m}_{vout})^{old} \tag{3.9}$$

3.2.3 Conservation of Energy

Energy may be transferred between a control volume and its adjacent volumes. Energy is added to a volume from the environment by conduction through the chimney walls if it is assumed that the environment is at a higher temperature. Figure 3.9 shows a control volume of the solar chimney.

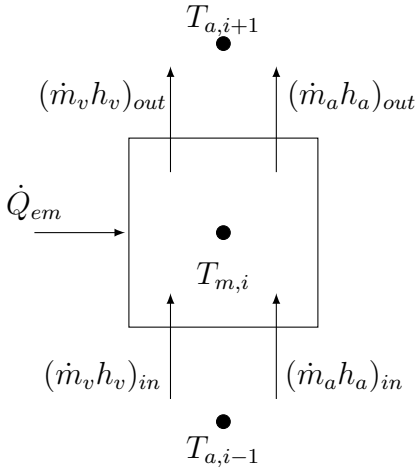

Figure 3.9: Conservation of energy control volume

The finite difference equation for a positive mass flow rate is given in Equation (3.10.a). The energy transferred from the solar chimney, $\dot{Q}_{sc}$, is the energy transferred from the heated walls and not from the environment.

$$\frac{dE}{dt} = \frac{d}{dt}(m_m c_v T_m) \tag{3.10.a}$$

$$= m_m c_v \frac{dT}{dt} + T_m c_v \frac{dm}{dt} \tag{3.10.b}$$

$$= (\dot{m}_a h_a)_{i-1} + (\dot{m}_v h_v)_{i-1} - (\dot{m}_a h_a)_i - (\dot{m}_v h_v)_i + \dot{Q}_{sc} \tag{3.10.c}$$

Equation (3.10.c) can be shortened by summing everything entering and exiting the control volume.

$$(\dot{m}h)_{in} = (\dot{m}_a h_a)_{i-1} + (\dot{m}_v h_v)_{i-1} + \dot{Q}_{sc} \tag{3.11}$$

$$(\dot{m}h)_{out} = (\dot{m}_a h_a)_i + (\dot{m}_v h_v)_i \tag{3.12}$$

The new temperature the mixture control volume can now be calculated, as shown in Equation (3.13).

$$T_m{}^{new} = T_m{}^{old} + \Delta t \left(\frac{(\dot{m}h)_{in} - (\dot{m}h)_{out} - T_m{}^{old} c_v \frac{dm}{dt}}{m_{m(i,j)} c_v} \right) \tag{3.13}$$

3.2.4 Conservation of Momentum

The law of conservation of momentum, given by Equation (3.32), is applied to the control volume shown in Figure 3.10. Th result is given by Equation (3.14).

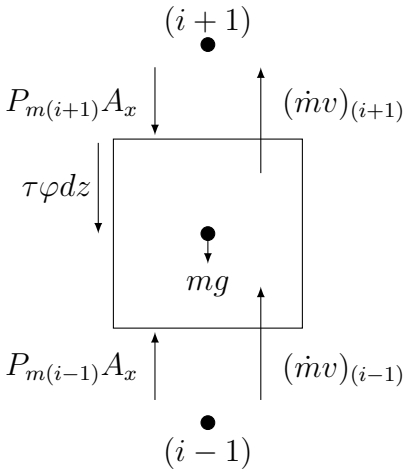

Figure 3.10: Conservation of momentum control volume

$$\frac{\Delta(mv)_i}{\Delta t} = (P_{m,i-1} - P_{m,i+1})A_x + ((\dot{m}v_{i-1} - \dot{m}v_{i+1})) + mgsin\theta - \tau\varphi dz \quad (3.14)$$

Where $\dot{m} = \rho A_x v$, $\varphi = \pi D$, $G = A_x v$ and the shear stress expressed as $\tau = f\frac{\rho v^2}{8}$. Dividing by A_x gives Equation (3.15).

$$\frac{\Delta(mG/{A_x}^2)_i}{\Delta t} = (P_{m,i-1} - P_{m,i+1}) + \left(\frac{\rho_{i-1}G^2}{A_x A_{x,i-1}} - \frac{\rho_{i+1}G^2}{A_x A_{x,i+1}}\right) + \rho g dz sin\theta - f\frac{\rho\pi D(G/A_x)^2 dz}{8A_x} \quad (3.15)$$

Equivalent lengths are used to incorporate inlet and outlet losses in the solar chimney (Batty and Folkman (1983*b*)). An equivalent length is incorporated into the theoretical model with $L_{eq} = \frac{kD}{f}$ (for a sharp inlet L_{eq}=$18D_h$), where D is the Diameter, f is the friction factor and k is the loss coefficient that is determined experimentally, as explained in Sections 3.4 and 3.5. Equation (3.15) can be integrated through the length of the chimney in the same procedure as outlined for Equation (3.35).

$$\sum_{i=1}^{N}\frac{\Delta(mG/{A_x}^2)_i}{\Delta t} = \sum_{i=1}^{N}\left(\frac{\rho_{i-1}G^2}{A_x A_{x,i-1}} - \frac{\rho_{i+1}G^2}{A_x A_{x,i+1}}\right) + \bar{\rho}g(L_0 - L_{N+1}) + \sum_{i=1}^{N}\rho_i g L_i sin\theta - \sum_{i=1}^{N} f\frac{\rho\pi D(G/A_x)^2(L_i + L_{eq,i})}{8A_x} \quad (3.16)$$

3.2.5 Solution Procedure of One−Dimensional Model for the Solar Chimney

The stepwise solution procedure for the solar chimney theoretical model is outlined below.

1 Define matrix sizes, fluid properties, time step, stoppage time, number of control volumes, inlet and outlet loss factors, chimney length and diameter, and set boundary conditions.
2 Specify chimney wall outer temperature gradient and determine heat transfer to control volume with Equation (3.1).
3 Use Equations (3.8) and (3.9) do calculate the new air and vapour masses.
4 Use Equation (3.13) to calculate the new mixture temperature.
5 Calculate the Reynolds number for each control volume.

6 Apply the finite difference formulation of Equation (3.16) to determine the new volumetric flow rate.
7 Set the old values at time t equal to the new values at time $t + \Delta t$.
8 Repeat steps 2 to 7 until the preset stoppage time is reached.

3.3 CFD Theory

In order to obtain theoretical results to validate experimental results a CFD package was used. FLUENT® was chosen, as it is capable of compiling fine three-dimensional meshes using user-defined inputs, boundary conditions and solution setups. The CFD theory is largely based on the modelling used in (Fluent (2010)).

3.3.1 Conservation of Mass

The mass conservation equation is also called the continuity equation. It is shown in Equation (3.1) and is solved by FLUENT® for phase q.

$$\frac{\partial}{\partial t}(\alpha_q \rho_q) + \nabla \cdot (\alpha_q \rho_q \vec{v}_q) = \sum_{p=1}^{n} (\dot{m}_{pq} - \dot{m}_{qp}) + S_q \tag{3.1}$$

where α_q is the volume fraction of phase q, ρ_q is the density of phase q, $\vec{v}_q$ is the velocity of phase q, $\dot{m}_{pq}$ characterises the mass transfer from the p^{th} to q^{th} phase and $\dot{m}_{qp}$ the other way around. S_q is the source term. The source term is zero by default and the mass transfer rates are affected when evaporation and condensation is specified, as discussed later, in Section 3.3.4.

3.3.2 Conservation of Energy

FLUENT® solves the energy equation in the following form:

$$\frac{\partial}{\partial t}(\rho E) + \nabla \cdot (\vec{v}(\rho E + p)) = \nabla \cdot \left(k_{eff} \nabla T - \sum_j h_j \vec{J}_j + (\bar{\bar{\tau}}_{eff} \cdot \vec{v}) \right) + S_h \tag{3.2}$$

where k_{eff} is the effective conductivity, $\vec{J}_j$ is the diffusion flux of species j and S_h includes the heat of chemical reaction and any other defined heat sources. The first three terms on the right-hand side of Equation (3.2) represent energy transfer due to conduction, species diffusion, and viscous dissipation, respectively. In Equation (3.2):

$$E = h - \frac{p}{\rho} + \frac{v^2}{2} \tag{3.3}$$

where the sensible enthalpy h, for ideal gases, is defined as

$$h = \sum_j Y_j h_j \tag{3.4}$$

where

$$h_j = \int_T^{T_{ref}} c_{p,j} dT \tag{3.5}$$

In Equation (3.4), Y_j is the mass fraction of species j and T_{ref} is a reference temperature of 298.15 K. Equation (3.2) includes pressure work, kinetic energy terms and enthalpy transport due to species diffusion.

3.3.3 Conservation of Momentum

The conservation of momentum for fluid phase q, as solved by FLUENT®, is

$$\frac{\partial}{\partial t}(\alpha_q \rho_q \vec{v}_q) + \nabla \cdot (\alpha_q \rho_q \vec{v}_q \vec{v}_q) = -\alpha_q \nabla p + \nabla \cdot \bar{\bar{\tau}}_q + \alpha_q \rho_q \vec{g} + \sum_{p=1}^{n} (\vec{R}_{pq} + \dot{m}_{pq} \vec{v}_{pq} - \dot{m}_{qp} \vec{v}_{qp}) + (\vec{F}_q + \vec{f}_{lift,q} + \vec{F}_{vm,q}) \tag{3.6}$$

where $\bar{\bar{\tau}}_q$ is the q^{th} phase stress-strain tensor

$$\bar{\bar{\tau}}_q = \alpha_q \mu_q (\nabla \vec{v}_q + \nabla \vec{v}_q^T) + \alpha_q (\lambda_q - \frac{2}{3} \mu_q) \nabla \cdot \vec{v}_q \bar{\bar{I}} \tag{3.7}$$

In Equations (3.6) and (3.7) $\vec{q}$ is the acceleration due to gravity, μ_q and λ_q are the shear and bulk viscosity of phase q, p is the pressure shared by phases, $\vec{R}_{pq}$ is an interaction force between phases, $\vec{F}_q$ is an external body force, $\vec{f}_{lift,q}$ is a lift force and $\vec{F}_{vm,q}$ is the interaction force between phases (Fluent (2010)).

For the simulating of evaporation it is important to note that $\vec{v}_{pq}$ is the interphase velocity with $\vec{v}_{pq} = \vec{v}_p$ if $\dot{m}_{pq} > 0$ and $\vec{v}_{pq} = \vec{q}_p$ if $\dot{m}_{pq} < 0$. Likewise $\vec{v}_{qp} = \vec{q}_q$ if $\dot{m}_{qp} > 0$ and $\vec{v}_{qp} = \vec{q}_p$ if $\dot{m}_{qp} < 0$. The lift force is appropriate for multiphase flows with droplets and bubbles that are far apart and therefore not applicable for simulating evaporation from a wall. The virtual mass force is only significant when the secondary phase density is smaller than the primary phase, which is not the case for the evaporative cartridge model.

3.3.4 PDEC Shaft

The CFD model of a PDEC shaft is required to theoretically simulate the three-dimensional characteristics of each inlet configuration under the same conditions as the experiments. It can further be used as a comparison with the one-dimensional model of the evaporative cartridge section.

FLUENT® can simulate constant rate evaporation with a multiphase model. Evaporation occurs from the liquid surface, resistance to heat and mass transfer takes place in the surrounding air film. The object from which evaporation occurs has a constant temperature. The phases for simulating water evaporation are air, water vapour and liquid water. The mechanisms of evaporation was discussed in Section 3.1. FLUENT® allows for mass transfer from the liquid water to the gaseous phase above a specified saturation temperature and at a specified evaporation rate.

$$\frac{\partial}{\partial t}(\alpha\rho_v) + \nabla \cdot (\alpha\rho_v\vec{V}_v) = \dot{m}_{l\to v} - \dot{m}_{v\to l} \tag{3.8}$$

where α is the vapour volume fraction, $\vec{V}$ is velocity and the subscripts v and l represent the vapour and liquid phases. The mass transfer can be described by Equations(3.9) and (3.10).

$$\dot{m}_{l\to v} = coeff * \alpha_l\rho_l\frac{(T_l - T_{sat})}{T_{sat}} \quad for \quad T_l > T_{sat} \tag{3.9}$$

$$\dot{m}_{v\to l} = coeff * \alpha_v\rho_v\frac{(T_v - T_{sat})}{T_{sat}} \quad for \quad T_v < T_{sat} \tag{3.10}$$

where $coeff$ is a coefficient that can be interpreted as a relaxation time and T_{sat} is the saturation temperature. The source term for the energy equation can be obtained by multiplying the rate of mass transfer by the latent heat. Gullman (2010) states that a User Defined Function (UDF) can be used to specify the mass transfer rate at a specific temperature. This model is used to compare with the results from the one-dimensional model, as shown in Section 5.3.

Another approach is to assume a specific boundary condition at the walls of the evaporative cartridge. FLUENT® allows for species mass fractions to be specified at domain inlets, outlets and walls. A temperature and humidity gradient can therefore be specified at the cartridge walls. This provides an increase in vapour mass at the walls along with an eventual temperature decrease at the cartridge walls. The gradients can be taken from the evaporation model to increase accuracy of the results. This method offers stability and is used for comparison with the experimental data when a model incorporating evaporation cannot reach convergence under the prerequisites set in Appendix C. This method will prevent the model from reaching high accuracy results.

3.3.5 Solar Chimney

In a solar chimney, heat is transferred from chimney walls to the air inside the chimney. The heat flux along the length of the chimney is not constant, as the walls are not heated uniformly along the length. A temperature gradient

can be specified along the length of the chimney. Temperature measurements from experimental data can be taken and a polynomial curve fitted to them, as shown in Appendix D. This curve can then be specified in an UDF and fitted as a boundary condition to the walls of the chimney in the theoretical model.

3.3.6 Rotating Configurations

FLUENT® provides two models to provide steady state solutions for single rotating reference frame setups. The first is the Mixing Plane Model, which can not be used when the models for species transport is enabled. The second is Multiple Reference Frame (MRF) Model and is the simplest approach of the two models for multiple zones. It is a steady-state approximation in which individual cell zones move at different rotational speeds. At the interfaces between cell zones, a local reference frame transformation is performed to enable flow variables in one zone to be used to calculate fluxes at the boundary of the adjacent zone (Fluent (2010)). During calculation of the MRF model the grid remains fixed. The motion of the moving part is therefore frozen and the instantaneous flow field is calculated. This provides a solution for the current flow field and does not take the changing orientation of the configuration with time into account. Averaging values from simulations at different orientations will allow for a more accurate prediction of the flow field.

3.3.7 Assumptions in Modelling

It is assumed that a steady state solution exists for the PDEC and solar chimney models. This corresponds with observations during testing, but is still an approximation. It is assumed that the liquid in the cartridge and the evaporated liquid are in equilibrium at the surface of the cartridge. It is further assumed that there is no transport of moisture within the cartridge itself. The liquid at the interface is considered unbound, meaning the liquid will behave like free liquid not absorbed into the material in any way. It will therefore exert a vapour pressure equal to that of free liquid, with corresponding enthalpy difference between liquid and vapour. It is assumed that a boundary layer of stagnant gas exists adjacent to the surface of the cartridge. The evaporation process is assumed to be entirely limited by the diffusion in the boundary layer film.

A whole-domain approach was used where the inside domain (PDEC and solar chimney) was modelled along with the outside domain (the "roof" of the building and the air over it). A domain with a breadth of 1 m, height of 1 m and a length of 3 m was modelled over the PDEC shaft and the solar chimney, with the inlet to the domain situated 1.5 m away from the centre of the shaft or chimney. A velocity boundary condition was set at the domain inlet to simulate wind flowing over the "roof" surface. The remaining boundaries of

the domain was set as pressure outlets where air could flow out freely. The "roof" was assumed to be flat and the wind profile was assumed to be fully developed and uniform. Wind speed is normally zero at ground level and increases with height. This was taken into account in the CFD models with the wind inlet specified at 1.5 m from the configuration placement. Lastly, it was assumed that steady-state atmospheric conditions exist at the model inlets and outlets.

3.3.8 Modelling procedure

The modelling procedure of the solar chimney consisted of convergence checking and mesh refinement, as specified in Appendix C. The following procedure was used when modelling the inlet configurations on the PDEC shaft:

1. Calculate Reynolds or Rayleigh numbers for case and determine if flow is laminar or turbulent (laminar and turbulent regions in flow field will vary, but domain is not divided into zones).
2. If flow is deemed turbulent, use the k-ϵ turbulence model.
3. Model the flow field first by excluding energy and species from calculations.
4. Check residuals for convergence (as specified in Appendix C) and refine grid.
5. Solve energy and species.
6. Set reaction rate in increments from low to high, checking residuals until convergence reached and solution approaches reality (i.e. saturated air at cartridge surface).

3.4 Inlet Configuration

Air-conditioning systems require a mechanical fan driven by an electric motor to move air through an enclosed space. Electricity usage adds to the costs of using such a system. A natural source of kinetic energy, as discussed in Section 2.1.1, is wind energy. Since the supply of wind energy is not constant throughout the desired hours of operation, an inlet design that functions for both still standing and windy conditions (Pearlmutter *et al.* (1996)) is required.

3.4.1 Procedure for Choosing Best Inlet

One of the aims of this project was to determine an inlet configuration that is capable of maximising airflow into the PDEC shaft at various wind speeds. Flow separation at the inlet is a problem, as the flow of air separates from the horizontal "roof" and causes a turbulent region in the shaft. An inlet

configuration should be able to induce flow with windy conditions and flow separation, and not obstruct flow with non-windy conditions. The inlet configuration that was built with this aim in mind is called the Turbine Fan Inlet (TFI). A description of the TFI configuration, along with descriptions of similar previously patented configurations, is given in Appendix E. The TFI configuration, along with an Open-ended configuration, the DSI configuration (tested by Swiegers (2012)) and a dome shaped configuration were tested. The four inlet configurations are shown in Figure 3.11.

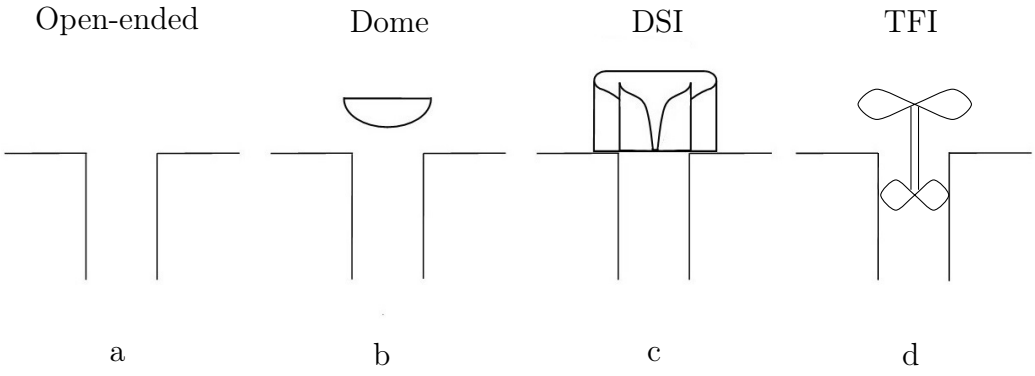

Figure 3.11: Inlet configurations for testing

The inlet configurations were tested on a 500 mm diameter, 4.8 m high PDEC shaft. Air was blown across the inlet at various speeds to determine the capability of the configuration to force air into the PDEC shaft. Tests were done with a wet and a dry evaporative cartridge. The change in volume flow rate, temperature and inlet energy loss coefficient were measured or determined for each test. The best inlet shape for a PDEC, from the tested configurations, could then be determined from comparing and interpreting the measured values.

3.4.2 Inlet Loss Coefficient Determination

The inlet energy loss coefficient is a measure of the efficiency of an inlet to channel flow into the shaft. It is therefore necessary to determine a loss coefficient for each inlet in order to determine the best shape. In order to obtain loss coefficients a testing setup had to be built. The space that housed the testing setup is shown in Figure 3.12. A heat exchanger can be used to thermally control the space. The PDEC shaft was installed next to a catwalk that allows access to the top of the shaft. A diagram of the testing setup is shown in Figure 3.13. The testing setup was designed so that air flows from the thermally controlled space through an inlet configuration into the PDEC shaft. It

then flows through an evaporative cartridge and further down the shaft, were it evacuates out to the thermally controlled space. A mechanical fan blows air through a flow straightener over the inlet configuration to simulate wind.

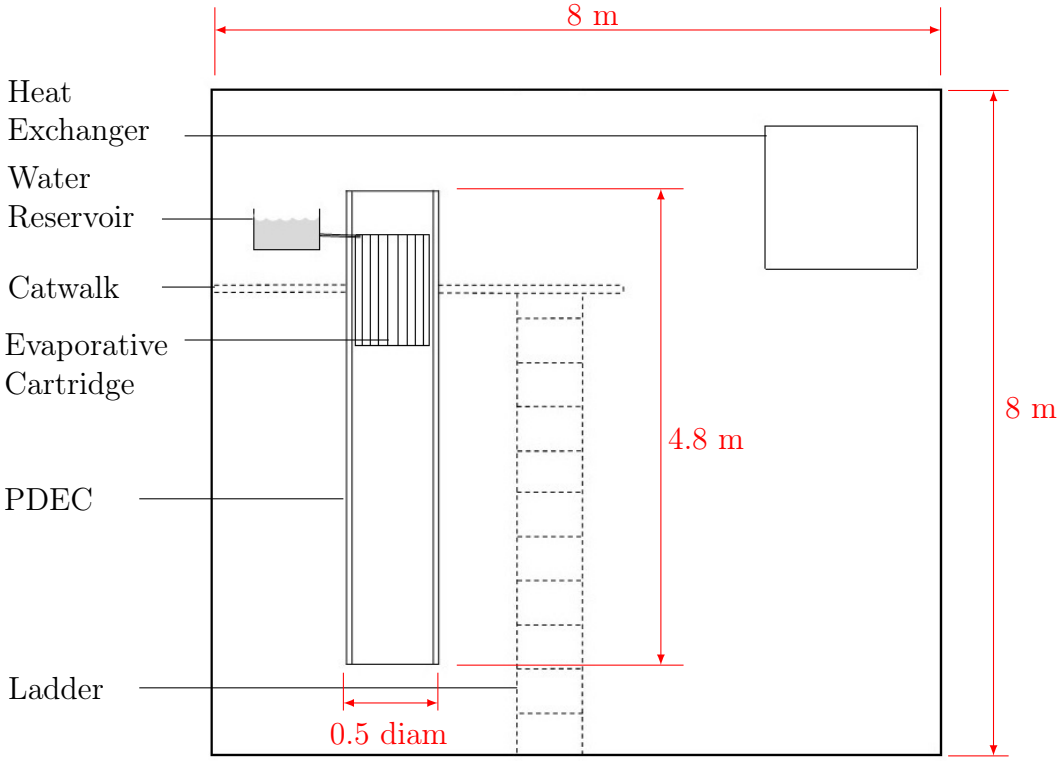

Figure 3.12: Thermally controlled space with PDEC and Heat Exchanger

The characteristics in mechanical wind differ from natural wind in that it consists of eddies in various different sizes, were natural wind is mainly dominated by large eddies. A mechanical fan is however capable of blowing a consistent volume flow of air over the configuration for a long period of time. This consistent flow of air enables measurements to be taken at steady-state conditions.

Cengel (2006) provides an equation that can be used to determine the inlet loss coefficient. Equation (3.1) is known as Bernoulli's equation.

$$P_i + \frac{\rho_i {V_i}^2}{2} + g\rho_i z_i = \sum_{i=1}^{n} k_L \frac{\rho_e {V_e}^2}{2} + P_e + \frac{\rho_e {V_e}^2}{2} + g\rho_e z_e \tag{3.1}$$

where P is the static pressure head, ρ is density, V is velocity, g is gravitational acceleration, k_L is the loss coefficient and the subscripts i and e represent

the inlet and exit of the testing setup. For Equation (3.1) the inlet is considered at P0 and the exit at P5.

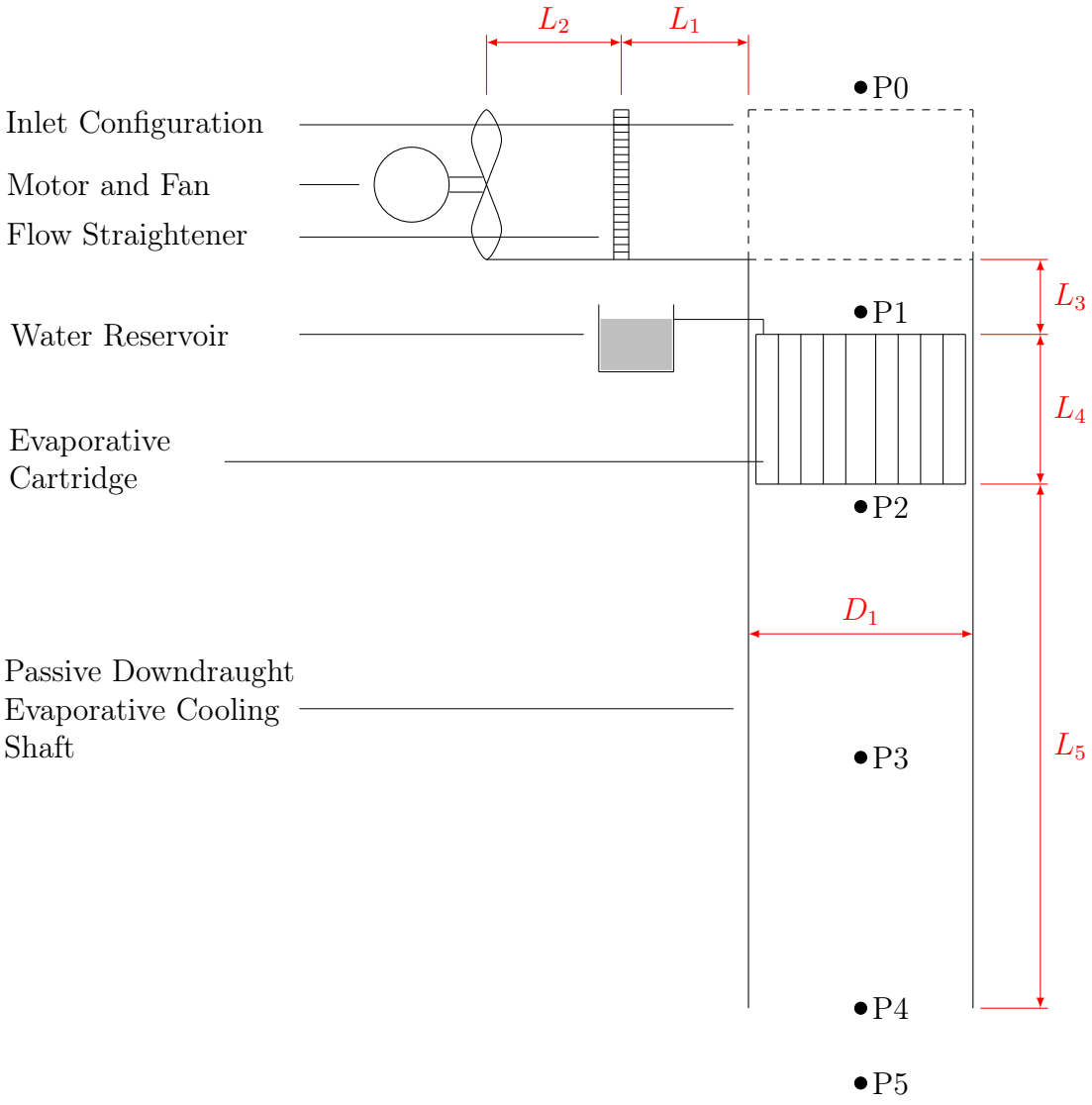

Figure 3.13: Setup to determine inlet loss coefficients

3.5 Outlet Configuration

Air exiting the solar chimney possesses kinetic energy due to heating from the solar chimney walls. The exiting air has upwards momentum when exiting the solar chimney. In an environment with no wind the air will move upwards forming a plume of hot air as it exits the chimney (dos S Bernardes *et al.* (2003)). Sreenivas and Prasad (2000) describes plumes as being buoyancy

driven unbounded flows which develop in open ambient fluid. Plumes spread by the process of entrainment in which irrotational ambient fluid is incorporated into the turbulent region. The kinetic energy in the hot air is eventually dispersed to the cold environment. This change in flow cross section and flow direction constitutes towards a minor loss or a head loss (Cengel (2006)).

3.5.1 Procedure for Choosing Best Outlet

The minor loss at the outlet of a pipe is greatest when the expansion at the outlet is sudden (Yokota (2012)). Increasing the chimney diameter without changing the volume flow rate through the chimney will therefore lead to a smaller loss coefficient. One possible way to do this is to install a diffuser at the outlet which assists in gradually increasing the outlet diameter. Another way to decrease the minor loss is to create a low pressure point near the outlet that sucks air out of the chimney. This can be achieved by positioning a dome near the outlet which creates a low pressure point near the concave surface as air flows over it.

An outlet design currently being mass produced is a turbine extractor configuration called the *Whirlybird*. Wind blows over the *Whirlybird* and turns the turbine, sucking air out of the chimney. The *Whirlybird* eliminates the effects of flow separation due to the flow of wind over the outlet hole.

The TFI configuration can be used as an outlet configuration by reversing the fan and the turbine as shown in Appendix E. The four outlet configurations considered in this study are the Open-ended, Dome, *Whirlybird* and Turbine Fan Outlet (TFO) as shown in Figure 3.14.

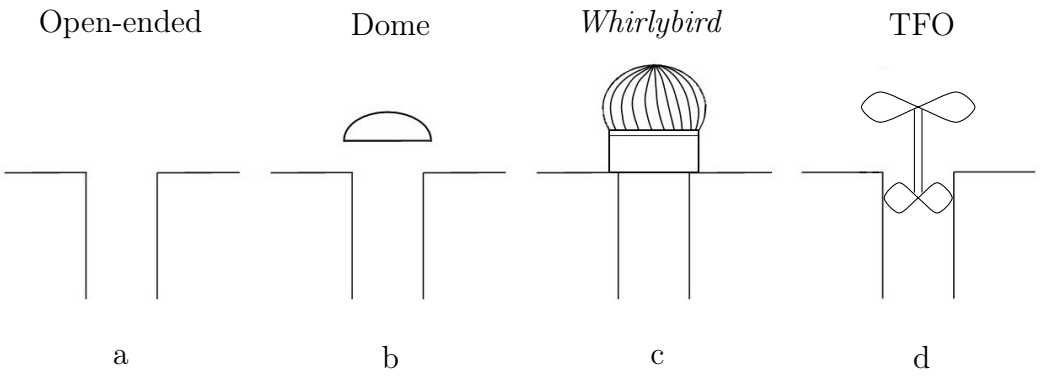

Figure 3.14: Outlet configurations for testing

The outlet configurations were tested under the same conditions as the inlet configurations. Wind was blown over the outlet configuration at different speeds. Tests were conducted on a chimney with heated and without heated

walls. The same measurements were taken as for the inlet configurations and the best outlet shape, from the tested configurations, for a solar chimney could then be determined by comparing and interpreting the measured values.

3.5.2 Outlet Loss Coefficient Determination

The outlet energy loss coefficient is a measure of the outlet's ability to extract air from the chimney. The outlet loss coefficient for each configuration was determined in a similar manner as for the inlet configurations. Pressure and velocity measurements were taken at points along the chimney and configuration to determine the loss coefficient. A solar chimney testing setup was built to determine the loss coefficients and is shown in Figure 3.15.

Air inside solar chimneys operating in real conditions are heated by solar radiation heating the chimney walls. Radiation enters through a glass wall and heats the walls inside the solar chimney. Heat is then transferred to the air inside the chimney. The testing setup is designed to heat the walls of the solar chimney. This is done by building concentric chimney walls and heating the air in between the tube walls. The air between the inner tube walls is then heated. Heat is transferred from the chimney walls to the air inside the chimney which creates an updraught. The walls are heated all along the perimeter of the chimney which causes an axi-symmetric temperature increase of the air in the solar chimney. The chimney was designed axi-symmetrically so that measurements could be taken with more precision and to better compare the experimental results with theoretical CFD results.

A fan blowing air at an outlet configuration through a flow straightener is positioned at the top of the chimney at the same location as for the inlet configuration testing setup. Outlet configurations are then placed at the top of the solar chimney and measurements are taken at various operating conditions. The best outlet can then be determined from calculating outlet loss coefficients using Equation (3.1).

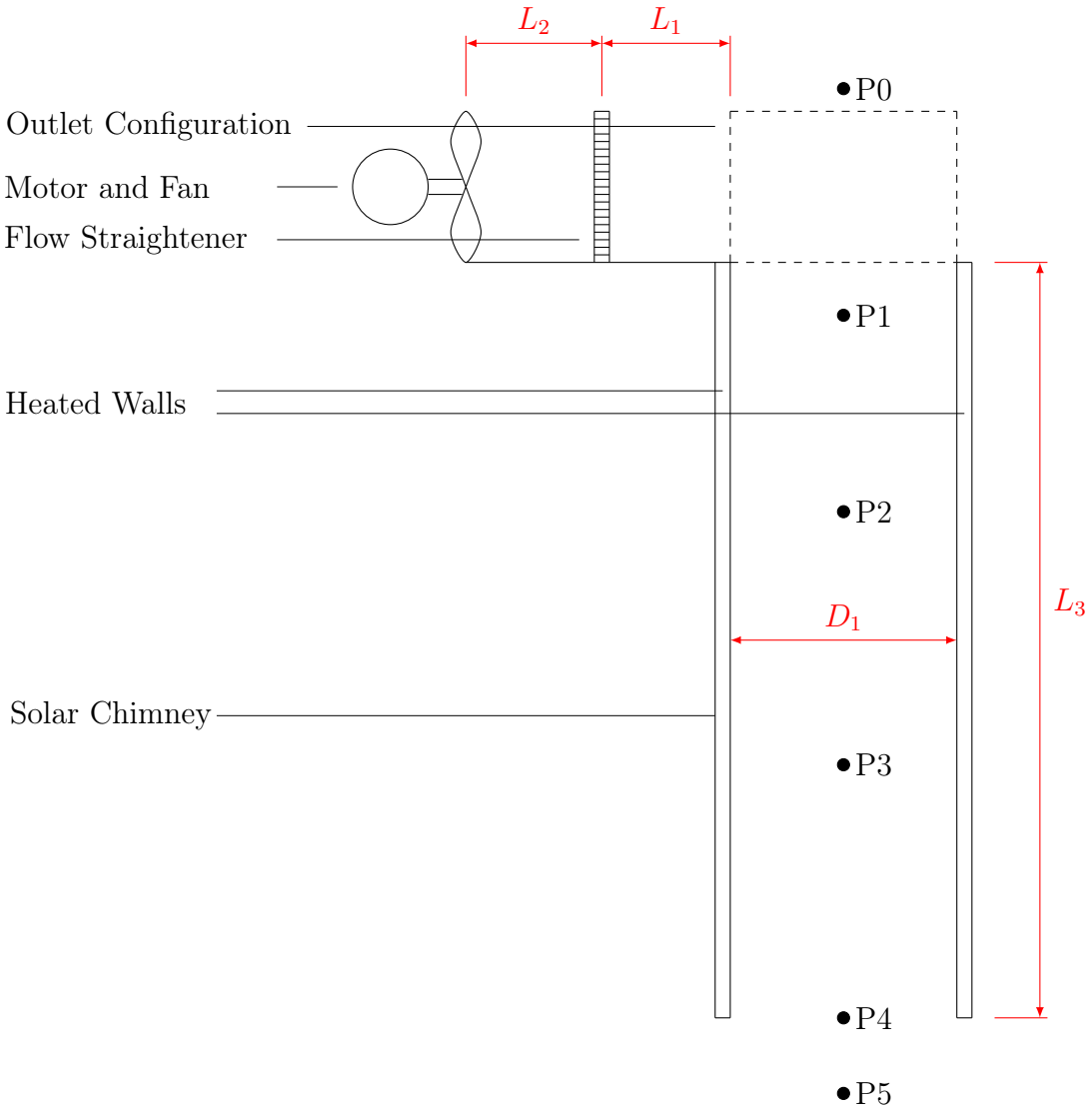

Figure 3.15: Setup to determine outlet loss coefficients

4 Experimental Work

In this section the experimental work is discussed. The testing setup as discussed in Section 3.4.2 and Section 3.5.2 was constructed. A large scale, 500 mm diameter and 4.8 m high, PDEC and solar chimney testing setup was built in order to obtain velocity, pressure and temperature measurements for a natural ventilation system for each inlet and outlet configuration. These measurements were used to obtain loss coefficients and to compare ventilation capabilities for each configuration for a wide range of operating conditions.

4.1 PDEC Testing Setup

A basic layout of the PDEC test setup is described in Section 3.4.2 (Figure 3.13). The PDEC shaft consists of an evaporative cartridge surrounded by a outer cylindrical wall. The various inlet configurations tested (see Figure 3.11) are placed at the top of the PDEC shaft close to the evaporative cartridge. A fan is situated at a specified distance from the inlet of the PDEC and used to simulate wind. A honeycomb structured flow straightener is placed between the fan and the inlet configuration, which provides a uniform flow field over the inlet configuration. Real wind does not have a uniform flow field, therefore the flow straightener is used to enable comparison of results with a theoretical model. The flow straightener had honeycomb shaped cells with a 3.175 mm dimension between parallel sides of the cells and was 31.75 mm thick in the direction of airflow.

To build the evaporative cartridge various materials were tested for their wettability. It was decided to test only cotton as it has a high capacity to hold water and, for safety reasons, it is not prone to catch fire. The results of the wettability tests are shown in Table 4.1. It was decided to build the cartridge from 100 % cotton (b grade), white bull denim.

The evaporative cartridge section was built as per the specification given in Section 5.1 with $L_4 = 1$ m. The finished evaporative cartridge is shown in Figure 4.1. A series of concentric wire-meshes were made from wiring together a 250x250x1 mm wire mesh. The concentric wire meshes have linearly decreasing diameters from the outer mesh. The outer mesh has a diameter of 500 mm. Each meshed-shell was then jacketed on both sides with the chosen

Table 4.1: Materials tested for evaporative cartridge

Material	Wetted Height
Nylon,Cotton 1	405 mm
Nylon,Cotton 2	380 mm
Nylon,Cotton 3	310 mm
100% cotton slub weave dual purpose	220 mm
100% cotton 2 way slub weave monsoon, ivory Prepared for Printing RISS, HM	260 mm
100% cotton b grade, white bull denim shrinkage unknown DGT, CAGS	410 mm

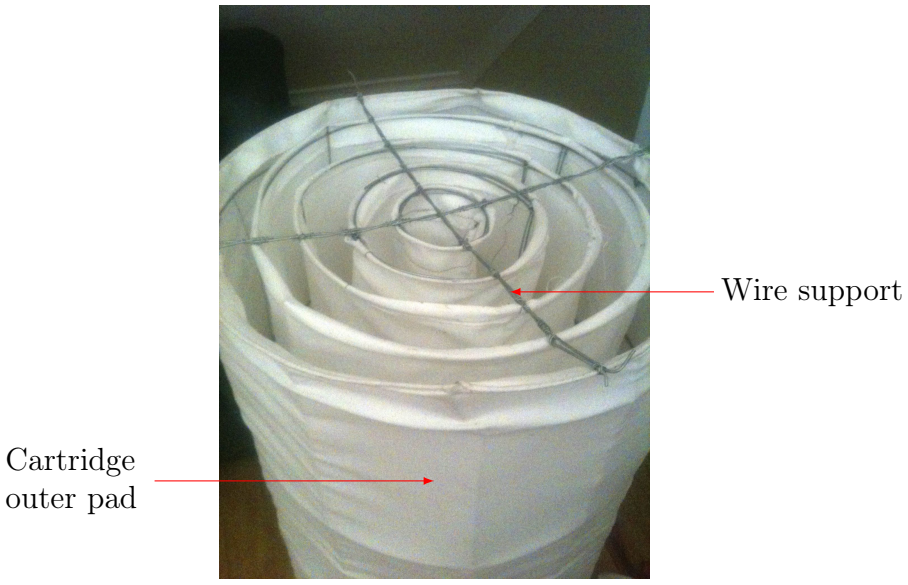

Figure 4.1: Evaporative cartridge with concentric evaporative pads

cotton cloth. Each concentric pad was then strengthened with two 2 mm steel wires along the length of the pad, to provide rigidity.

The PDEC shaft was built to fit specifications outlined in Figure 3.13. The shaft wall was made from 0.5 mm acrylic sheet that was wrapped around a 4.8 m high, 0.5 m diameter mesh (galvanised steel 50x50 mm, 2 mm wire thickness). The mesh was rolled into four cylinders of $D_1 = 0.5$ m joined together at the top and bottom to form one 4.8 m shaft with $L_3 = 0.5$ m and $L_5 = 3.38$ m, as shown in Figure 3.13. A large wooden bracket made from laminated pine was built to hold the shaft in place. A hole, with the same diameter as the shaft, was cut from the top of the wooden bracket along with

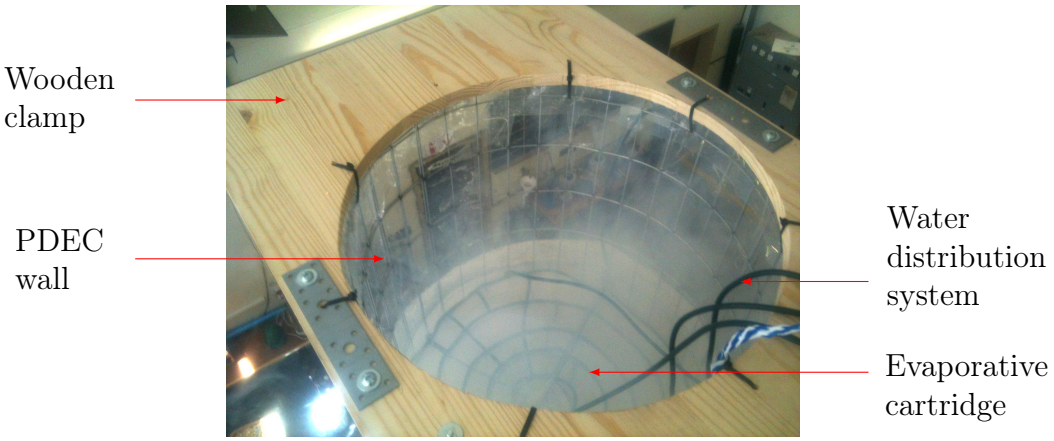

Figure 4.2: Smoke entering the wooden bracket holding the PDEC shaft in place

eight equaspaced holes around the perimeter. Cable ties with 4 mm width were then looped through the holes and the mesh structure of the shaft. Two 2 mm × 35 mm × 175 mm aluminium plates were bolted along the narrow edges of the bracket, next to the hole for the shaft, to add strength under tension. The bracket was then clamped onto a 6 m high catwalk, shown in Figure 3.12. A High Velocity Floor Fan (model: IF450) was used to simulate wind blowing over the configuration.

A Z-500 DIXON smoke machine was used to visually inspect the flow patterns for each configuration. Figure 4.2 shows smoke entering the top of the PDEC shaft. A water distribution system was installed on top of the evaporative cartridge to continuously wet the pads when testing. Green water pipes (type: HDPE100) were coiled all along the evaporative pads and small holes were cut along the bottom of the tubes to leak water onto the pads. Three tubes were attached to the coil on the outside evaporative pad to provide an even distribution of water to the cartridge. Taps were installed in the three tubes providing water to the cartridge. The tubes were attached to a 50 liter bucket which was placed 0.7 m above the cartridge to provide enough pressure to ensure downwards flow of water. The water level in the bucket was used to measure the volume flow rate to the cartridge.

Inlet configurations were installed in the space above the PDEC shaft, on top of the wooden bracket. The DSI and TFI configurations were simply placed on top of the bracket, while the Dome inlet was kept in place by attaching cable ties to it and looping 0.7 mm steel wire through it. The steel wires were attached to an existing overhead structure and the wooden bracket. The Dome was fastened at a height of 7 cm above the top of the wooden bracket.

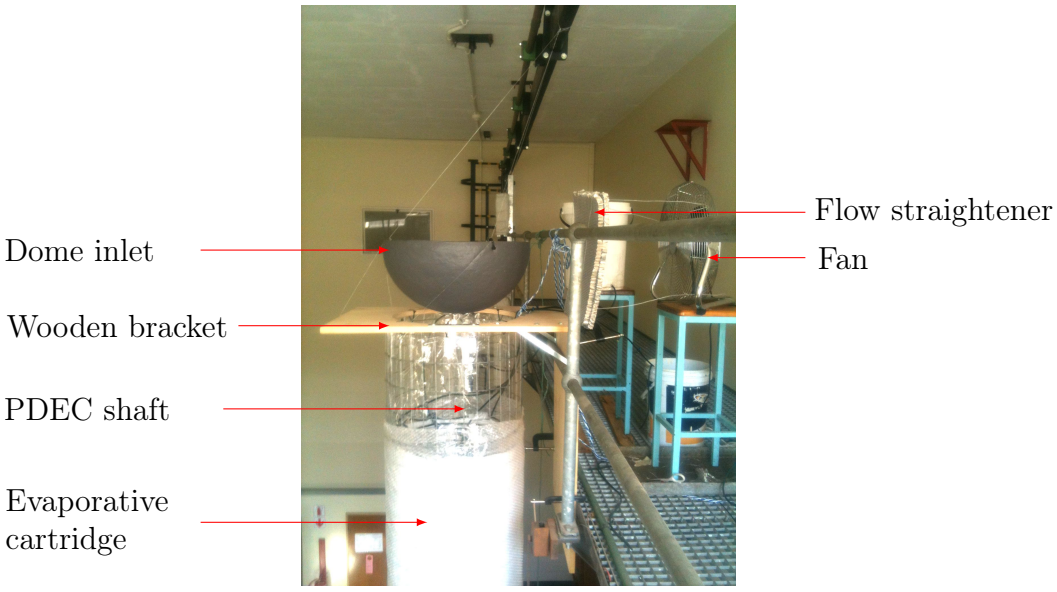

Figure 4.3: Dome configuration operating over PDEC shaft

The Dome inlet over the PDEC shaft can be seen in Figure 4.3. The Dome was made by spraying polyurethane into a dome-like shape and then grating it down to its final form. The surface of the Dome was then smeared with wood glue in order to smooth the surface. It was then painted with Duran Roofkote Pure Acrylic Roof Paint.

The DSI configuration was made from cutting and grating polystyrene into a cone shape. The cone was then smeared with silicon to smooth the surface. The guide vanes were made from cardboard with the intention to keep the configuration as light as possible. It was then attached to the cone with a combination of wood glue and silicon. The configuration was then painted with the Duran Roofkote Acrylic paint. The TFI configuration was made from mainly 0.9 mm aluminium sheet metal. Details on the construction of the TFI inlet is provided in Appendix E.

4.2 Solar Chimney Testing Setup

The basic layout of the solar chimney testing setup is described in Section 3.5.2 (Figure 3.15). The chimney was built with the same total chimney length as the PDEC shaft. The solar chimney consists of concentric cylindrical walls. The walls were made from the same wire mesh and plastic as was used for the PDEC shaft. The same positioning of the wind producing fan and flow straightener is used as for the PDEC testing setup. Outlet configurations are

placed at the top of the solar chimney and measurements taken at various operating conditions to determine outlet loss coefficients.

Figure 4.4 shows the hairdryers (used to heat the chimney walls) placed at the bottom of the solar chimney, between the concentric walls. The hairdryers are 239 V, 1800 W, Model no: RHHD21 Russel Hobbs with two wind speed and two "level of heat" settings. The settings chosen for the tests are discussed in Appendix F. The gaps between the hair dryers and between the concentric walls at the top of the chimney were sealed with plastic tape to prevent air from escaping. A small cut was made in the plastic near the top of the chimney so air could escape. The chimney was attached to the same wooden bracket as discussed in Section 4.1.

Outlet configurations were installed in the space above the solar chimney on top of the wooden bracket. The TFO configuration were placed on top of the solar chimney and secured with 0.5 mm steel wires. The Dome outlet was fastened in a similar manner as it was installed for the inlet configuration, with three concentric 0.5 mm steel wires positioning it in place. The same Dome configuration was used for the outlet as was used for the inlet. The Dome was fastened at a height of 7 cm above the wooden bracket. The TFO configuration was constructed with the parts used for the TFI configuration. The fan, turbine and guide walls were reversed so that the fan forces air out of the chimney. The specific *Whirlybird* that was used is a Windmaster Tornado 500 mm Wind Turbine. Figure 4.5 shows the *Whirlybird* configuration operating over the solar chimney test setup.

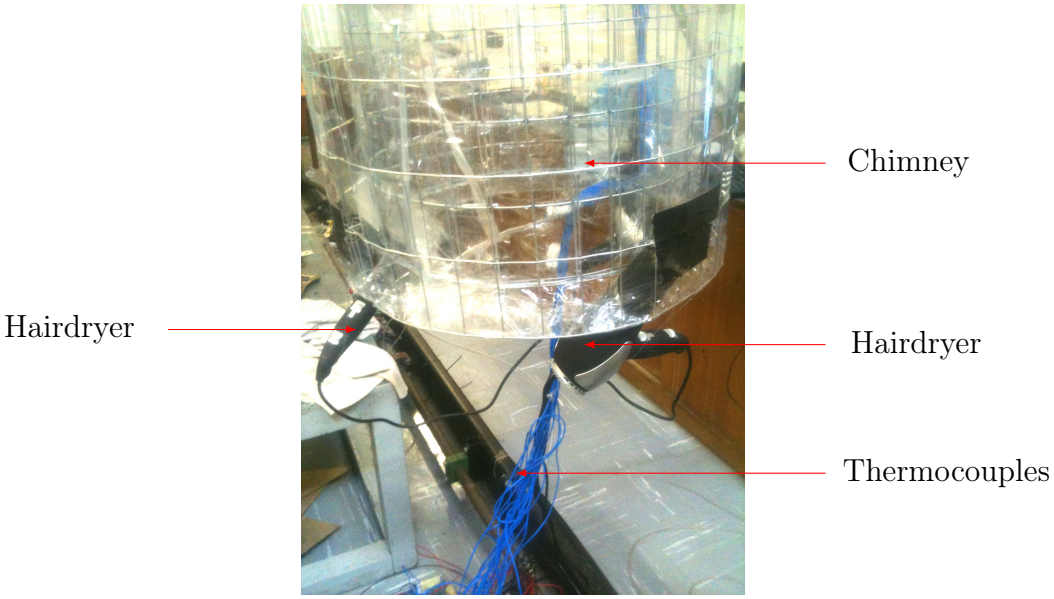

Figure 4.4: 1800 W Russel Hobbs hairdryers used to heat solar chimney walls

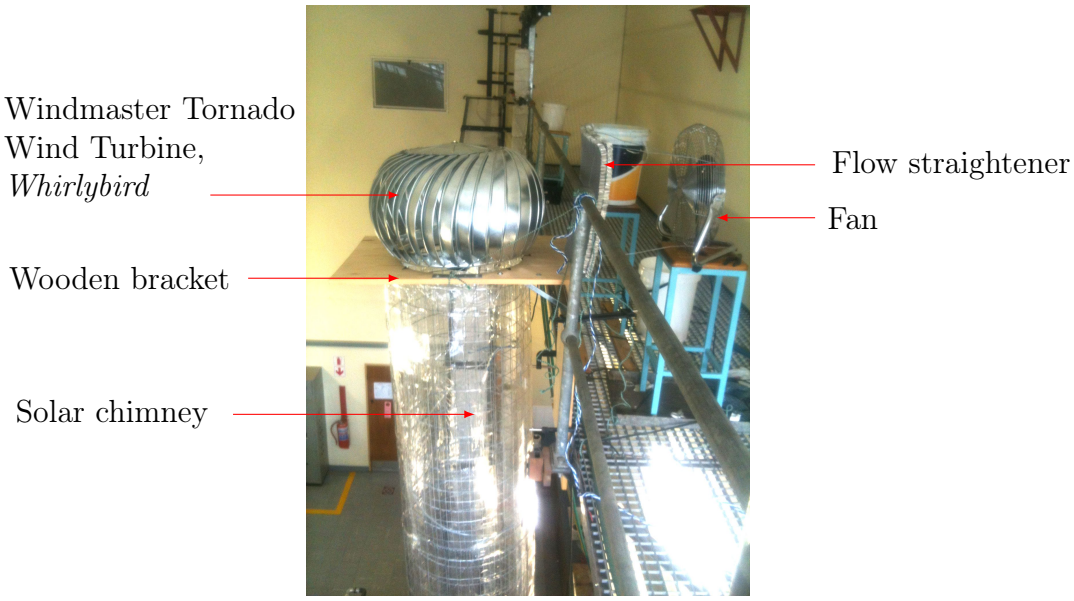

Figure 4.5: *Whirlybird* configuration operating over solar chimney

4.3 Measurement and Data Acquisition

A BETZ Manometer was used to measure the pressure differences across the wind tunnel. A ROTOTHERM Flowmeter Anemometer was used to manually measure wind speeds at the top and bottom of the PDEC and solar chimney experimental setups. Several velocity measurements across the diameter at the point of measurement were made in order to obtain an average velocity for that point. Table 4.2 provides the make, model and serial numbers of the equipment used to capture the experimental pressure and velocity data. The calibration of the thermocouples (T-type) used to measure dry- and wet-bulb temperatures across the PDEC and solar chimney are shown in Appendix G.

4.4 Experimental Procedure

The experimental procedure for the PDEC and solar chimney testing setup were similar. A "testing in progress" sign was displayed outside the thermally controlled space, shown in Figure 3.12, to prevent anyone entering and altering the conditions in the space. Any deviations from the experimental procedure, for solar chimney testing, are shown in brackets as follows.

Table 4.2: Measurement equipment for experiments

Make	Model	Serial Number
AGILENT Data Acquisition/ Switch Unit 34970A	34970A	S/N MY440511115
AGILENT plug-in switch card	34901A	S/N MY50060822
AGILENT USB/GPIB cable	823575B	MY49450589
SENTRY hotwire Anemometer	ST732	S/N 1047000890
ROTOTHERM Flowmeter Anemometer	L10171/2	US37047554
Anemo-phychrometer and BTU-phychrometer	R5232	US9635723
BETZ Manometer 5000	221949	MY41087800
Z-400 DIXON Smoke Machine	D15342	S/N DN 1105010472
Lenovo IdeaPad	Y570	CB11264459

1 Check that all windows and doors are closed, as an external draught can influence the results.
2 Put on safety equipment and inform nearby technicion of the intention to work at heights.
3 Install the inlet or outlet configuration concentrically on top of the chimney and make sure that it is secure.
4 Switch on data logger and computer to store data and start logging process.
5 Wet evaporative pads and cloths where the wet bulb temperatures are measured. (Only wet cloths for solar chimney tests and start hairdryers on correct setting. Wait 30 min until chimney temperature is at steady state.)
6 Switch on fan with required speed setting if it is a wind simulation.
7 Measure velocity at top and bottom of PDEC shaft or chimney at various points along the diameter and log on computer spreedsheet.
8 Measure pressure drop over PDEC shaft or chimney and log on spreedsheet.
9 Stop data logger if all required measurements have been taken and written down.
10 Reset fan to different speed setting if different speed setting is required.
11 Restart data logger and retake all required measurements.
12 Switch off and unplug fan if tests are complete. (Switch off and unplug hairdryers.)
13 Remove inlet or outlet configuration from the PDEC shaft or chimney.

4.5 Error Analysis

The error for all test results are found using the following analysis:

$$\delta D = \sqrt{\left(\frac{\delta D}{\delta X_1}\right)^2 \delta\left(X_1^2 + \left(\frac{\delta D}{\delta X_2}\right)^2 \delta X_2^2 + \ldots} \tag{4.1}$$

where the parameter D is a function of independent variables X_1, X_2, etc. δD is the total error and δX_1, δX_2, etc., are the uncertainties of each independent variable. Derivatives can be obtained for the measured data error analysis and a final parameter error can be obtained, as given in Appendix H.

The uncertainties of all the experimental parameters are presented below in Table 4.3. The uncertainty assosiated with area, A_{rel}, could not be calculated in a striaghtforward manner and were estimated. The greatest uncertainty were with the thermocouple probe accuracy, T_{pr}, with a uncertainty of $\pm 1\,\%$, which at a temperature of $25°C$ is $4\,\%$.

Table 4.3: Uncertainties of independent variables

Independent variable	Uncertainty
T_{pr}	$\pm 1°C$
T_{ven}	$\pm 0.2°C$
V_{pr}	$\pm 0.03 m/s$
V_{read}	$\pm 3\,\%$
P_{rel}	$\pm 1\,\%$
ρ_{rel}	$\pm 1\,\%$
A_{rel}	$\pm 0.001\,\mathrm{m}$

For example, to calculate the error in the volumetric flow rate measurement at an air speed of $0.43\,\mathrm{m/s}$, were $G_e = A_e V_e$. The derivatives are

$$\frac{\partial G_e}{\partial V_e} = \frac{G_e}{V_e} \tag{4.2}$$

$$\frac{\partial G_e}{\partial A_e} = \frac{G_e}{A_e} \tag{4.3}$$

Thus the error is

$$\frac{\delta G_e}{G_e} = \sqrt{\left(\frac{\delta V_e}{V_e}\right)^2 + \left(\frac{\delta A_e}{A_e}\right)^2} = \sqrt{\left(\frac{0.04129}{0.43}\right)^2 + \left(\frac{0.001}{0.5}\right)^2} = 4.08\,\% \tag{4.4}$$

4.6 Safety

The risk identification and mitigation procedures associated with the PDEC and solar chimney tests are shown in Table 4.4. A design strategy and safety procedure was implemented to mitigate each identified risk.

Table 4.4: Safety procedure

Risk	Design Impact	Safety Instructions
Falling risk: Tall structure	Build chimney close to ground.	When object (chimney) is hanging do not walk beneath or near the bottom.
	Build chimney light.	Put up warning sign near chimney and wear closed shoes.
	Secure it completely.	Use help from technician when setting up.
Cutting risk: Rotating fan	Install emergency stop	Ensure emergency stop is within reach when testing.
	Fasten fan to stationary structure.	Unplug fan if fastener or structure fail.
Electrocution risk: Wires exposed	Insulate wires	Ensure wire connections are secure before turning power on.
	Group multiple wires and fasten.	Refasten any loose wires.
	Fasten wires and cables away from ground.	Clean up water spillage on ground.
Breaking risk: Incorrect use of equipment	Display visible instructions.	Read instructions and use equipment under supervision of technician.
Falling risk: Working at heights	Build experimental setup near ladder.	Wear safety harness when working on catwalk, as shown in Figure 3.12.

5 Results

In this section the results obtained from experimental PDEC and solar chimney tests are discussed. The experimental results are compared with theoretical results obtained from CFD and one-dimensional models. It was decided to compare each test with the CFD models, as the effects of buoyancy, wind or their combination on the ventilation rates and conditions could be investigated. The one-dimensional model only allows for one non-zero flow direction component and will therefore not necessarily compare well with the experimental results (Lagoudas and Haisler (2002)). Inlet and outlet loss coefficients are experimentally determined for each configuration and, where possible, compared with existing theoretical results.

5.1 Evaporative Cartridge Dimensions

The theory discussed in Sections 3.1.1 to 3.1.5 was used to build a one-dimensional axi-symmetric theoretical model. The model was coded in FORTRAN and ran in FTN95 from Silverfrost Compiler with the Plato Interactive Program Development Environment (IDE). The model was used to determine the optimal dimensions for the evaporative cartridge before construction began. The standards set by Hanley *et al.* (1995) for ASHRAE (American Society of Heating, Refrigerating and Air Conditioning Engineers), were used as a guideline for the required output temperature and humidity of the cartridge. The model was set to simulate a typical hot summers day in Cape Town with operating and outside temperature at 27 °C and a relative humidity of 43 %. Appendix I shows a prediction, by the one-dimensional model, of the performance of a SCAPDEC in South African cities, including Cape Town. Appendix B.1 shows convergence testing of the one-dimensional model.

Figure 5.1 shows the relative humidity distribution for various evaporative cartridge lengths and number of concentric pads. The maximum allowable relative humidity, as set by Hanley *et al.* (1995) for ASHRAE, is shown on the figure. Anything above this maximum relative humidity is therefore not considered as it will not achieve occupant thermal comfort. It was decided to put a radial constraint of 250 mm on the design of the evaporative cartridge to limit variable parameters. This constraint is only a design constraint and

is not present in the one-dimensional theoretical model. The values shown in Figure 5.1 to 5.5 are taken as the average of all the N'th control volumes in the Z direction, as was specified in Figure 3.1. The figure shows that there is an increase in relative humidity with an increase in length and number of evaporative pads. This is because the surface area, from which evaporation can occur, increases and more water vapour can enter the air-vapour mixture. The graph for R = 6 approaches saturation as it becomes more difficult for the air-vapour mixture to carry any more water vapour.

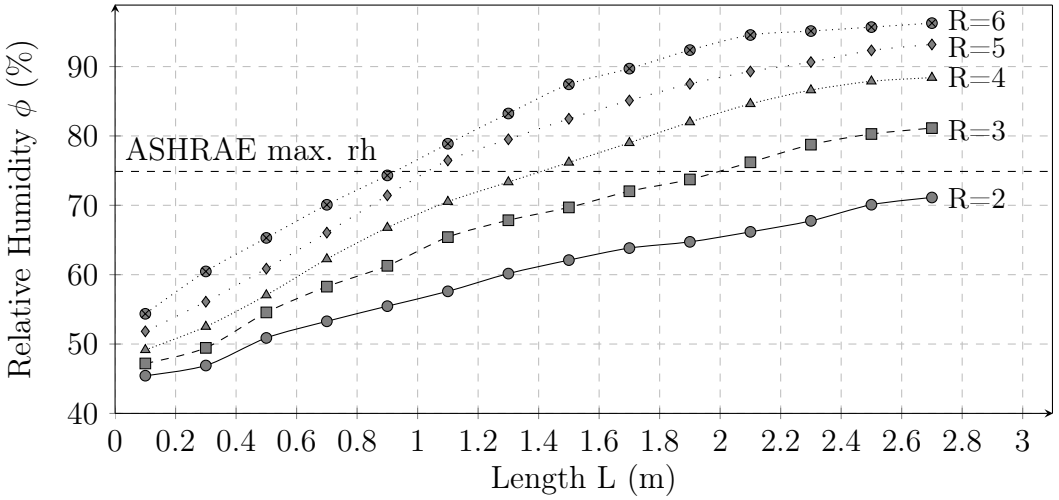

Figure 5.1: Relative humidity comparison of different evaporator cartridge lengths (L) and number of evaporative pads (R) showing the maximum allowable relative humidity set by ASHRAE [$T_{initial}$ and $T_{outside}$ = 27 °C, T_{water} = 16.5 °C, $\phi_i = 43\%$]

An important design parameter is the temperature gradient over the evaporative cartridge, shown in Figure 5.2. The minimum allowable temperature is shown as the dashed line, as prescribed by the ASHRAE maximum allowable relative humidity. The maximum allowable temperature for thermal comfort, as stated by Holm and Engelbrecht (2005) in Section 2.2, is shown on the figure as well. The temperature distribution decreases with an increase in the number of evaporative pads and cartridge length. The figure suggests that there is a minimum allowable temperature to which the air can be cooled with a specific set of design parameters. It is again important to note that the graph for R = 6 approaches saturation and the decrease in temperature becomes zero with an increase in cartridge length.

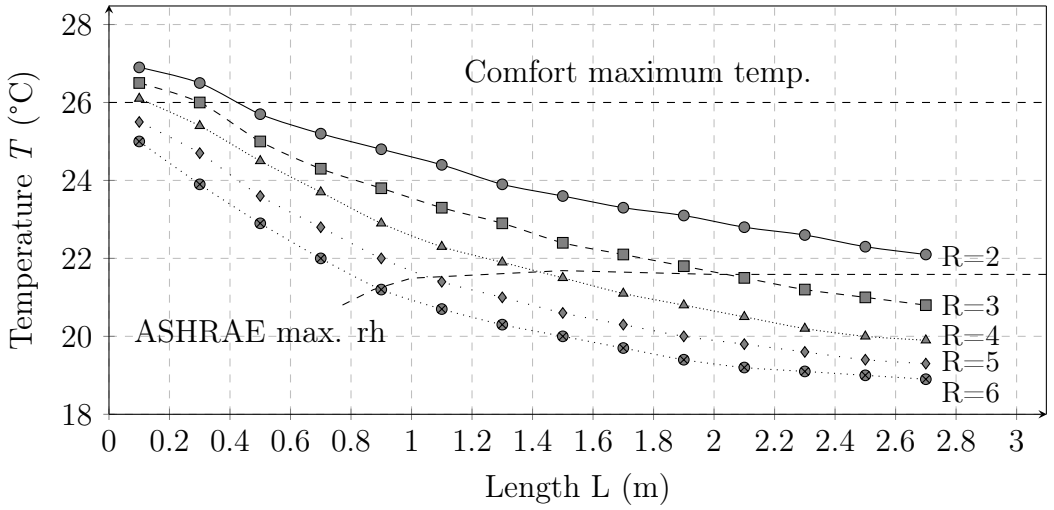

Figure 5.2: Temperature distributions for different evaporator cartridge lengths (L) and number of evaporative pads (R) showing the maximum allowable relative humidity set by ASHRAE [$T_{initial}$ and $T_{outside}$ = 27 °C, T_{water} = 16.5 °C, $\phi_i = 43\%$]

Figure 5.3 shows that the variance in volumetric flow rate is small for different numbers of evaporative pads. There is however an increase in volumetric flow rate with an increase in cartridge length. The mixture mass increases due to more liquid evaporated over a longer length and area in the Z direction. The colder and more dense air sinks downwards at a faster rate, increasing the volume flow rate. The AHSRAE maximum allowable volumetric flow rate has not been shown, because it would not be clear on this figure. For clarity the figure has to be assessed at different sections.

Sections of the volumetric flow rate at different evaporative pad lengths are shown in Figure 5.4. The figure shows that a higher volumetric flow rate is achieved at shorter lengths when with more evaporative pads. If the cartridge length is longer, the cartridge with fewer evaporative pads have a higher volumetric flow rate. For a cartridge of length between 0.7 m and 1.1 m, a maximum volumetric flow rate is achieved if 4 or 5 evaporative pads are present.

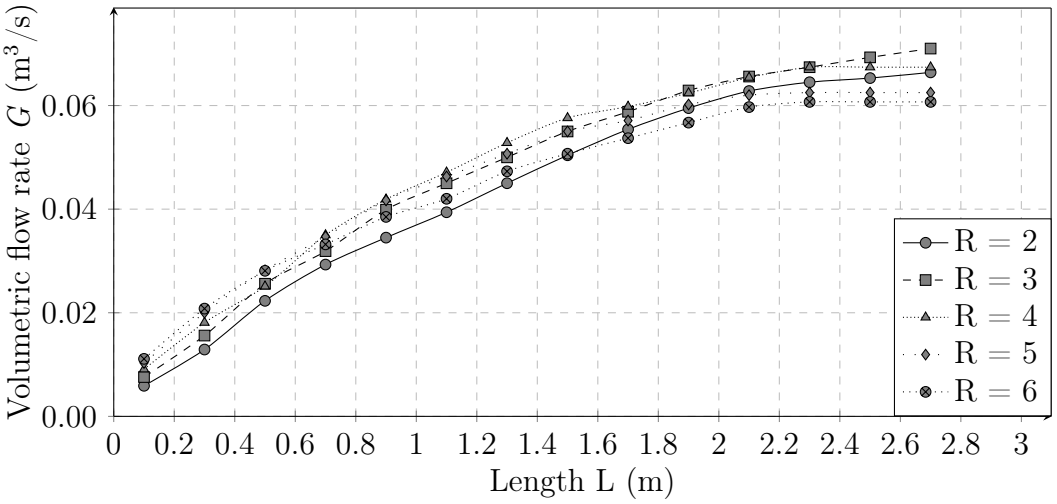

Figure 5.3: Volumetric Flowrate distributions for different evaporator cartridge lengths (L) and number of evaporative pads (R) [$T_{initial}$ and $T_{outside}$ = 27 °C, T_{water} = 16.5 °C, ϕ_i = 43%]

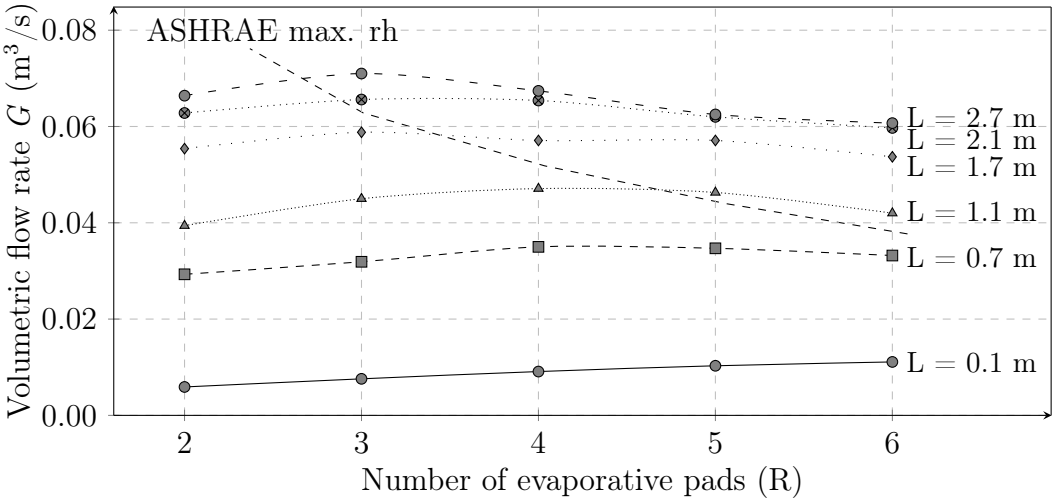

Figure 5.4: Volumetric flow rate distributions at specific cartridge lengths and varying number of evaporative pads (R) [$T_{initial}$ and $T_{outside}$ = 27 °C, T_{water} = 16.5 °C, ϕ_i = 43%]

With the temperature and volume flow rate known, the rate of heat transfer from the liquid to the air can be calculated. The following equation is used to calculate the rate of heat transfer.

$$\dot{Q} = \dot{m} c_p (\Delta T) \tag{5.1}$$

where $\dot{Q}$ is the rate of heat transfer, $\dot{m}$ is the mass flow rate, c_p is the specific heat capacity of air and ΔT is the change in air temperature over the cartridge. The rate of heat transfer indicates the amount of cooling energy transferred and can indicate optimal evaporative cartridge dimensions.

Figure 5.5 shows the rate of heat transfer for various evaporative cartridge lengths and number of evaporative pads. The figure shows that the highest allowable rate of heat transfer is with a 2 m cartridge and R = 3. This value is however misleading in some ways. The one-dimensional theoretical model calculates a state of properties for each control volume and assumes a constant property over the whole control volume. Section 5.3 shows a comparison of the distribution of relative humidity in each control volume of the one-dimensional model and the three-dimensional CFD model. From this it is evident that if the control volume size in the one-dimensional model is too large, the program starts over-predicting results. This problem can not be corrected by minimising the control volume height (in the Z direction), as the model will still produce a one-dimensional result.

A length of 1 m with R = 5 and a diameter of 0.5 m were chosen as the dimensions for the evaporative cartridge. These dimensions were chosen, as they provide maximum allowable rate of heat transfer and can be compared with experimental data with more confidence than a longer cartridge with fewer concentric pads.

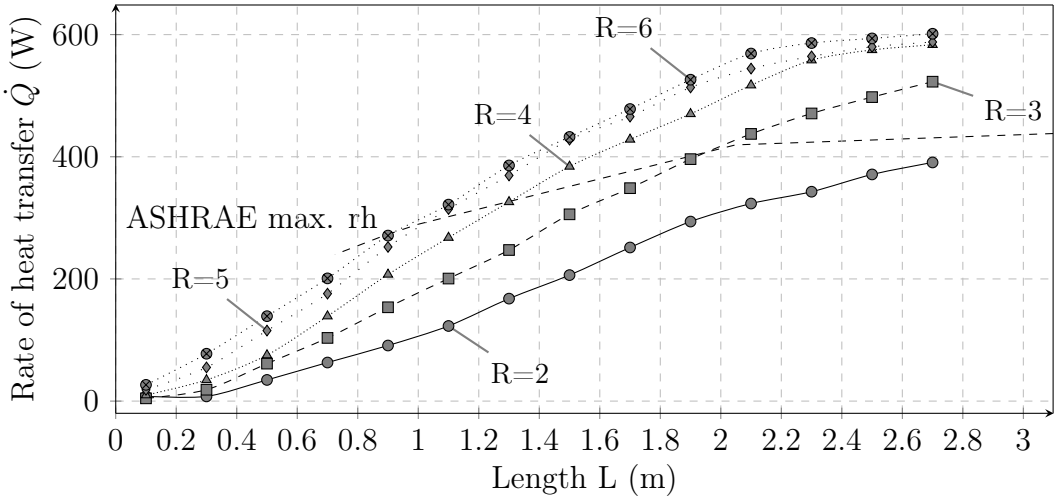

Figure 5.5: Rate of heat transferred with varying evaporator cartridge lengths (L) and number of evaporator pads (R) [$T_{initial}$ and $T_{outside}$ = 27 °C, T_{water} = 16.5 °C, $\phi_{initial}$ = 43%]

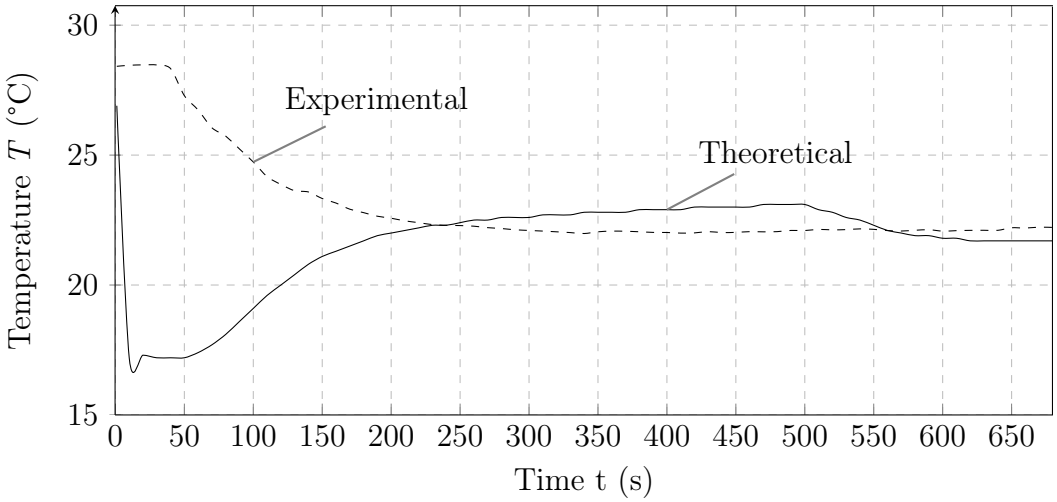

Figure 5.6: Comparison of theoretical with experimental temperature of evaporative cartridge model [L = 1 m, 5 concentric pads, T_{amb} = 27.5°C, $\phi = 43\%$]

5.2 Comparison of One-Dimensional Theoretical Models with Measured Data

The one-dimensional theoretical models are compared with the measured data to check the steady state results of the models. The transient data from the theoretical model and the experiments cannot match, as the theory assumes an initial wall boundary condition from the start of the simulation and the experimental setup takes time to reach this wall condition. The temperature comparisons for the evaporative cartridge and the solar chimney are shown in Figures 5.6 and 5.7. The temperature for the evaporative cartridge represent the mean temperature below the cartridge and the temperature for the solar chimney represent the mean temperature at the top of the chimney.

Figure 5.6 shows that the theoretical model under-predicts the temperature in start-up conditions. This is due to the initial mass transfer due to a temperature difference, as explained in Section 5.4.1 were it is referenced. Figure 5.7 shows an over prediction, by the theoretical solar chimney model, of the temperature in start-up conditions. This is because the measurements were taken from the moment the solar chimney was heated, were the theoretical model assumes the chimney to be heated from the start.

The results show that the theory under-predicts the temperature for the evaporative cartridge and over-predicts the temperature for the solar chimney, for the steady-state conditions. Both models are less than 1 °C from the measured data. The evaporative cartridge model does over-predict the volumetric flow rate, which can be seen when comparing Figures 5.3 and 5.9. The figures

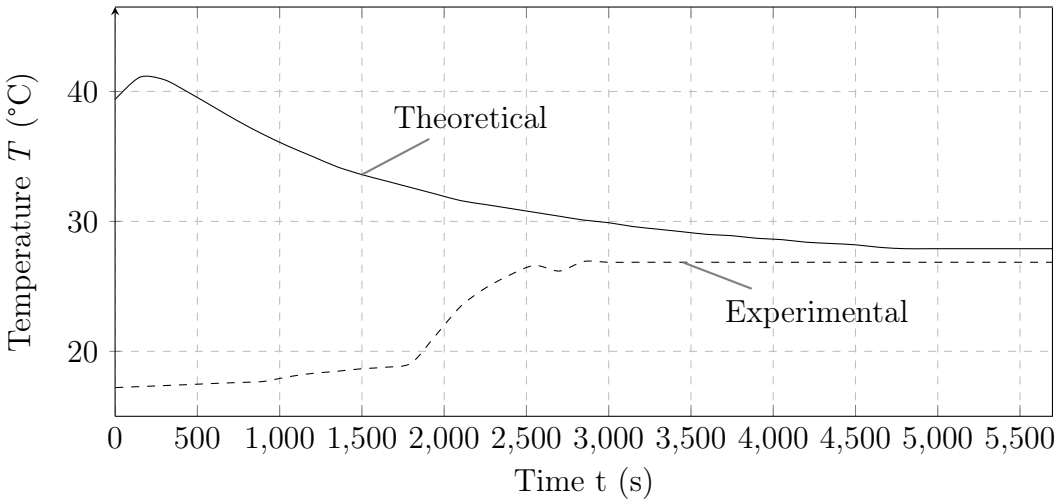

Figure 5.7: Comparison of theoretical with experimental temperature of solar chimney model [$T_{amb} = 17.1°C$, $\phi = 46.3\%$]

show that the theoretical model predicts a volumetric flow rate of $0.0425\,m^3/s$ and the measured flow rate was $0.0376\,m^3/s$. The solar chimney model under-predicts the volumetric flow rate of the measured data as shown in Figures 5.17 and B.3. The theory predicts a volumetric flow rate of $0.1401\,m^3/s$ where the measured value is $0.1759\,m^3/s$. The over prediction of the cartridge model is better understood by investigating the relative humidity distribution shown in Section 5.3, where the two dimensional effects are not taken into account by the theoretical model. The under prediction of the solar chimney model is due to each cell assuming a constant condition in a one-dimensional grid and not taking into account the two dimensional effects.

5.3 Theoretical Relative Humidity Distribution Comparison

A one-dimensional theoretical model of the evaporative cartridge section in the PDEC shaft was developed and compared with experimental results, as discussed in Section 3.1. A three-dimensional CFD model was used along with the one-dimensional model to investigate the results with more clarity and with a finer resolution. The theoretical models are compared to investigate the ability of the one-dimensional model to predict the results.

A comparison of the relative humidity distributions in the evaporative cartridge of the theoretical models are shown in Figure 5.8. The one-dimensional model shows a almost linear increase in relative humidity from the top to the bottom of the cartridge. The two-dimensional axisymmetric model shows a

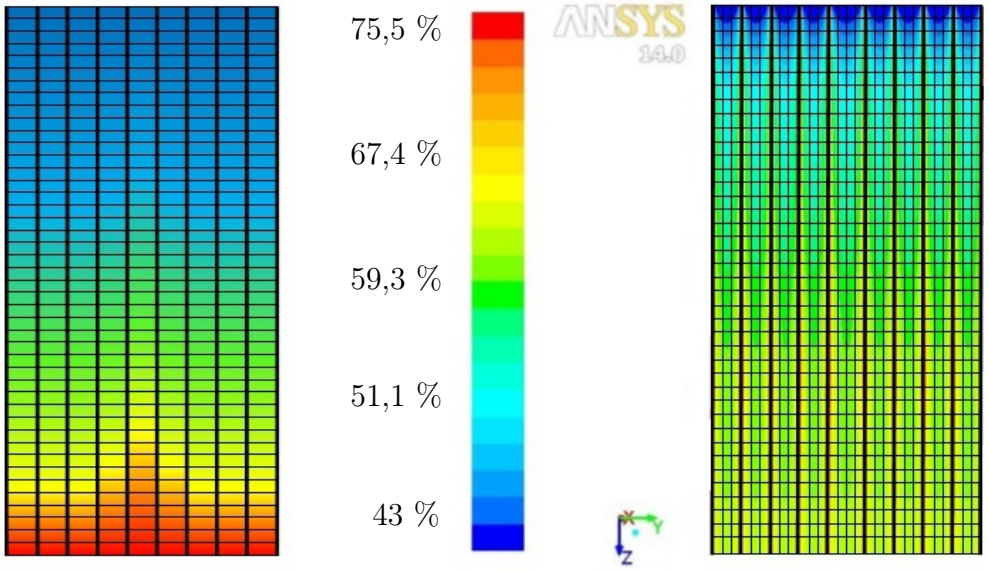

(a) One-Dimensional model (b) CFD axisymmetric model

Figure 5.8: Comparison of CFD and theoretical relative humidity distribution in evaporative cartridge section (with dark vertical lines representing the evaporative cooling pads) [$T_{amb} = 27°C$, $\phi_{initial} = 43\%$]

high relative humidity near the cartridge walls and decreasing away from the walls. The models predict a different relative humidity at different grid locations, even though the maximum relative humidity is nearly the same in both.

5.4 Inlet Configuration

Inlet configurations were tested on the PDEC testing setup as discussed in Section 3.4.2 and Section 4.1. Velocity, pressure and temperature were measured at points all along the shaft as shown in Figure 3.13. The figures showing temperature distributions provides the temperature as measured between points P1 and P4.

5.4.1 Open-Ended Inlet

The first configuration that was tested is an Open-ended configuration. The Open-ended inlet was subjected to different wind speeds with a dry and wet evaporative cartridge in the PDEC. The resulting volumetric flow rates and temperature distributions are shown in Figures 5.9 and 5.10.

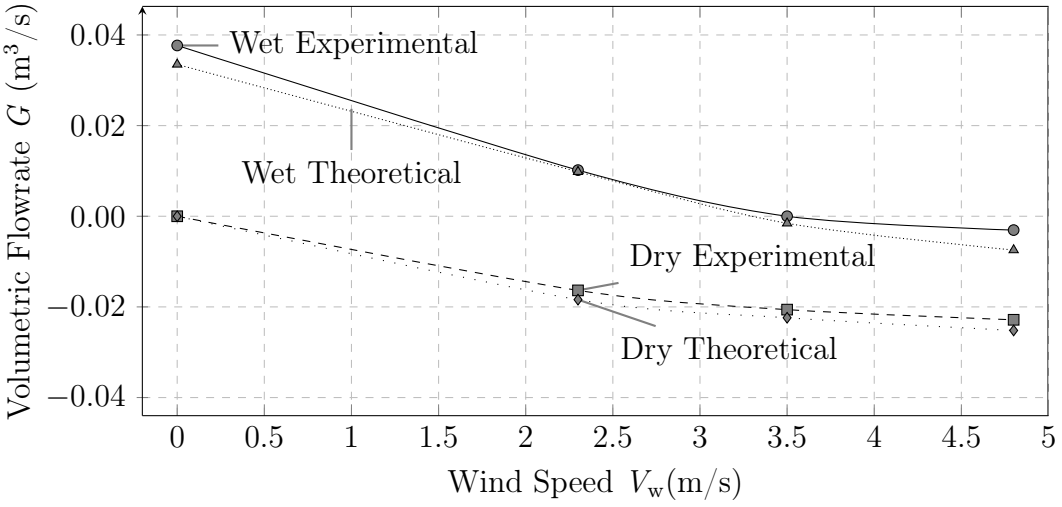

Figure 5.9: Volumetric Flowrate of PDEC as a function of wind speed for dry and wetted cartridge pads with Open-ended inlet [$T_{amb} = 26.8°C$, $\phi = 45.8\%$]

It is evident that for both the dry and the wet tests the volumetric flow rate decreased as the wind speed increased. The wind sucked the cold air out of the PDEC shaft and the inlet effectively became an outlet. Differences between the theoretical and measured data may be due to the fan not blowing the air uniformly over the inlet, as is the case with the theoretical model.

Figure 5.10 shows that the temperature at the four measured points within the PDEC shaft, with P1 at the top of the shaft above the evaporative cartridge and P4 at the bottom of the shaft. The figure shows that the temperature decreased from top to bottom when there was no wind present. When the wind increases the temperature starts increasing at the bottom of the shaft as warm air is sucked into the opening. At the same time the temperature at the top of the shaft decreased as the cooler air from the evaporative cartridge was sucked out at the top of the shaft. The temperature measured at the bottom of the evaporative cartridge (P2) for the 0 m/s test corresponds well with the one-dimensional theoretical model, as shown in Section 5.2.

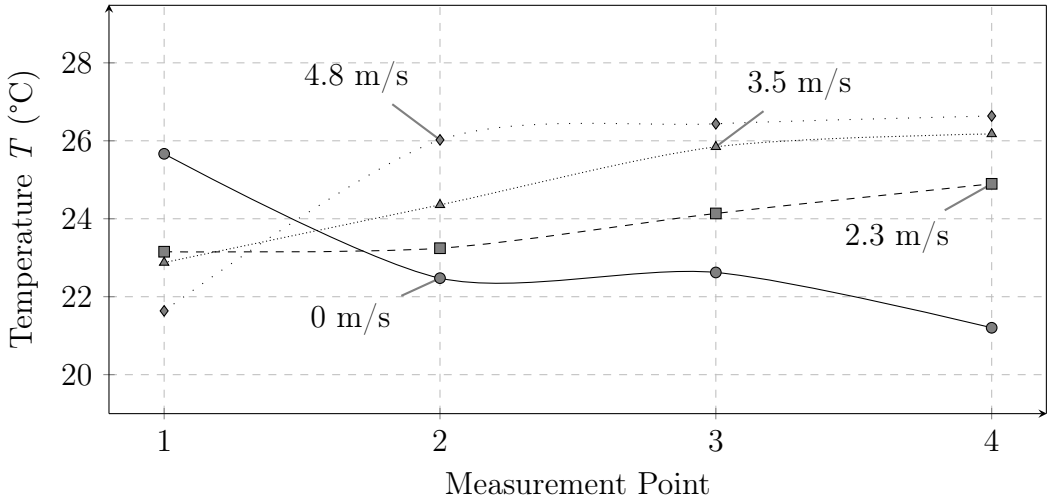

Figure 5.10: Temperature distribution along center of wetted PDEC with Open-ended inlet [T_{amb} = 26.8°C, ϕ = 45.8%]

From Section 5.2 it is evident that, although the experimental and theoretical temperature for the evaporative cartridge starts at the same value, the theory significantly under-predicts the temperature in the start-up phase. This is because the model initially over-predicts the amount of mass transferred from the liquid to the air-water vapour mixture due to the initial temperature difference between them. The initial deviation between the experimental and theoretical data can be reduced by decreasing the heat transfer coefficient between the liquid and gaseous phases. The deviation diminishes over time, because the mass transfer in the Z direction (specified in Figure 3.2) increases while the mass transfer between the evaporative pads and the air-water vapour mixture decreases as the air approaches saturation.

From Section 5.3 it is evident that, all though the models both reach the same maximum relative humidity, the one-dimensional model predicts the increase only in one flow component. This is an indicator that the CFD model will ultimately predict the flow field more accurately than the one-dimensional model.

5.4.2 Dome Inlet

The Dome configuration was designed to have an airfoil shape, which would create high and low pressure points with wind flowing over it. This pressure difference would be the driving factor of airflow in the PDEC shaft. Figure 5.11 shows the volumetric flow rate distribution with the Dome configuration on the PDEC shaft, at various wind speeds.

The Dome configuration does not create an obstruction to flow when the evaporative cartridge is wetted and no wind is present. As the wind speed

increases the volumetric flow rate decreases for a wet and dry evaporative cartridge. The Dome configuration does not create a positive, downwards flow of air for any wind speed when the PDEC shaft is dry. This suggests that the airfoil design does not work in this application.

Break-away air from flow separation at the Dome edge flows either into or over the PDEC shaft opening, depending on the flow field and wind speed. If the separated air flows over the PDEC shaft opening, inertial forces in the turbulent region will cause some of the air in the shaft to gain momentum and be sucked out at the top of the shaft. It was noticed in the experiments that the amount of air escaping at the top of the shaft varied with time. The theoretical data under-predicts the experimental data. Three sets of measurements were taken over an extended time, taking into account flow speed and direction. An average value of the results were taken in order to obtain an average volumetric flow rate as opposed to the steady-state solution predicted by the CFD model. This is the cause for the under-prediction of some of the data.

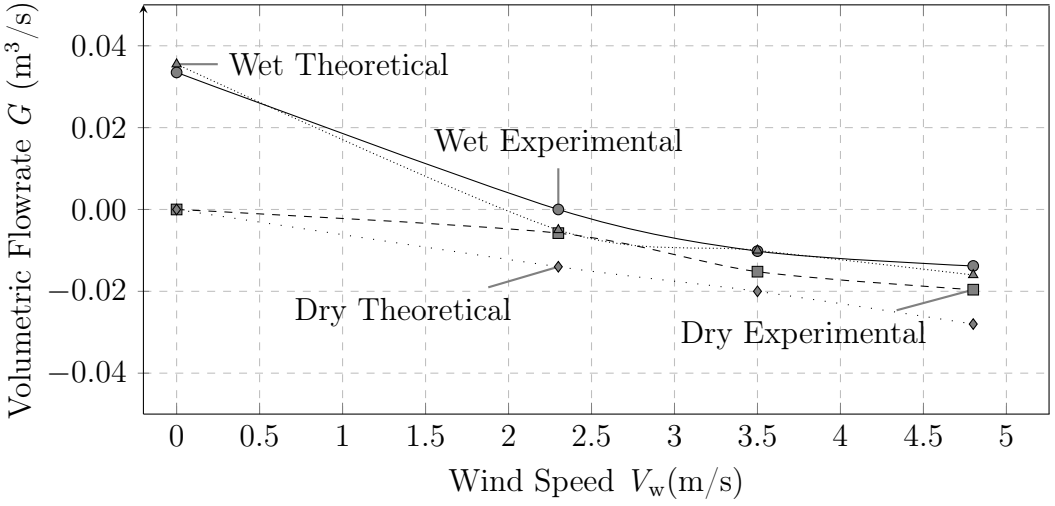

Figure 5.11: Volumetric Flowrate of PDEC as a function of wind speed for dry and wetted cartridge pads with Dome inlet [$T_{amb} = 27°C$, $\phi = 43.2\%$]

It is evident, from Figure 5.12 that, at low wind speeds, the temperature drops over the evaporative cartridge from P1 to P2. It is important to note that the temperatures do not decrease over the entire PDEC shaft, from P1 to P4, for any of the high wind speeds. The Dome inlet is therefore not capable of increasing volumetric flow rate or decreasing temperature over the PDEC shaft when wind is present.

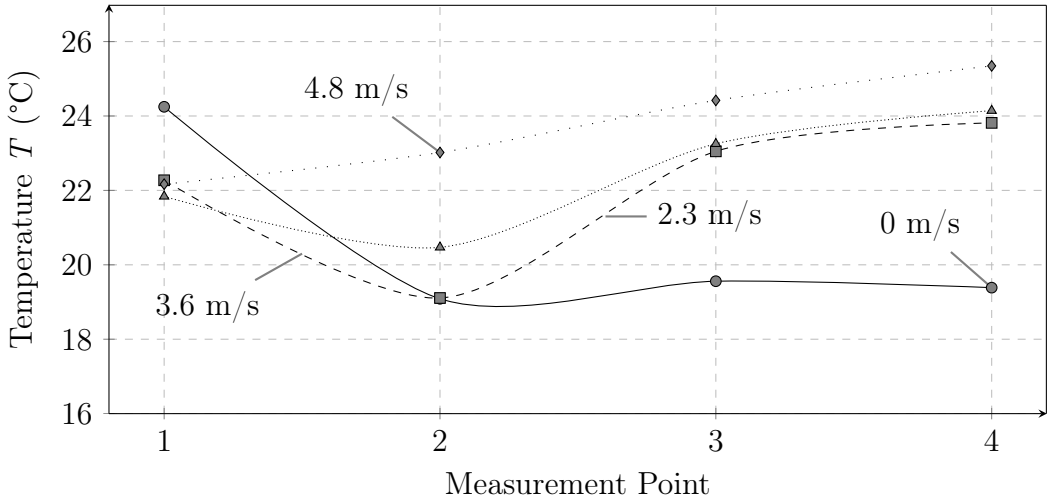

Figure 5.12: Temperature distribution along center of wetted PDEC with Dome inlet [$T_{amb} = 27°C$, $\phi = 43.2\%$]

5.4.3 DSI Inlet

It was decided to retest the DSI configuration after a study by Swiegers (2012) successfully proved the ability of the configuration to improve airflow. The configuration channels wind, with a guide vane and cone combination, and forces it into the PDEC shaft.

From Figure 5.13 it can be seen that the PDEC shaft will provide a high volume flow rate if the evaporative pads are wetted. It is evident that the theoretical wetted model under-predicts the wet experimental data. This is due to an inaccuracy in the measured velocity profile. The theoretically determined velocity profile, shown in Appendix J.2, shows the profile variation at different wind speeds. The measured air speed varied greatly between each inlet guide vane of the DSI, causing an inaccuracy in the calculation of the experimental values.

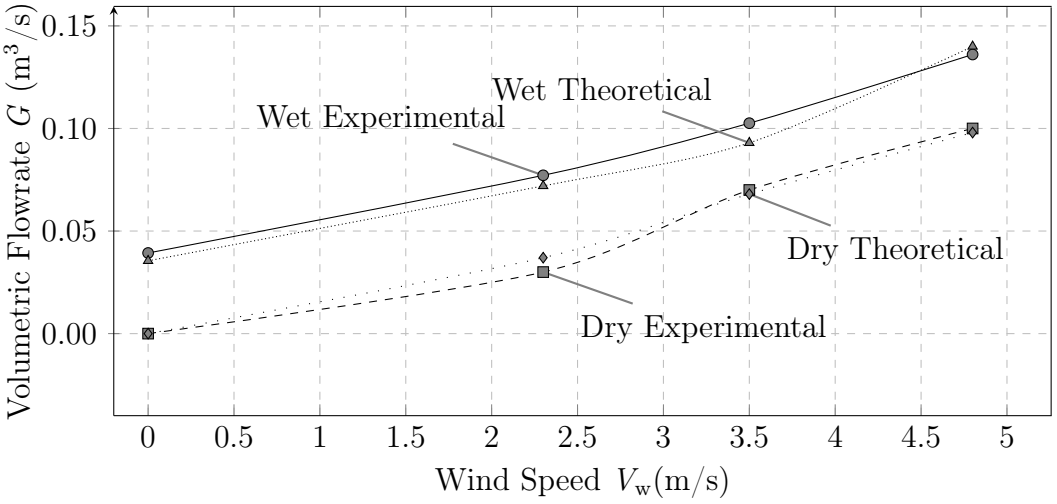

Figure 5.13: Volumetric Flowrate of PDEC as a function of wind speed for dry and wetted cartridge pads with DSI inlet [$T_{amb} = 27°C$, $\phi = 45.8\%$]

Figure 5.14 shows the temperature distribution along the centre of the PDEC for different wind speeds. The figure shows that when the DSI configuration is installed the temperature along the centre will increase as the wind speed increases. The temperature is however not linearly dependent on the wind velocity. The three-dimensional flow field is susceptible to changes in wind velocity and the velocity profile in the PDEC will vary a great deal with varying wind speeds. This variation in air speed will affect the amount of measurable heat energy at different points of measurement for different wind speeds.

The increase in temperature with increase in wind speed at P1 to P4 is apparent. Warmer outside air flows directly into the PDEC and through the evaporative pads. Evaporation occurs as the air flows through the cartridge, which cools the air before the second measurement point. The volume flow rate increases with wind speed and the air spends less time flowing though the cartridge. The air therefore has less time to cool down, which is why the temperature increases with increasing volume flow rate.

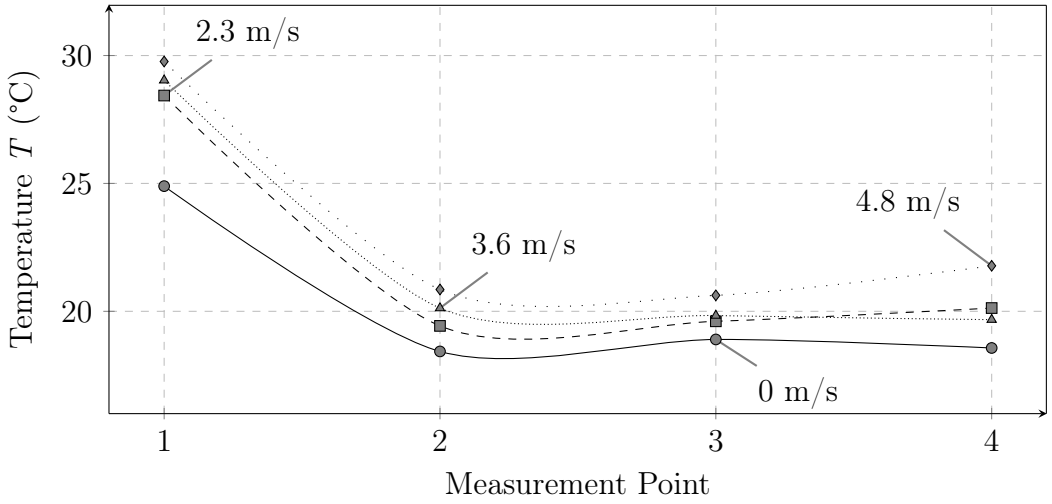

Figure 5.14: Temperature distribution along center of wetted PDEC with DSI inlet [$T_{amb} = 27°C$, $\phi = 45.8\%$]

5.4.4 TFI Inlet

The TFI inlet is a configuration that was designed to operate both with and without the presence of wind. A detailed explanation of the operating principles, as well as research on comparable previous inlet and outlet configurations, is given in Appendix E. The TFI configuration, along with the natural ventilation system, consisting of a PDEC shaft and solar chimney, was provisionally patented (Swiegers (2014)).

From Figure 5.15 it is evident that the resulting volumetric flow rate increases with an increase in wind speed for both the dry and wet evaporative cartridge tests. As the wind speed increases the dry and wet results tend towards each other, indicating that the majority contributor to the volume flow rate becomes the amount of air forced down by the TFI configuration and not by buoyancy effects.

The CFD model of the PDEC indicated that at low volumetric flow rates the parcels of air directly above the cartridge cooled down from the initial ambient temperature. In Figure 5.16 it can be seen that the addition of wind causes the temperature above the evaporative pads (P1) to increase. The temperature increase is because cold parcels of air cannot form above the evaporative pads, as the TFI channels wind into the system causing the volumetric flow rate through the PDEC to increase. The increase in volumetric flow rate means air is moving more quickly through the system and warmer outside air is drawn in from the surroundings, which increases the temperature at P1.

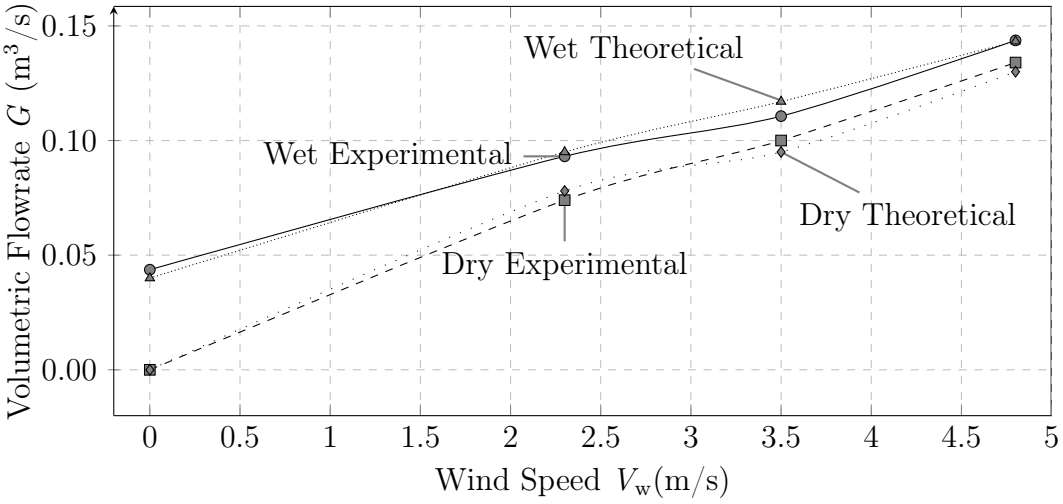

Figure 5.15: Volumetric Flowrate of PDEC as a function of wind speed for dry and wetted cartridge pads with TFI inlet [T_{amb} = 27°C, ϕ = 45.8%]

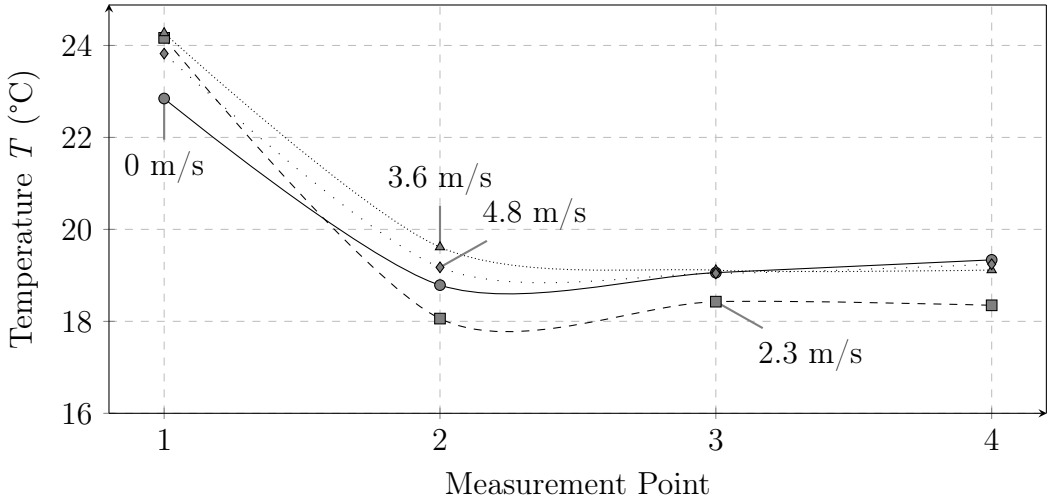

Figure 5.16: Temperature distribution along center of wetted PDEC with TFI inlet [T_{amb} = 27°C, ϕ = 45.8%]

A wind speed of 2.3 m/s shows the largest decrease in temperature over the evaporative pads (P1 to P2) compared to the zero wind speed test. The faster wind speeds shows a smaller decrease in temperature over the cartridge when compared to the zero and the 2.3 m/s test. It is noticeable that there is a smaller increase in temperature over the PDEC (P2 to P4) for the tests with

wind, when compared to the zero wind speed test. This is because air spends less time in the PDEC where heat is added by the surroundings.

5.4.5 Inlet Loss Coefficients

Inlet loss coefficients provide a measurement of the efficiency of a configuration to channel air into the PDEC shaft. Equation (3.1) in Section 3.4.2 provides a way to calculate the loss coefficient from velocity and pressure data. The average velocities measured along the width of the shaft at points along the length of the shaft was used in the equation to determine a loss coefficient for each configuration at the tested wind speeds. Measurements were taken at 0.05 m increments along the width of the shaft to determine a velocity profile and average velocity, which was further used to determine the experimental volumetric flow rates. A comparison of the theoretical and experimental velocity profile for the Open-ended inlet is shown in Appendix J.1. Table 5.1 shows the calculated loss coefficients for each inlet configuration for a wet PDEC shaft.

Table 5.1: Inlet loss coefficients for wet PDEC and various wind speeds

Wind Speed	0 m/s	2.3 m/s	3.5 m/s	4.8m/s
Open-ended	0.498	0.855	0.966	N/A
Dome	0.466	0.948	N/A	N/A
DSI	0.298	0.188	0.158	0.116
TFI	0.217	0.166	0.134	0.105

Equation (5.1) shows an example calculation of how the Open-ended inlet loss coefficient (k_{ILC}) was determined with no wind. The loss coefficient k_L due to friction on the shaft walls were calculated with the Blasius correlation (Chen (1979)).

$$
\begin{aligned}
k_{ILC} &= \frac{2((p_i - p_e) + (z_i - z_e)(\rho_i - \rho_e)g + (\frac{{V_i}^2 - {V_e}^2}{2}) + \sum_{i=1}^{n} k_L \rho_p {V_p}^2)}{\rho_i({V_i}^2)} \\
&= 2\Bigg((1) + (4.8)(1.12 - 1.216)(9.81) + (\frac{1.216(0.68^2) - 1.12(0.43^2)}{2}) \\
&\quad + 0.029(1.216)(0.68^2) + 0.193(1.12)(0.43^2) \Bigg) / (1.12(0.68^2)) \\
&= 0.498
\end{aligned} \tag{5.1}
$$

where $k_L = 4f(L)/D_h$, with $f = 64/Re$ for Re$<$2000 and $f = (0.079)(Re^{-0.25})$ for 2100$<$Re$<$100000.

Table 5.1 shows that the TFI configuration has the lowest loss coefficient for each of the tests. The DSI configuration has a slightly higher loss coefficient for each test. The Open ended and Dome inlets both have higher loss coefficients than the TFI and DSI configurations and the loss coefficients increased until they could no longer be calculated, indicated in the figure as N/A. In these tests the flow reversed and the inlet essentially functioned as an outlet. Cengel (2006) states that the loss coefficient for an Open-ended inlet is 0.5. The calculated loss coefficient from Equation (5.1) is 0.498, which corresponds well with Cengel (2006).

Inlet loss coefficients for the dry PDEC shaft is shown in Table 5.2. The inlet loss coefficients for the Open ended and Dome inlets are not shown, as the flow reversed for these tests and the loss coefficients were not calculated.

Table 5.2: Inlet loss coefficients for dry PDEC and various wind speeds

Wind Speed	0 m/s	2.3 m/s	3.5 m/s	4.8 m/s
DSI	N/A	0.395	0.269	0.215
TFI	N/A	0.218	0.160	0.134

The table shows decreasing loss coefficients with an increase in wind speed for each configuration. The TFI configuration has a lower loss coefficient for all the tests. The dry and wet PDEC tests therefore both show that the TFI configuration is the most effective in forcing air into the PDEC shaft with and without the presence of wind.

5.5 Outlet Configuration

The outlet configurations (Figure 3.14) were tested on the solar chimney, as shown in Section 3.5.2. The solar chimney was built as an independent test setup from the setup built for the PDEC shaft. Each configuration was installed on the solar chimney and subjected to different windy conditions. The tests were conducted on both a hot and a cold solar chimney in order to determine the outlets' ability to extract air if no solar resource is available. Velocity, temperature and pressure measurements were made along the solar chimney to compare results and to determine outlet loss coefficients.

5.5.1 Open-Ended Outlet

An Open-ended outlet does not provide any obstructions to air exiting the solar chimney. It does however not provide any assistance to flow when wind is present. The volumetric flow rate and the temperature distribution is shown in Figures 5.17 and 5.18.

Figure 5.17 shows that increasing wind speed decreases the volumetric flow rate though a hot solar chimney, as illustrated in Appendix K. The CFD model shows that wind blows over the outlet due to flow separation and decreases the amount of air that escapes the solar chimney. Intertial forces from the wind causes some of the air in the chimney to gain momentum and escape. The chimney walls creates an obstruction for the air that has gained radial momentum in the chimney, allthough some air still escapes. Some of the air from the wind flows into the solar chimney creating a local downdraught. These effects all contribute to the amount of air escaping the solar chimney.

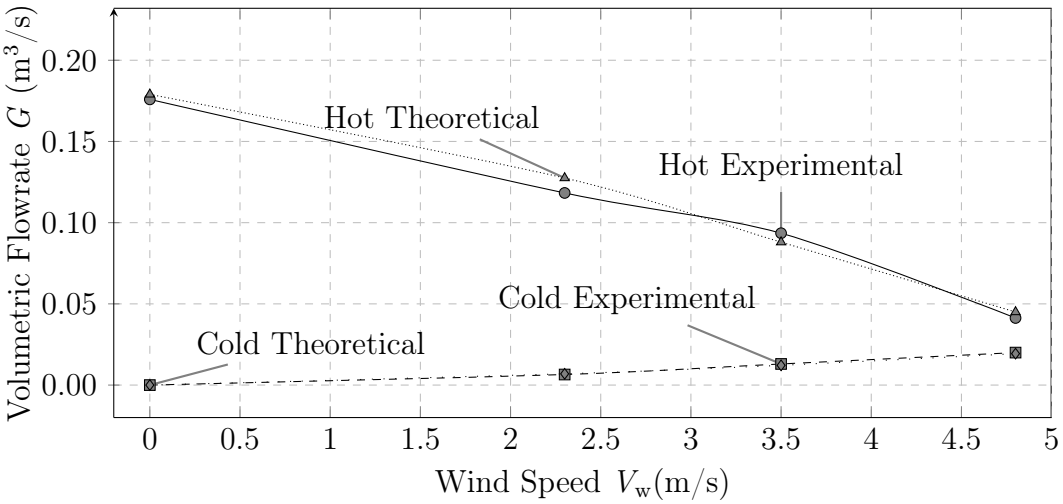

Figure 5.17: Volumetric Flowrate of hot and cold solar chimney as a function of wind speed with Open ended outlet [$T_{amb} = 17.7°C$, $\phi = 55.1\%$]

The volumetric flow rate for a cold solar chimney marginally increases with increasing wind speed. These results are different from the dry PDEC Open-ended tests, because the added pressure difference over the evaporative cartridge is not present in the solar chimney. Some of the air is able to escape and flow out of the solar chimney, contributing to a positive volume flow rate out of the chimney. The hot and cold plots converges to a volumetric flow rate of $0.03\,m^3/s$.

The results shown in Figure 5.18 do not follow a pattern with increasing wind intensity. It is evident that the wind intensity does not influence the temperature by much at the centre near the top of the solar chimney (P1). It does however influence the temperature distribution along the length of the chimney at P2 and P3. This is because air spends more time in the chimney as the volume flow rate decreases, as discussed in Appendix K. From CFD it is apparent that the increasing wind speed decreases the amount of air escaping at the top of the solar chimney.

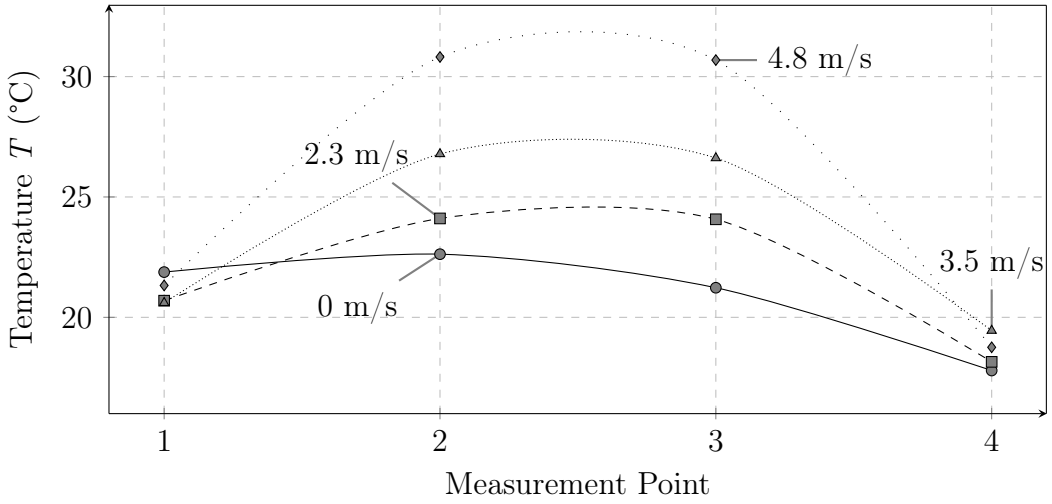

Figure 5.18: Temperature distribution along center of wetted PDEC with Open ended outlet [T_{amb} = 17.5°C, ϕ = 55.1%]

5.5.2 Dome Outlet

The Dome outlet is exactly the same configuration as the Dome inlet, but the concave dome is turned to face upwards. The intended purpose is to create an aerofoil shape, which creates a low pressure point above the opening at the top of the solar chimney. This low pressure point could help suck air out of the solar chimney and create an updraught assisting in removing stale air from the living space.

Figure 5.19 shows a decrease in volume flow rate with an increase in wind speed for a hot solar chimney. The measured and theoretical data do not coincide for the initial measurements for a hot solar chimney. This might be due to under specification of the constant temperature wall function (discussed in Appendix D) in the CFD model at the time the measurements were taken, as the temperature at the chimney wall is not constant during testing. The cold solar chimney tests show the same decrease in volume flow rate with increase in wind speed as the hot tests. The Dome outlet decreases the effect that wind has on the volumetric flow rate through the solar chimney, when compared to the Open-ended outlet.

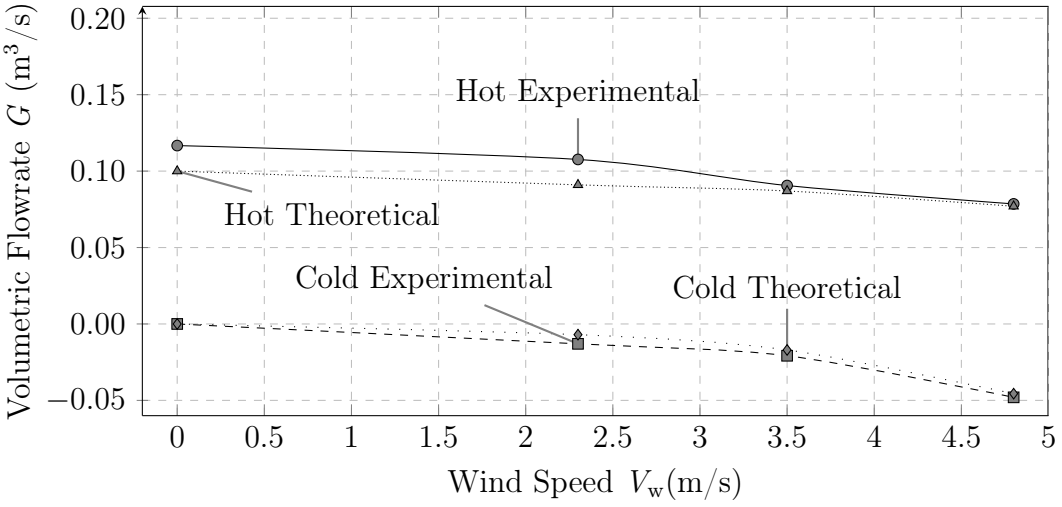

Figure 5.19: Volumetric Flowrate of hot and cold solar chimney as a function of wind speed with Dome outlet [T_{amb} = 18.1°C, ϕ = 55.5%]

Figure 5.20 shows the temperature distribution along the length of the solar chimney for the hot solar chimney tests. The test with no wind shows a low temperature distribution. This is because the hot air is exhausted easily at the top of the chimney and the air spends a small time inside the chimney where heat is added.

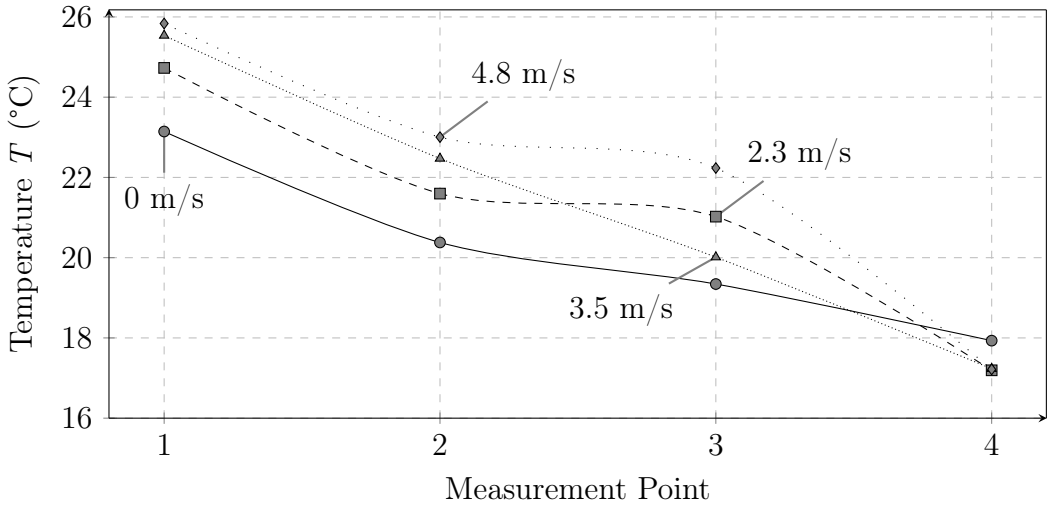

Figure 5.20: Temperature distribution along center of solar chimney with Dome outlet [T_{amb} = 17.1°C, ϕ = 55.5%]

As the wind speed increases the air struggles to escape though the outlet and spends more time inside the chimney. This extra time allows for more heat to be added to the air. The tests with wind therefore shows an increase in temperature along the length of the solar chimney.

5.5.3 *Whirlybird* Outlet

The *Whirlybird* outlet is a commercially available outlet. The *Whirlybird* configuration tested is a Windmaster Tornado 500 mm Wind Turbine. The *Whirlybird* has 32 blades acting as a turbine that sucks air out of the opening beneath it. The configuration was tested at different wind speeds on a hot and cold solar chimney. The resulting volumetric flow rate and temperature distributions are shown in Figures 5.21 and 5.22.

The *Whirlybird* acts as a resistance to flow when no wind is present. Air cannot escape as easily as it did for the Open-ended tests on a hot solar chimney. A pressure difference exists over the *Whirlybird* as wind speed increases, which assists in sucking air out of the solar chimney. This is evident in the cold solar chimney tests. The hot solar chimney tests shows an initial decrease in volumetric flow rate with an increase in wind speed. However, for the hot test with the highest wind speed the volume flow rate increased again. This is because a high pressure point is formed inside the *Whirlybird* due to the effects of wind around the configuration and the hot air rising in the chimney. This high pressure initially pushes back on the air rising in the chimney, which causes the initial decrease in volumetric flow rate for a hot tests. As the wind speed increases again a low pressure point is formed adjacent to the *Whirlybird*, on the side furthest from the incoming wind because of its dome shape. This low pressure point assists in sucking air out of the *Whirlybird* and the volumetric flow rate increases. The forces on the air due to the rotation of the *Whirlybird* further assists in air extraction.

Figure 5.22 shows an increase in temperature for P1 to P3, when compared with P4 at the bottom of the chimney. The temperature distribution initially increase for the 2.3 m/s and 3.5 m/s wind speed tests. This is due to the decreasing volumetric flow rate, as shown in Figure 5.21. The air spends more time inside the chimney where it heats up. The test conducted at a 4.8 m/s wind speed shows a similar temperature distribution as was measured for the 2.3 m/s test. This is because the experimental volumetric flow rates are similar at for the two wind speeds. The cold and the hot tests show a good correlation between the experimental and theoretical values.

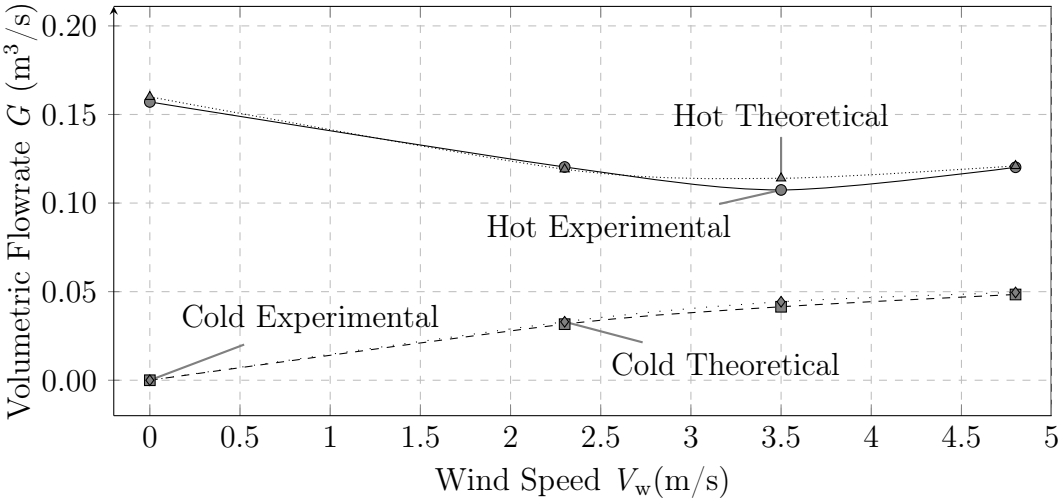

Figure 5.21: Volumetric Flowrate of hot and cold solar chimney as a function of wind speed with *Whirlybird* outlet [T_{amb} = 20.2°C, ϕ = 50.7%]

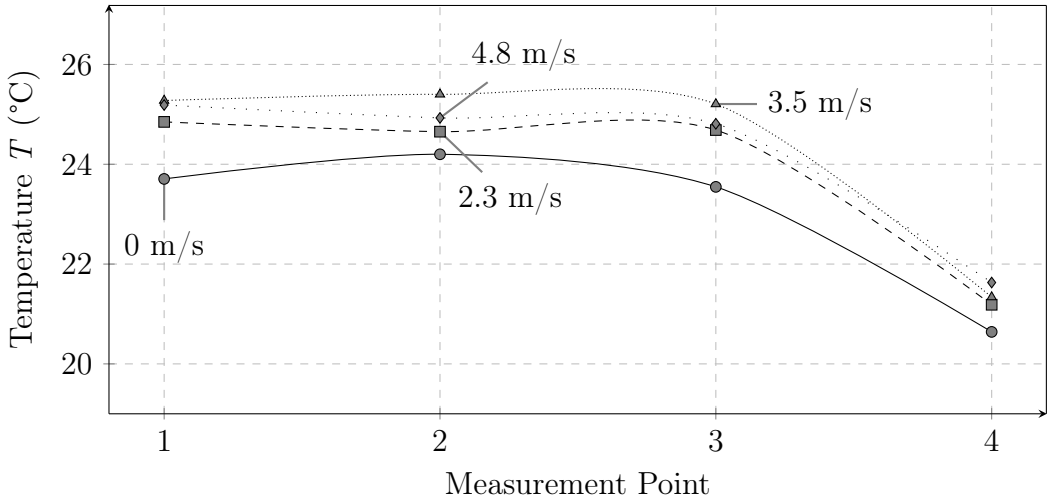

Figure 5.22: Temperature distribution along center of solar chimney with *Whirlybird* outlet [T_{amb} = 20.2°C, ϕ = 50.7%]

5.5.4 TFO Outlet

The TFO configuration is essentially the TFI configuration with the turbine and fan reversed. The turbine is reversed, along with the guide walls, to reverse the rotation of the axis connected to the fan. The fan is reversed to blow the air upwards out of the solar chimney. The volumetric flow rate, as measured at different wind speeds, is shown in Figure 5.23.

Figure 5.23 shows a decrease in volumetric flow rate with increase in wind speed, for both the hot and the cold solar chimney tests. The CFD model showed wind entering the TFO, at the turbine inlets, and flowing down into the solar chimney, as indicated in Appendix K. The effect increased with increase in wind speed. This effect might be negated by bending the turbine blades to form a helical shape, leading the wind upwards away from the solar chimney. The roof of the configuration will have to be removed for the air to flow out, which will remove protection from rain.

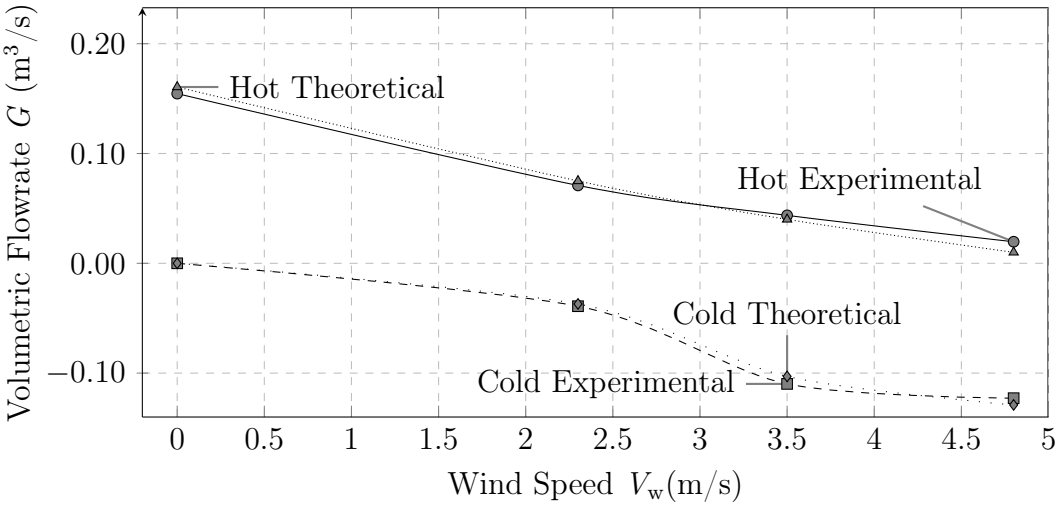

Figure 5.23: Volumetric Flowrate of hot and cold solar chimney as a function of wind speed with TFO outlet [$T_{amb} = 17.9°C$, $\phi = 48\%$]

Figure 5.24 shows the temperature distribution, along the length of the solar chimney, with increase in wind speed. The temperature distribution increased with increase in wind speed. This is because the air cannot escape at the top of the solar chimney and spends more time inside the solar chimney, where it heats up. The volume flow rate (shown in Figure 5.23) decreases as the air spends more time in the solar chimney.

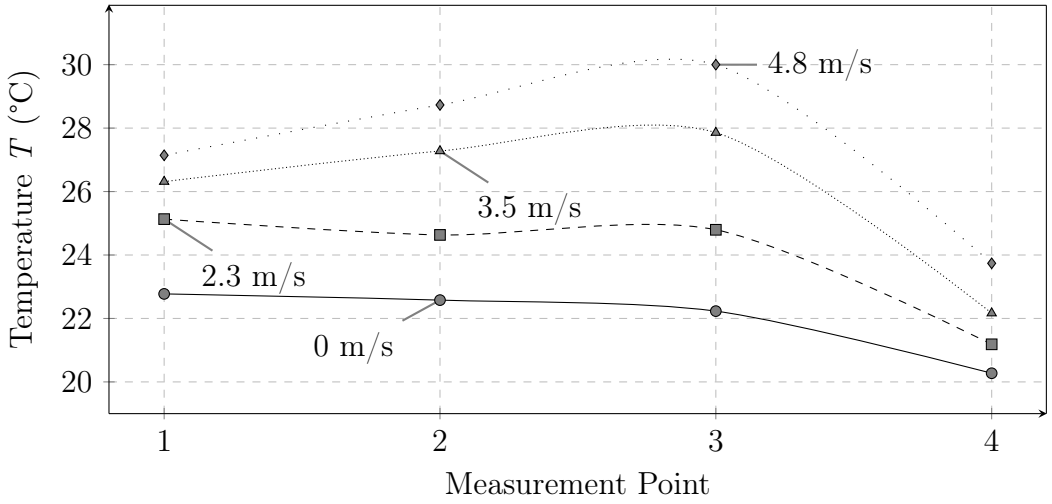

Figure 5.24: Temperature distribution along center of solar chimney with TFO outlet [T_{amb} = 17.9°C, ϕ = 48%]

5.5.5 Outlet Loss Coefficients

Outlet loss coefficients can be determined for each outlet configuration in the same way as was calculated for each inlet configuration, shown in Section 5.4.5. Equation (3.1) in Section 3.4.2 is used to calculate the loss coefficient for each configuration and for each test. Table 5.3 show the calculated loss coefficients for each configuration for the different tested wind speeds.

Table 5.3: Outlet loss coefficients for hot solar chimney and various wind speeds

Wind Speed	0 m/s	2.3 m/s	3.5 m/s	4.8 m/s
Open-ended	1.036	1.443	1.817	2.396
Dome	1.386	1.407	1.632	1.994
Whirlybird	1.112	1.424	1.564	1.393
TFO	1.065	1.817	2.664	4.534

The *Whirlybird* configuration has the lowest loss coefficient for the higher wind speeds. The Open-ended outlet has the lowest loss coefficient when no wind is present. Cengel (2006) states that the outlet loss coefficient of an Open-ended outlet, with no wind, is 1. This is close to the calculated value of 1.036. The Open-ended, Dome and TFO configuration shows an increase in loss coefficients with an increase in wind speed. The *Whirlybird* configuration shows a decrease in loss coefficient with an increase in wind speed. Figure 5.21

shows that the *Whirlybird* outlet is also the only configuration capable of effectively sucking air through the solar chimney for the cold tests. The Open-ended configuration shows a positive volumetric flow rate, but is not capable of sucking large quantities of air out of the solar chimney. The outlet loss coefficients for the cold solar chimney tests where therefore only calculated for the *Whirlybird* tests, and is shown in Table 5.4.

Table 5.4: *Whirlybird* loss coefficients for cold solar and various wind speeds

Wind Speed	0 m/s	2.3 m/s	3.5 m/s	4.8 m/s
Whirlybird	N/A	2.606	1.976	1.905

5.6 Summary of Results

A brief summary of the results obtained in Sections 5.4 and 5.5 is provided for convenience. The noteworthy results obtained from the tests on the Open-ended, Dome, DSI and TFI inlet configurations and the Open-ended, Dome, *Whirlybird* and TFO outlet configurations are given. A discussion and conclusion on the entire project is given thereafter in Section 6.

5.6.1 Summary of Inlet Results

The Open-ended inlet indicated that the volumetric flow rate through the PDEC shaft decreases with wind speed, for both a cold and dry evaporative cartridge. The direction of flow reversed, for a wet cartridge, and air flowed upwards in the PDEC shaft at a wind speed of over 3.5 m/s. The calculated inlet loss coefficient of 0.498, for no wind and a wet cartridge, corresponds well with the coefficient indicated by Cengel (2006), which is 0.5. The coldest temperature measured (for the wet PDEC, Open-ended tests) at the bottom of the evaporative cartridge was 22.50 °C. This corresponds well with 21.7 °C predicted by the one-dimensional model, as shown in Section 5.2. The dry tests indicated an updraught in the PDEC shaft for all wind speeds.

The same decrease in volumetric flow rate was noted with the Dome inlet, although the decrease was not as significant. The flow reversed at a lower wind speed (around 2 m/s) than it did for the Open-ended tests. Even though the Dome inlet protects against rain, it does not provide a significant advantage over the Open-ended inlet if a configuration is required that functions well in still and windy conditions.

The DSI configuration showed a significant increase in volumetric flow rate with increase in wind speed. The inlet loss coefficient decreased with an increase in wind speed for all the tests. A maximum flow rate of 0.136 m^3/s was measured at a wind speed of 4.8 m/s for a wet evaporative cartridge.

A increase in volumetric flow rate with an increase in wind speed was also noted for the TFI configuration. The volumetric flow rate at all wind speeds was greater for the wet and dry test when compared to the DSI configuration. The coldest temperature measured at the bottom of the PDEC shaft was 18.4 °C. This temperature was measured at a wind speed of 2.3 m/s.

5.6.2 Summary of Outlet Results

The tests conducted on a Open-ended outlet, with a hot solar chimney, showed a decrease in volumetric flow rate as the wind speed increased. The cold solar chimney tests indicated a positive flow rate of air upwards in the solar chimney for all wind speeds. The flow of air in the solar chimney therefore never reversed. The lowest outlet loss coefficient of 1.036 was calculated when no wind was present. Cengel (2006) predicts this value to be 1, which is close to the calculated value.

Tests conducted on the Dome outlet indicated a slight decrease in volumetric flow rate with an increase in wind speed. Air flowed downwards in the solar chimney for the cold tests. The Dome outlet is not capable of increasing the volumetric flow rate through the solar chimney, even though it decreases the effects that wind has on the chimney when compared to the Open-ended outlet tests.

The *Whirlybird* outlet proved to be the most effective in maximising the air flow rate through a solar chimney for the tested wind speeds. The tests on a hot solar chimney with no wind showed a decrease in volume flow rate from 0.176 m^3/s to 0.157 m^3/s, for an Open-ended and *Whirlybird* configuration respectively. The *Whirlybird* therefore ads a resistance to the outflow of the solar chimney. A pressure difference exists over the *Whirlybird* when wind is present. This pressure difference assists in sucking air out of the chimney. The maximum calculated outlet loss coefficient for the *Whirlybird* was 1.564 for a wind speed of 3.5 m/s.

The volumetric flow rate through the solar chimney with the TFO configuration decreased with an increase in wind speed. The configuration was not successful in sucking air out of the solar chimney and the volumetric flow rate decreased from 0.154 m^3/s to 0.019 m^3/s, as the wind speed increased from 0 m/s to 4.8 m/s. The flow of air reversed for the cold solar chimney tests and the downdraught of air increased with increasing wind speed. This downdraught was created by the turbine blades capturing air from the incoming wind and forcing it down the chimney. This effect could be negated by bending the blades to force air to escape at the top of the configuration.

6 Discussion and Conclusion

Natural ventilation systems use natural driving forces, such as wind pressure and buoyancy, to move air through a living space. Air flowing in a natural ventilation system enters through an inlet and exits through an outlet. This study investigated the inlet and outlet shape design of a natural ventilation system, while keeping in mind the natural driving forces of the system. In order to test different configurations, a natural ventilation testing setup was built. The natural ventilation system consisted of a full scale Passive Downdraught Evaporative Cooling (PDEC) and solar chimney, as shown in Section 4.

6.1 Inlet Configurations

Swiegers (2012) tested four inlet configurations namely the Open-ended, Extruding end, Cone and DSI (Dobson Swiegers Inlet) configurations. The inlets were tested in a wind tunnel simulating conditions in a PDEC shaft. Thereafter they were tested on a laboratory scale SCAPDEC (Solar Chimney Augmented Passive Downdraught Evaporative Cooling) system. The DSI configuration performed best under varying wind speeds and draught intensities.

For the current study it was decided to test four inlets namely the Open-ended, Dome, DSI and TFI (Turbine Fan Inlet) configurations. The inlet configurations were introduced in Section 3.4. Details on the construction of each inlet configuration were discussed in Section 4.1. A large scale PDEC shaft was constructed in a thermally controlled space, as discussed in Section 3.4.2.

The PDEC shaft incorporated an evaporative cartridge situated within the shaft wall. A one-dimensional, finite difference theoretical model of the evaporative cartridge section was developed, shown in Section 3.1, and used to determine optimal cartridge dimensions before construction began. Appendix B.1 provides the convergence testing of the one-dimensional evaporative cartridge model. It was decided to build a cartridge with five concentric evaporative pads with an outer diameter of 0.5 m and a length of 1 m. A comparison of the one-dimensional model predictions and the experimentally measured values are given in Appendices 5.2 and 5.3. The one-dimensional model was unsuccessful in capturing the start-up conditions. Different materials were tested (Section 4.1) to determine their wettability and it was decided to build the

cartridge from 100 % cotton (b grade), white bull denim. The PDEC shaft was built with a length of 4.8 m to allow space for the configurations to be installed on top of the shaft and air to escape freely at the bottom of the shaft.

The inlet configurations were installed on the PDEC shaft and tested under different wind intensities. The tests were conducted on a shaft with a dry or wet evaporative cartridge. Temperature, pressure and velocity measurements were taken with each test. Each test was simulated in FLUENT® to provide theoretical three-dimensional results to compare with measured results. A discussion of the CFD models are given in Section 3.3. FLUENT® was used as a tool to determine theoretical results and to inspect flow patterns that could not be visualised with smoke tests. It was not used as a tool for optimisation before tests began and pictures with colourful graphics were kept to a minimum, as numerical data is of more value when comparing with the experimental results. The measured and theoretical volumetric flow rate for each test were compared in Section 5.4. The CFD results proved to be extremely accurate in predicting measured data. An outlet loss coefficient was calculated for all the wet PDEC tests.

Section 5.6.1 shows a summary of the results obtained from the tests on the inlet configurations. The Open-ended inlet was the most effective in forcing air through the PDEC shaft when no wind was present, with a volumetric flow rate of 0.038 m^3/s. The calculated inlet loss coefficient of 0.498 was close to the value calculated by Cengel (2006), which is 0.5. The Dome inlet was not effective in forcing air through the wet PDEC and the flow of air reversed when the wind speed rose above 3.5 m/s, after which the air flowed up the shaft and out through the inlet. The DSI (Dobson Swiegers Inlet) configuration was effective in forcing air through the PDEC shaft at all tested wind speeds. A maximum of 0.136 m^3/s was measured with the DSI configuration installed on a PDEC with a wet evaporative cartridge, at a wind speed of 4.8 m/s.

The TFI (Turbine Fan Inlet) configuration was the most effective in forcing air through the PDEC shaft at the tested wind speeds. A maximum volumetric flow rate of 0.144 m^3/s was measured at a wind speed of 4.8 m/s. The volumetric flow rate at all wind speeds was greater for the dry test when compared to the DSI configuration. The coldest temperature measured at the bottom of the PDEC shaft was 18.4 °C at a wind speed of 2.3 m/s. The natural ventilation system proposed in this study, consisting of the PDEC and solar chimney along with the TFI configuration, was provisionally patented (Swiegers (2014)).

6.2 Outlet Configurations

Swiegers (2012) tested four outlet configurations namely the Open-ended, Cone, *Whirlybird* and DSO (Dobson Swiegers Outlet) configurations. The configurations were tested on the same wind tunnel that was constructed for

the inlet testing, but with the direction of the forced draught reversed to simulate conditions in a solar chimney. The outlet configurations were then tested on a laboratory scale SCAPDEC system. The DSO and whirlybird configurations were deemed to be equally capable of removing air from the solar chimney. A set of four inlet configurations were chosen for this study, namely the Open-ended, Dome, *Whirlybird* and TFO (Turbine Fan Outlet) configurations. The outlet configurations were introduced in Section 3.5. The configurations were tested on a large scale solar chimney (shown in Section 3.5.2) built in a thermally controlled space.

The solar chimney was built with the same dimensions as the PDEC shaft, with a height of 4.8 m and a diameter of 0.5 m. A one-dimensional, finite difference model was constructed to determine the ability of the model to predict the performance of a large-scale solar chimney. Appendix B.2 shows convergence testing of the one-dimensional solar chimney model. Section 5.2 shows a comparison of measured data with the theoretically predicted outlet temperature of the solar chimney by the one-dimensional model. The model was unsuccessful in capturing the start-up conditions.

The inlet configurations were installed on the solar chimney and tested at various wind speeds. Temperature, pressure and velocity measurements were taken at the same locations as for the tests on the PDEC shaft. Results were compared with theoretical results from CFD and the one-dimensional model were applicable. The measured and theoretical CFD volumetric flow rate for each test was compared in Section 5.5. The CFD results proved to be accurate in predicting measured results. An outlet loss coefficient was determined for each configuration.

Section 5.6.2 shows a summary of the results obtained from the tests on the outlet configurations. The Open-ended outlet showed a decrease in volumetric flow rate with an increase in wind speed for the hot tests. A loss coefficient of 1.036 was calculated when no wind was present, which is close to the value of 1 given by Cengel (2006). The Dome outlet showed a slight decrease in volumetric flow rate in the solar chimney with an increase in wind speed. Even though the Dome outlet decreases the effect that wind has on the outlet when compared to the Open-ended outlet, it is not capable of increasing airflow through the chimney with increase in wind speed. The *Whirlybird* outlet was the most effective in sucking air out of the solar chimney for the tested wind speeds. The *Whirlybird* does add a resistance to the outflow, which was evident when a volumetric flow rate of 0.157 m^3/s was measured at 0 m/s, compared to 0.176 m^3/s for the Open-ended outlet. A pressure difference was measured over the *Whirlybird* when wind was present. This pressure difference assisted in sucking air out of the chimney. The maximum calculated outlet loss coefficient for the *Whirlybird* was 1.564 for a wind speed of 3.5 m/s. The TFO configuration was not capable of increasing airflow and the volumetric flow rate decreased from 0.154 m^3/s to 0.019 m^3/s, as the wind speed increased from 0 m/s to 4.8 m/s.

6.3 Concluding Remarks

The effectiveness of an inlet configuration is determined by its ability to force air into the PDEC shaft. For each test the configurations' ability to induce flow was determined. The ability can be ranked with a five point performance system between poor, fair, good, very good and excellent. Table 6.1 provides a summary of each inlet configurations' ability to increase volumetric flow rate in the PDEC shaft. The table should serve as a guide when choosing a suitable inlet configuration for a natural ventilation system. From the table it is evident that the TFI configuration performs best in both still and windy conditions.

Table 6.1: Ability of inlet configurations to increase volumetric flow rate in a dry and wet PDEC

Inlet		0 m/s	2.3 m/s	3.5 m/s	4.8 m/s
Dry:					
Open-ended		-	Poor	Poor	Poor
Dome	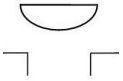	-	Poor	Poor	Poor
DSI	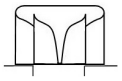	-	Good	Very Good	Very Good
TFI	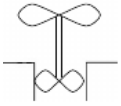	-	Excellent	Excellent	Excellent
Wet:					
Open-ended		Excellent	Fair	Poor	Poor
Dome	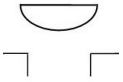	Good	Poor	Poor	Poor
DSI	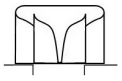	Good	Good	Very Good	Very Good
TFI	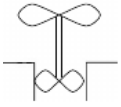	Good	Excellent	Excellent	Excellent

The effectiveness of an outlet configuration is determined by its ability to suck air out of the solar chimney. Table 6.2 provides a summary of each outlet configurations' ability to induce flow in the solar chimney. The same five point performance ranking system is used as was used in Table 6.1. The table indicates that the *Whirlybird* configuration performs the best for both still and windy conditions.

Table 6.2: Ability of outlet configurations to increase volumetric flow rate in a cold and hot solar chimney

Outlet		0 m/s	2.3 m/s	3.5 m/s	4.8 m/s
Cold:					
Open-ended		-	Poor	Fair	Fair
Dome	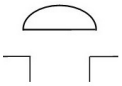	-	Poor	Poor	Poor
Whirlybird	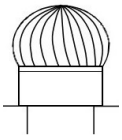	-	Good	Good	Very Good
TFO	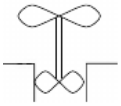	-	Poor	Poor	Poor
Hot:					
Open-ended		Excellent	Good	Good	Fair
Dome	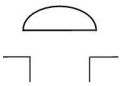	Poor	Poor	Poor	Poor
Whirlybird	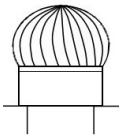	Very Good	Very Good	Good	Very Good
TFO	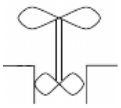	Very Good	Fair	Fair	Poor

7 Recommendations

In this study inlet and outlet configurations were tested on a PDEC (Passive Downdraught Evaporative Cooling) shaft and solar chimney. Large-scale independent PDEC and solar chimney models were built, with a height of 4.8 m and diameter 0.5 m, on which the inlet and outlet shapes were tested. The conditions of air flowing into the shaft and chimney were controlled, as the test setups were built in a thermally controlled room. It is proposed to couple the PDEC and solar chimney to form a full-scale SCAPDEC (Solar Chimney Augmented Passive Downdraught Evaporative Cooling) system. The PDEC and solar chimney should be built on either side of a "living space" that has a realistic heat load and dimension. The living space could incorporate a single room or multiple stories of a building complex. The SCAPDEC system can be built outside and tested throughout the year to determine the ability of the system to ventilate the living space in a South African climate.

It is further suggested that the possibility of a two-dimensional empirical model be investigated. The one-dimensional model proved too inaccurate in the start-up phase. A two-dimensional model could prove to be more sensitive to changes in start-up and boundary conditions. A two-dimensional empirical model could also be a useful tool if a CFD software package, or a computer capable of running it, is not available.

Appendix A

Environmental Impact / Amelioration Implications

This report focuses on optimising inlet and outlet shapes for a full scale PDEC and solar chimney or a combined SCAPDEC system. Full scale natural ventilation systems have been implemented in building structures and could significantly reduce environmental emissions (Martinez (2000)). These systems generally only implement a PDEC shaft without an assisted solar chimney.

A.1 Health Implications

Recent findings have shown that indoor air is often more polluted than outdoor air and is often a greater health hazard than the corresponding outdoor setting (Elzaidabi (2008)). Sundell (2002) states that people spend up to 90 % of their life indoors. The indoor environment is therefore the most important environment in relation to human health.

Axley (2001) states that natural ventilation systems admitting outdoor air without filtration in urban environments, where outdoor particulate levels are excessive, result in low indoor air quality. Mechanical ventilation systems offer air filtration and are often built with central automation and extensive ducting. If these systems are not properly maintained it results in poor indoor air quality and health risks. Axley (2001) further states that robustness is the ability of a system to perform up to the expectations when assumptions and conditions underlying its design are violated. Natural ventilation systems rank high in terms of robustness. This means that a natural ventilation system can provide a more healthy, comfortable and productive environment if the design is robust and not complex like most mechanical ventilation systems. Axley (2001) further states the value of the pleasure of fresh outdoor air, when available, and the ability to personally control ventilation, should not be underestimated. Emmerich *et al.* (2001) conducted a study were a user controlled natural ventilation systems was implemented in a building and concluded that

occupants were more than capable of obtaining thermal comfort as well as air quality.

PDEC shafts draw in outside air, humidifies it, and a downdraught causes the humidified air to flow into the building structure. Humidifying air does however increase the risk of fungi and bacterial exposure, as declared by WHO (2009). Fungi and bacteria levels in the air can be decreased to an acceptable level if the evaporative cartridge is regularly washed or replaced if necessary. The feed-water to the cartridge should be regularly cleaned or filtered.

A SCAPDEC system draws in outside air and exhausts it without the need for recirculation. The spread of diseases through viruses, bacteria or fungi decreases as exhausted air is lost to the environment if inlets and outlets are not placed close together. Mechanical ventilation systems often recirculate air as this decreases the amount of air that has to be tempered to the required thermal condition.

A.2 Environmental Impact

A SCAPDEC does not use a compressor or refrigerants to cool the air to the desired temperature. Water is the only cooling media used and the system can be deemed environmentally friendly when compared to mechanical ventilation systems. Mechanical ventilation systems require energy input to operate pumps and fans. This energy is likely electricity generated in coal-based power plants. Natural ventilation systems therefore generally have a lower carbon footprint than mechanical ventilation systems. Photovoltaic augmentation of natural ventilation may rapidly become feasible with falling prices and minimal or no storage requirement. This could decrease the cost of electrical fan-assisted inlet and outlet configurations which could increase the overall efficiency of the ventilation system.

Martinez (2000) theorises that an average person requires $58.2\,\mathrm{W/m^2}$ of cooling power per day to achieve thermal comfort. In section 5.1 it was theorised that the evaporative cartridge built for this study has a cooling power of 280 W. If the occupant latent loads, lighting, computer loads, solar loads and fresh air requirement is ignored, a PDEC shaft is required every $4.81\,\mathrm{m^2}$. This is an unrealistic requirement in a building structure. The model also predicts a maximum cooling capacity of 600 W, although this design was not chosen due to reasons discussed in the section. This cooling capacity would require a PDEC shaft vent every $10.3\,\mathrm{m^2}$. This approach will lead to a high relative humidity of indoor air which may lead to occupants not feeling thermally comfortable. A larger number of PDEC shafts will require more building material and water consumption, which will increase the initial and maintenance costs as well as the carbon footprint. It should be noted that the current study was done with specific input parameters and the cartridge will perform best in a dry

and hot climate. A compromise between cooling capability and environmental impact should be found when designing a naturally ventilated building.

In South Africa, ESKOM is currently the main supplier of electricity throughout the country and has varying tariffs depending on the time of day. The energy saved in a building with a natural ventilation system that does not rely on electrical inputs and can therefore be calculated based on the tariffs. It is clear that such a building requires a lot less power than a building with a conventional air conditioning system and has a lower overall carbon-footprint.

Appendix B

Convergence Testing for the One-Dimensional Models

Convergence testing is required in order to use the results of the one-dimensional models. Results are sensitive to changes in number of control volumes and the size of the time step. This Appendix investigates the grid sensitivity of the one-dimensional theoretical evaporative cartridge and solar chimney models.

B.1 Evaporative Cartridge Model

The theoretical model was written in FORTRAN and ran in FTN95 from Silverfrost Compiler with the Plato Interactive Program Development Environment (IDE). For each set of input conditions convergence testing was done on the output variables. For each condition the temperature, volumetric flow rate and relative humidity of the control volume at the bottom of the evaporative cartidge or solar chimney was checked for convergence. Results were only deemed to have converged if the changes in results were different by less than 3 % with each iteration. Figures B.1 and B.2 shows convergence testing of the temperature output of a specific input condition.

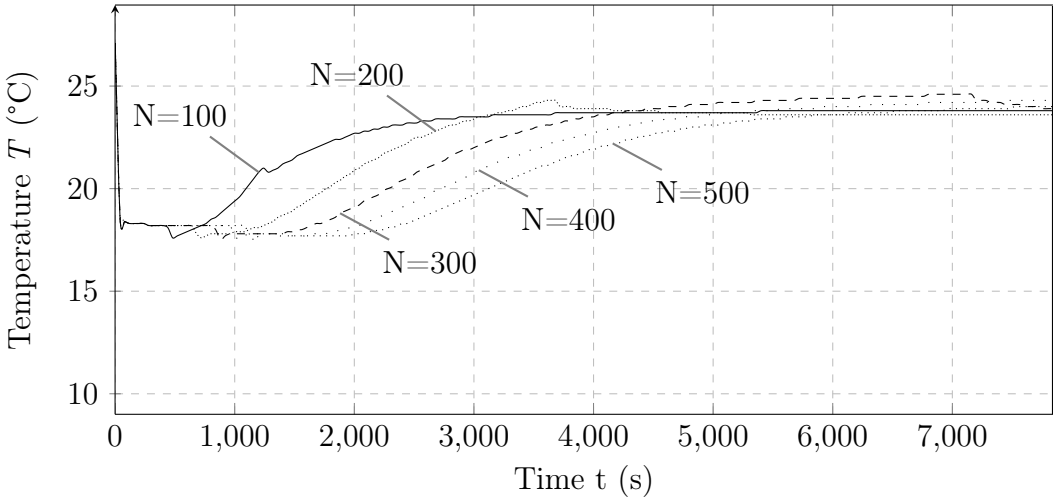

Figure B.1: Convergence of temperature with change in number of lengthwise control volumes (N) of theoretical evaporative cartridge model [L = 0.9 m, 3 concentric pads, T_{amb} = 27.5°C, ϕ_i = 43%]

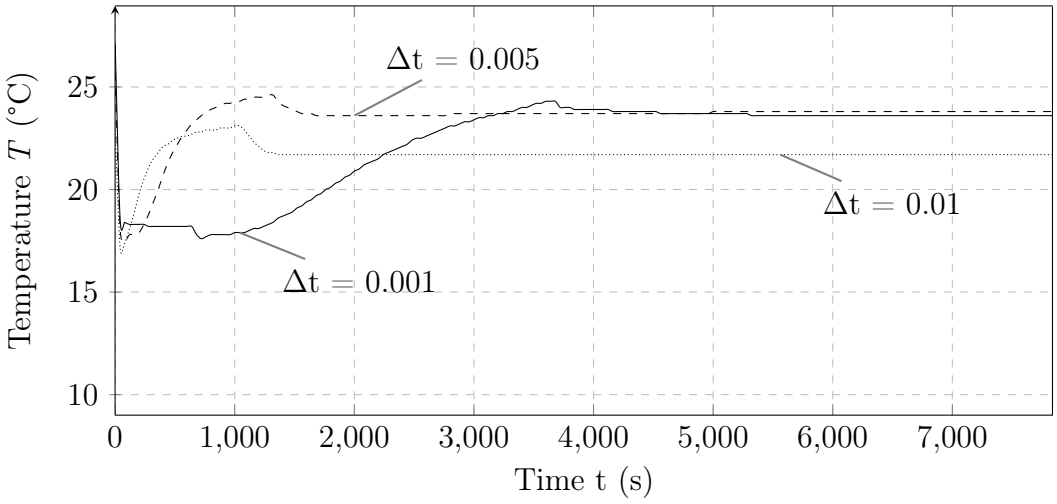

Figure B.2: Convergence of temperature with change in time step (Δt) of theoretical evaporative cartridge model [L = 0.9 m, 3 concentric pads, N = 300, T_{amb} = 27.5°C, ϕ_i = 43%]

B.2 Solar Chimney Model

The solar chimney model followed the same prerequisites for convergence as discussed in section B.1. Figures B.3 and B.4 shows convergence testing of

the volumetric flow rate output of a specific input condition (indicated in the figure caption with square brackets).

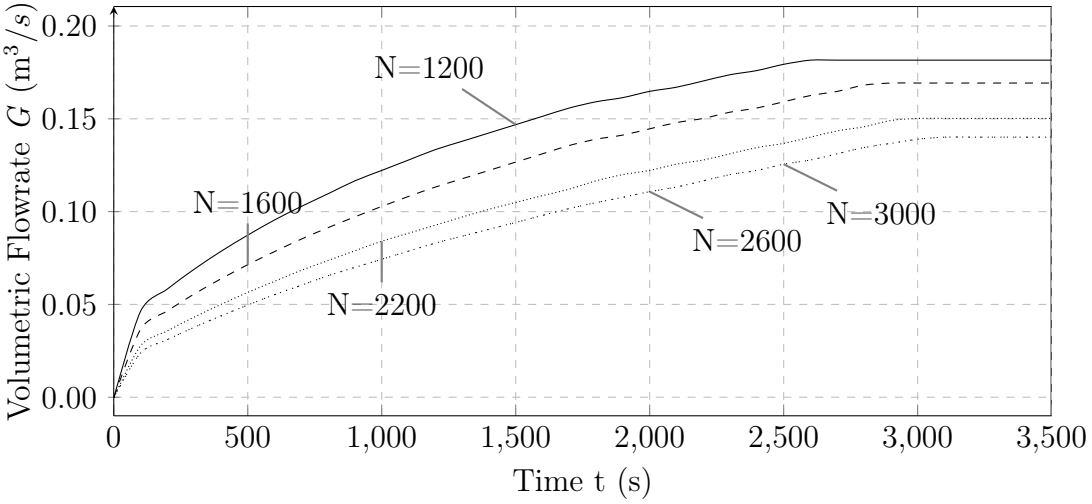

Figure B.3: Convergence of volumetric flow rate with change in number of lengthwise control volumes (N) of theoretical solar chimney model [T_{amb} = 17.1°C, $\phi_i = 56\%$]

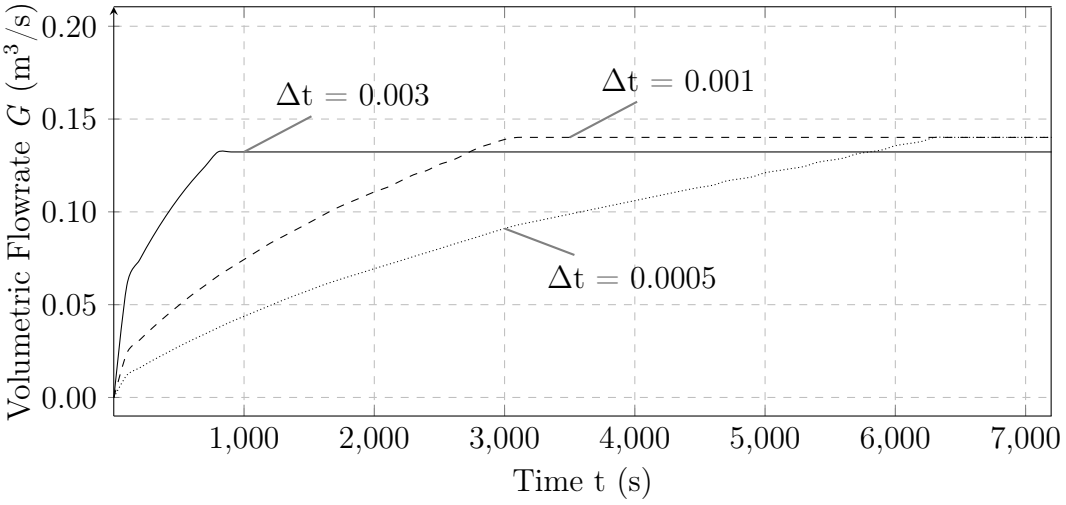

Figure B.4: Convergence of volumetric flow rate with change in time step (Δt) of theoretical solar chimney model [N = 2600, T_{amb} = 17.1°C, $\phi_i = 56\%$]

Appendix C

CFD Mesh Stability and Grid Independence

In order to obtain reasonable and reliable results, a well converged and grid independent simulation is required. Convergence criteria must assure that results do not change with each iteration. In order to achieve convergence for each CFD model scalar change is monitored. The temperature and velocity at the model inlets and outlets were monitored. The solution was considered converged if these values had a domain imbalance of 1% or less. Residuals of the continuity, momentum and energy equation was monitored and a solution was only considered converged if the residuals fell below a value of 10^{-3} and the residuals of the energy equation below 10^{-6}.

One of the procedures undertaken to globally refine the mesh was to adapt the mesh according to calculated temperature gradients. A refinement threshold was set to refine the grid at points were temperature gradients exceeded the threshold. Another procedure was to define a "number of divisions" boundary condition at each edge of the mesh and to scale all divisions with a constant factor between simulations, until grid independence was reached. A flow chart showing the procedure undertaken for mesh refinement for each inlet and outlet mesh is shown in Figure C.1.

The mesh for the Open-ended inlet and outlet configuration were first refined to an acceptable level before any of the remaining configurations were modelled. The remaining configurations were modelled in the same domain as the Open-ended configurations. Once the configuration was modelled into the domain, the mesh was refined around the configuration. The mesh in the rest of the domain was left mainly unaltered. Figures C.2 and C.3 show the refinement process for the Open-ended inlet configuration with average temperature, beneath the evaporative cartridge, and volume flow rate through the PDEC shaft.

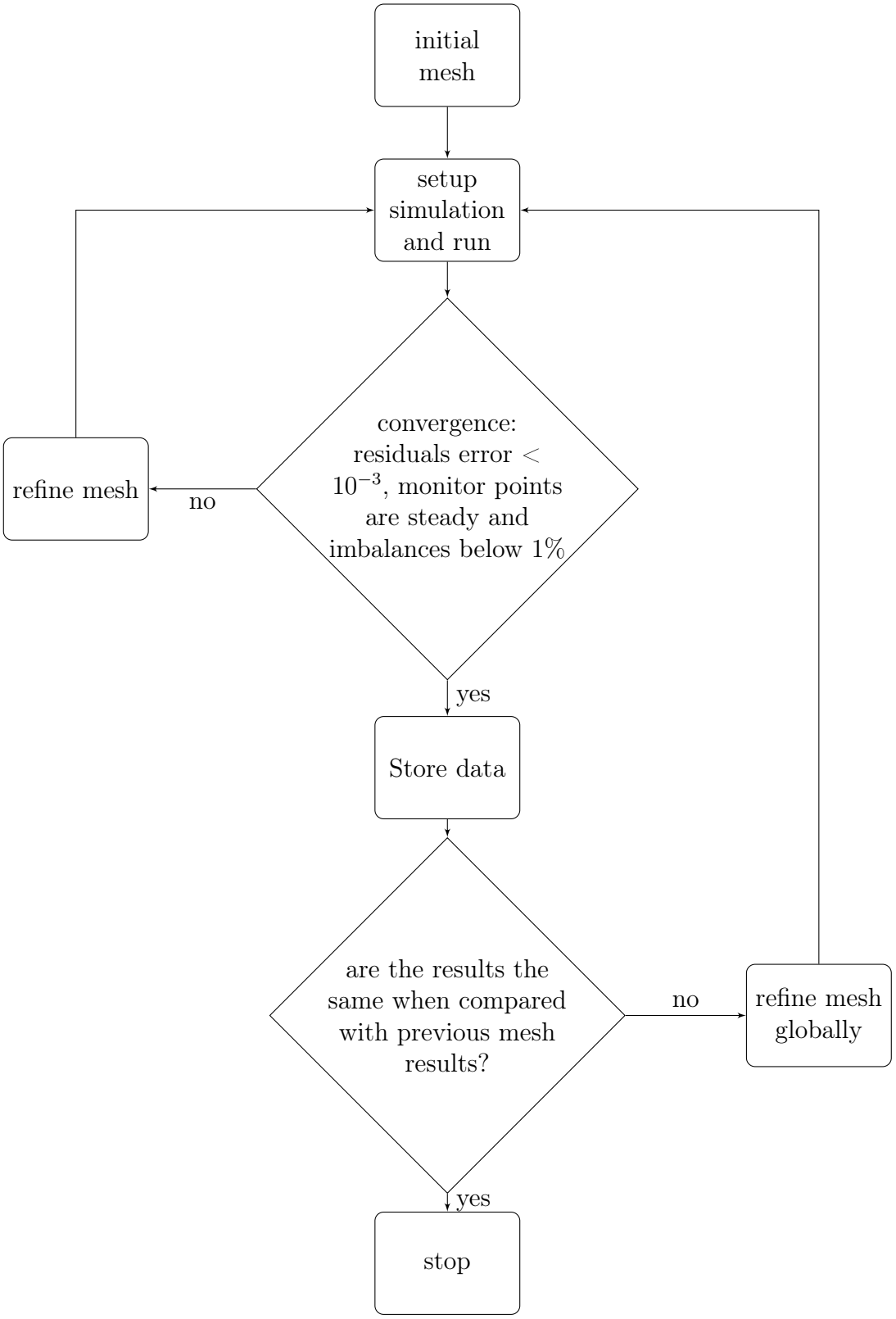

Figure C.1: Flow chart showing the procedure for mesh refinement

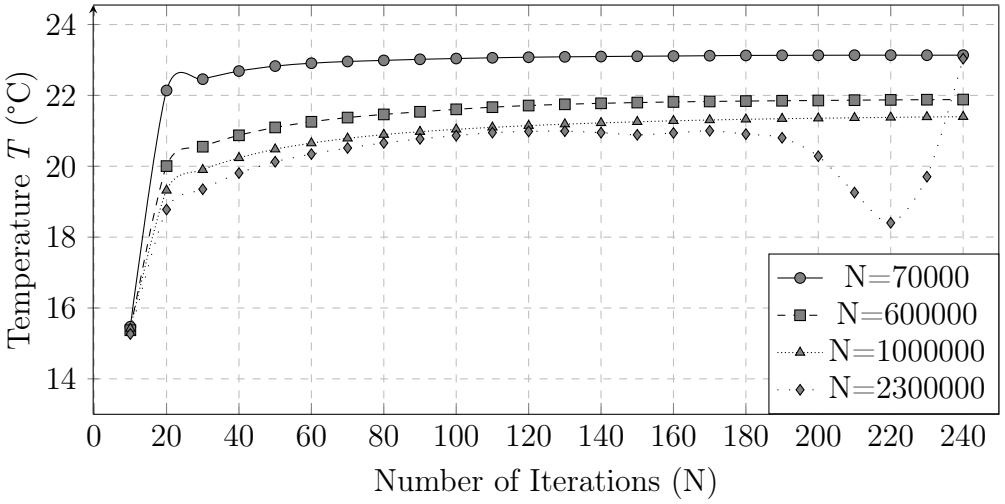

Figure C.2: CFD model convergence check with the average temperature beneath the evaporative cartridge [T_{amb} = 26.8°C, ϕ_i = 43%]

Figure C.2 shows that a finer mesh provides a more accurate answer when compared with experimental data. The finest mesh causes an instability in the result. This problem may be corrected by changing the under-relaxation factors in the setup or by checking which equation failed first. The mesh can then be adapted according to which equation provided the instability in the mesher.

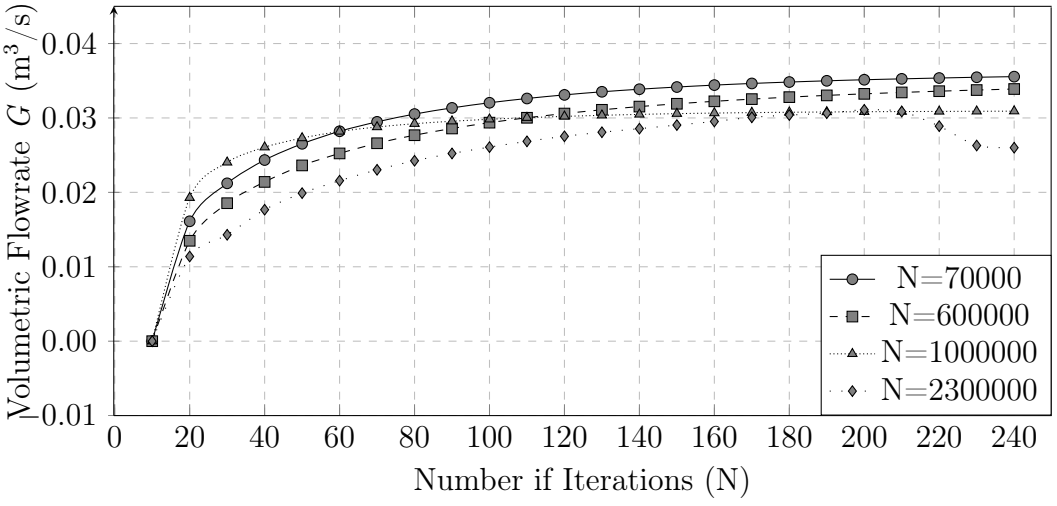

Figure C.3: CFD model convergence check with volume flow rate through the PDEC shaft [T_{amb} = 26.8°C, ϕ_i = 43%]

FLUENT® allows for this adaptation to be made in the setup program itself, without the need to restart the mesher program. The mesh can be updated according to where the steepest gradient of a specific variable occurs. The mesh will therefore be updated where the variable change is the most significant.

Figure C.3 shows that there is not a significant change in the calculated volume flow rate with a increase in the number of elements. The finer meshes do indicate a lower volume flow rate when compared to the coarser meshes. Table C.1 shows the final mesh properties chosen for each inlet configuration.

Table C.1: Mesh properties of inlet models

Configuration	Number of Elements
Open ended	1016549
Dome	993283
DSI	1154352
TFI	1628522

The procedures for mesh stability and grid independence were followed for the theoretical models of the outlet configurations as well. The results for the Open-ended outlet are shown in Figures C.4 and C.5.

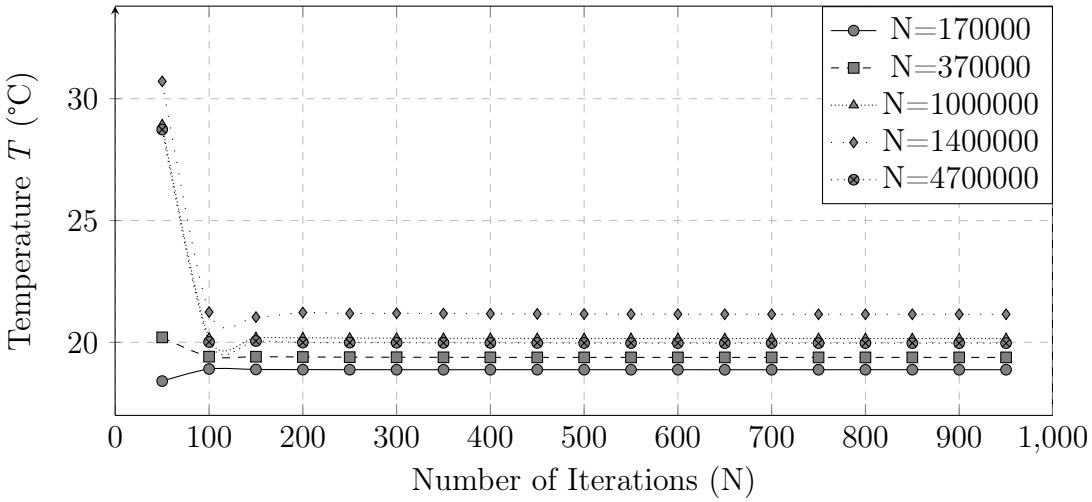

Figure C.4: CFD model convergence check with the average temperature at the top of the solar chimney [T_{amb} = 26.8°C, ϕ_i = 43%]

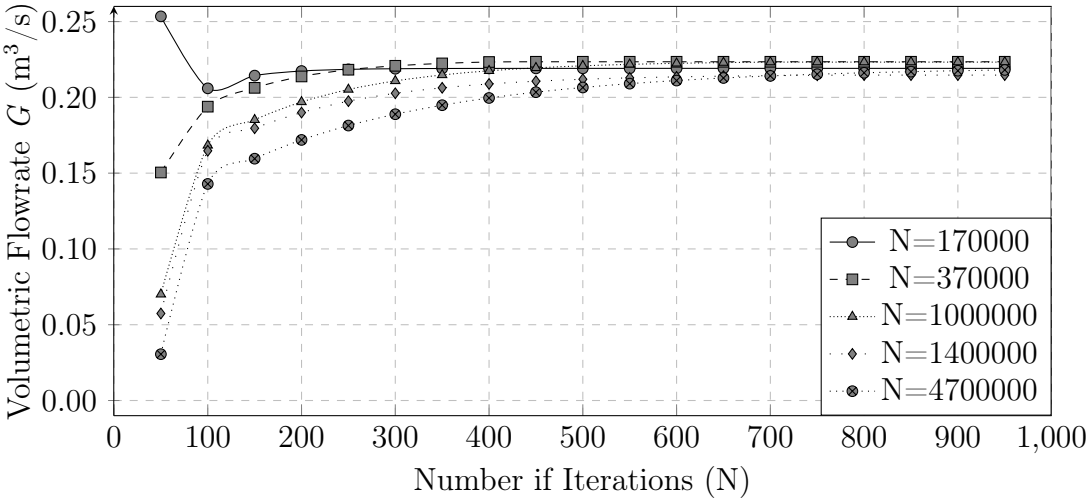

Figure C.5: CFD model convergence check with volume flow rate through the solar chimney [T_{amb} = 26.8°C, $\phi_i = 43\%$]

The results show that the finer mesh does converge to an answer and that the coarser meshes both under-predict and over-predict the outlet temperature and overpredict the volume flow rate through the solar chimney. The final mesh properties of the theoretical model for each outlet configuration are shown in Table C.2.

Table C.2: Mesh properties of outlet models

Configuration	Number of Elements
Open ended	1132415
Dome	1053223
Whirlybird	1296976
TFI	1593770

Appendix D

Solar Chimney Temperature Distribution

The temperature distribution on the walls of the solar chimney is used as a boundary condition for the one-dimensional solar chimney model. Figure D.1 shows the temperature distribution as measured at four points along the solar chimney. A second-order polynomial equation is shown in the figure and was used in the one-dimensional and CFD theoretical models.

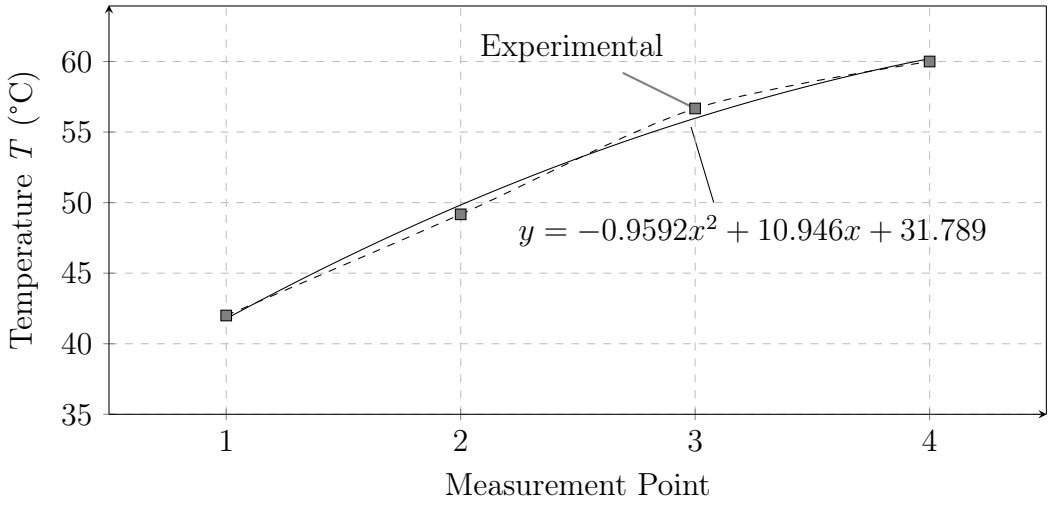

Figure D.1: Temperature distribution along the wall of solar chimney [T_{amb} = 17.1°C, ϕ = 56.1%]

Appendix E
TFI Configuration

The TFI configuration was designed with natural ventilation systems in mind. Natural ventilation systems generally have slower moving air when compared with conventional HVAC systems, because it uses buoyancy effects to move air through a living space. In order to increase the volume flow rate through the system the TFI configuration was designed to function when wind is blowing through it and not cause an obstruction in the absence of wind. This Appendix investigates previous inlet configurations that was designed for similar operating conditions. Specifications for the design of the TFI configuration are provided.

E.1 Previous Configurations

It is necessary to investigate previous configurations that are used to either extract or force air into a space. One way to investigate previous configurations is to research patents. This section investigates different patents of similar inlet or outlet configurations. The patent code has been included in all the patent figure titles.

The patent in Figure E.1 is a roof ventilator that extracts hot air. The invention consists of a turbine hood that uses wind energy to turn a fan or vane assembly. The turbine is turned by either hot air rising from underneath or winds. It differs from a conventional *Whirlybird* in that it incorporates an axial fan to assist in increasing air flow. The fan is said to come with an optional motor powered by electricity from PV panels on windless days. This patent is not suggested to be used in combination with a natural ventilation system. It does not mention a savonius turbine or channels to force wind onto a specific point on the turbine. It is only mentioned as an outlet configuration.

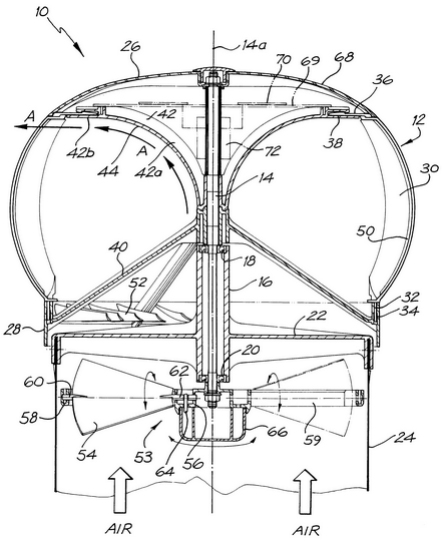

Figure E.1: Relative humidity distribution (WO 2000068619 A1)

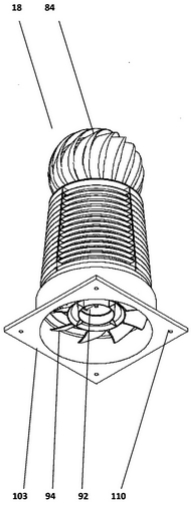

Figure E.2: Passive heat recovery and ventilation system (US 20110201264 A1)

The patent, shown in Figure E.2, is a passive heat recovery system. The configuration is placed on top of the system which acts as an inlet and an outlet for stale air. Fresh air flows in through the configurations louvers which are downwards facing to create a pressure difference for incoming air. It then flows through an axial fan, connected to a turbine at the top of the configuration,

and then flows through a heat exchanger. Here stale air flows in the opposite direction as incoming fresh air without coming in direct contact with each other. Heat transfer takes place between them in order for the fresh air to approach the temperature of the outflowing air. The fresh air then flows into the living space. The stale air flows through the centre of the axial fan, through a pipe, into the outlet turbine where it is evacuated.

This system is designed to provide fresh air to a living space in an energy efficient manner. It does not have separate inflow and outflow chimneys. Stale air will therefore be difficult to evacuate without the use of a mechanical fan. This system does not employ evaporative cooling to achieve thermal tempering. It does not employ a savonius turbine with wind guide channels. The invention is an inlet and outlet configuration in one and cannot be placed on the inlet and outlet of a natural ventilation system.

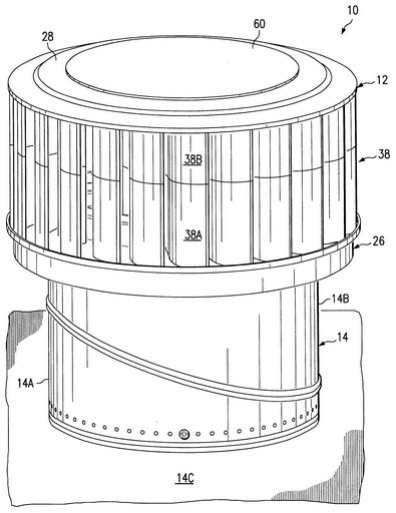

Figure E.3: Windjet turbine (US 6582291 B2)

The invention in Figure E.3, like a whirlybird, is mostly used to evacuate hot and stale air from attic air space. The invention comprises of a turbine which is made by molding or extruding techniques. Stale attic air increases the load placed in the air conditioning system and this invention helps to remove this hot air by extracting it through the roof structure. The air is extracted by the hot air that rises through it or by wind energy rotating the turbine throwing the air out like a centrifugal fan. This patent does not include the use of an axial fan and is not used in cooperation with a natural ventilation system.

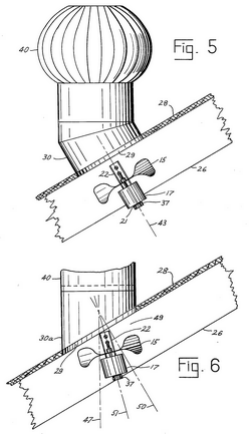

Figure E.4: Fans for use with turbine ventilators, and methods and apparatus for supporting the same (US 3952638 A)

The patent in Figure E.4 incorporates a turbine and a fan, where the fan is spaced a distance away from the turbine instead of within the base of the roof jack or base of the ventilator itself. The fan is said to be located away from the ventilator to increase efficiency and for noise reduction purposes. The invention is for any purpose where a ventilator could be used. It does not mention a savonius turbine that channels wind.

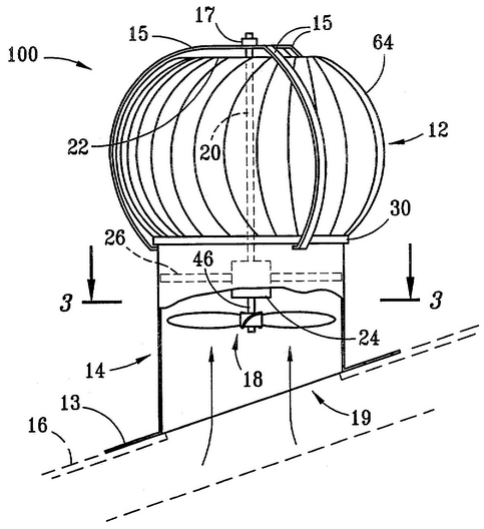

Figure E.5: Turbine ventilator (US 20030190883 A1)

Figure E.5 shows an ventilator comprising of a turbine coupled to a fan so that rotation of the turbine results in rotation of the fan at a rotational speed greater than that of the turbine. The patent suggests that a gearbox is used to rotate the fan faster than the turbine and not at the same speed. The Turbine Ventilator does not channel wind to a savonius turbine. This patent describes an outlet configuration that removes air from a ventilated space and is not mentioned as an inlet configuration. A Ventilation system that uses evaporative cooling is not mentioned.

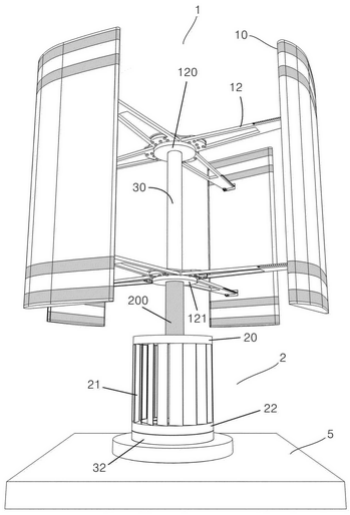

Figure E.6: Vertical wind turbine generator with ventilator (US 20130049373 A1)

The vertical wind turbine generator with ventilator, shown in Figure E.6, is an assembly consisting of three components: a vertical wind turbine assembly, a ventilator, and a generator. This assembly can be installed on roof openings, or any other opening that can benefit from power generation and ventilation. The power generation unit is connected to the ventilator, which in turn is connected with the wind turbine. The ventilator unit and a power generator is driven simultaneously when the turbines rotate. The generator produce electricity and the ventilator exhausts the air. The vertical wind generator with ventilator is a device to generate electricity and to serve as an outlet configuration for a ventilation system. It is not for a evaporative cooling system and not mentioned as being able to serve as an inlet.

E.2 Construction of the TFI Configuration

The TFI configuration was designed to force air into a natural ventilation system with and without the presence of wind. It was therefore designed to increase volume flow rate through the PDEC shaft and not to be an obstruction when the flow is only bouyancy driven. The TFI configuration, along with the PDEC and solar chimney ventilation system, is provisionally patented (Swiegers (2014)).

The design incorporates a savonius rotor that extrudes above the PDEC shaft. The rotor has four half-cylinder shaped blades connected to a central shaft. Each blade has an inlet guide-vane which forces air onto the convex part of the blade. The rotor acts as a turbine that drives a fan, which is situated inside the PDEC shaft. The fan has four blades and connected to the savonius rotor by a shaft. Figure E.7 shows an exploded view of the TFI configuration.

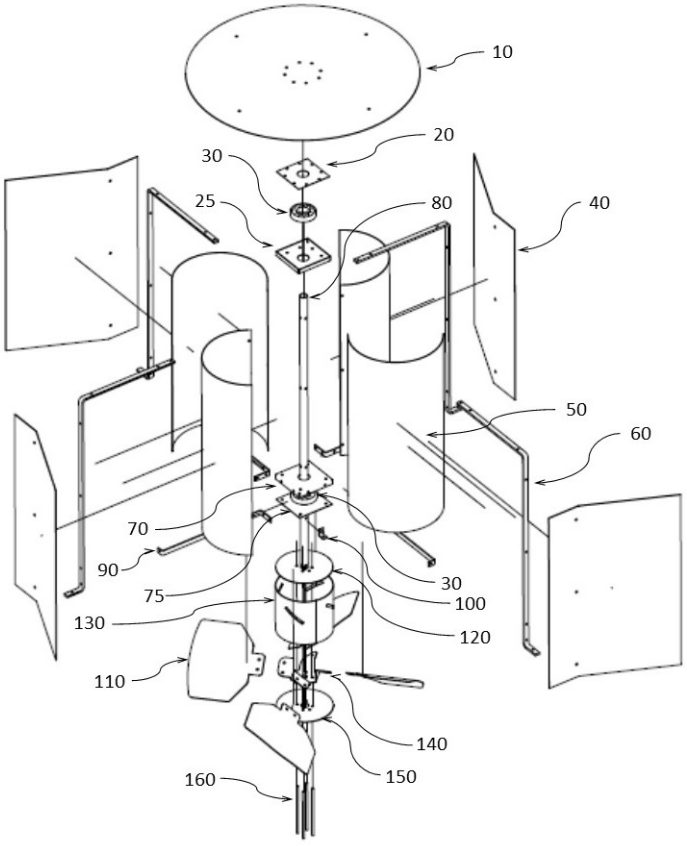

Figure E.7: Exploded view of TFI configuration (Swiegers (2014)).

The fan, fun hub, bearing casings, roof plate, savonius blades and inlet guide vanes were rolled and bent from 0.9 mm aluminium sheet metal. The shaft is 16 mm diameter aluminium tubing with 1.5 mm wall thickness. A 12x16x40mm ball bearing is used at the top and bottom of the savonius rotor to centre the shaft. The structure that grounds the inlet guide vanes and bearing casings is made from 2 mm aluminium sheet metal. Steel brackets of 1 mm thickness is added to strengthen the corners of the structure plates.

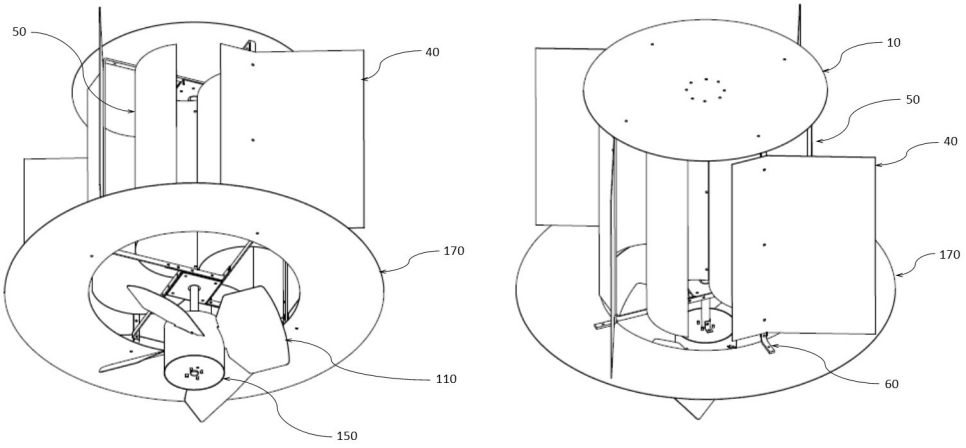

Figure E.8: Top and bottom isometric view of the TFI configuration (Swiegers (2014)).

Appendix F

Solar Chimney Hairdryer Settings for Temperature Distribution

The hair dryers that heat the solar chimney walls have two settings for speed and two settings for heat intensity. The tests with different combinations of settings were completed before any tests with outlet configurations. The aim of these tests were to find a combination of a speed and heat setting that heats the chimney as much as possible, without altering the structural integrity of the chimney and that is capable of keeping the chimney walls at a constant temperature. Temperatures at the four measurement points (as was shown in Figure 3.15) from the top to the bottom of the chimney are shown in Figure F.1.

The settings have either a setting of "1", representing a low setting, and "2", representing a high setting. For each setting combination there is an increase in temperature between P4 and P3. The updraught created by the solar chimney draws in colder air from the room, which is what is measured at P4. From P3 to P1 there is a decrease in temperature. In this section of the solar chimney some heat is lost to the environment through the outer wall, most notably with the "Heat 1, Speed 1" setting. To best interpret this data, it is necessary to investigate the measured volumetric flow rate for each test, which is shown in Table F.1.

The table shows an increase in volumetric flow rate with an increase in the heat and speed settings of the hairdryer. Each hairdryer has to operate for the length of each test to maintain the solar chimney at a constant temperature. To decrease the risk of overworking the hairdryer heating elements or melting the solar chimney walls, it was decided to test each outlet configuration with a "Heat 1, Speed 2" setting.

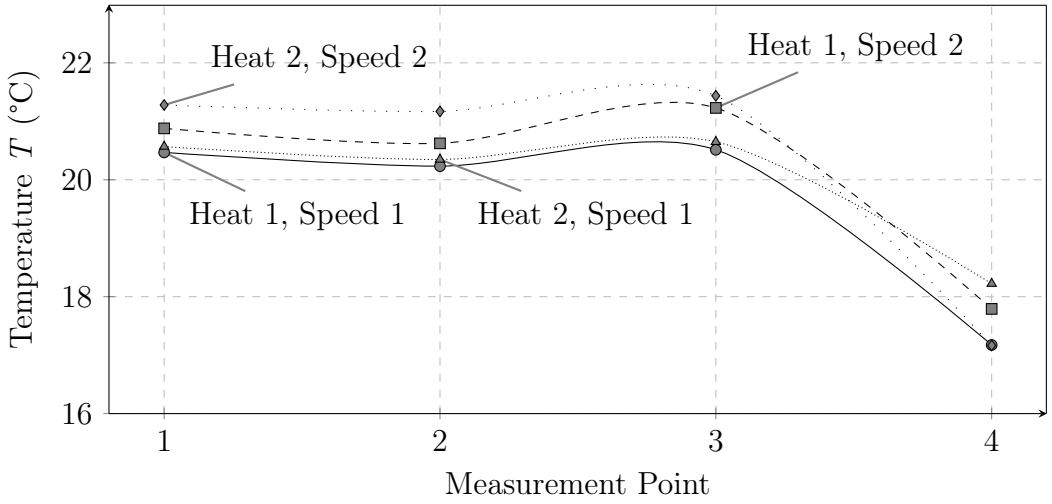

Figure F.1: Temperature distribution along centre of solar chimney for different hairdryer settings [$T_{amb} = 17.1°C$, $\phi = 56.1\%$]

Table F.1: Volumetric flow rate for different settings

Test	Volumetric flow rate [m^3/s]
Heat 2, speed 2	0.1898
Heat 1, speed 2	0.1759
Heat 2, speed 1	0.1523
Heat 1, speed 1	0.1468

Appendix G
Thermocouple Calibration

Thermocouples are calibrated by measurement either at a series of fixed point temperatures, by comparison with reference, or standard thermometers (EURAMET (2011)). In fixed point measurements the melting or freezing point of a substance is usually measured. A level of uncertainty in the measurement will always exist. Bell (2001) states that the width of the margin, or interval, and the confidence level, or how sure we are that the 'true value' is within that margin, are the two important factors when quantifying an uncertainty. Measurements were taken with each thermocouple around fixed temperatures to determine the level of uncertainty in the results.

Figures G.1 and G.2 show the calibration of the T-type thermocouples around two points. The figures show the measured temperature for the 16 thermocouples. The upper and lower limits for a satisfactory thermocouple measurement was set as three standerd deviations from the mean. This implies a coverage factor, k, of three and a 99.7 % certainty that the reading lies within the satisfactory level. The limits are shown on the figures.

For each of the measurement points a t-test was conducted to ensure that the measured values accurately present the experimental results. An example calculation that was conducted around the boiling point of water is shown below.

$$t = \frac{\bar{x}_1 - \bar{x}_2}{\sqrt{\frac{{\sigma_1}^2}{n_1} + \frac{{\sigma_2}^2}{n_2}}} = \frac{99,271 - 99,385}{\sqrt{\frac{0{,}0855}{16} + \frac{0{,}0442}{16}}} = 1.267 \tag{G.1}$$

where $\bar{x}_1$ and $\bar{x}_2$ are the means of the two sets of data, ${\sigma_1}^2$ and ${\sigma_2}^2$ are the variances of the two sets and n_1 and n_2 are the number of thermocouples for each set. The resulting $t = 1.267$ was checked in a t-table (Banerjee (1961)), and it is smaller than the t-value of 4.07 that is found at a 15-degrees of freedom and 99 % certainty entry. This means that the difference between the two sets of measured values are not significant.

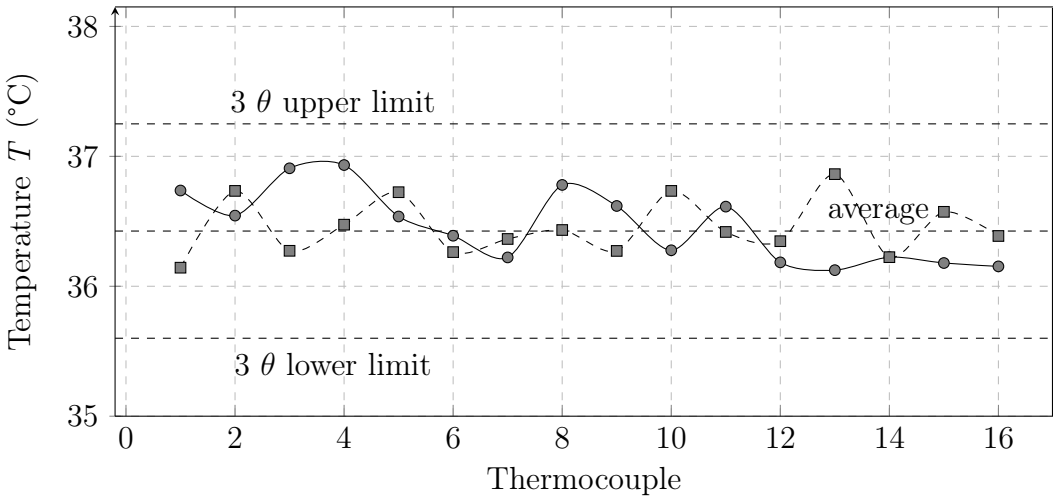

Figure G.1: Thermocouple calibration

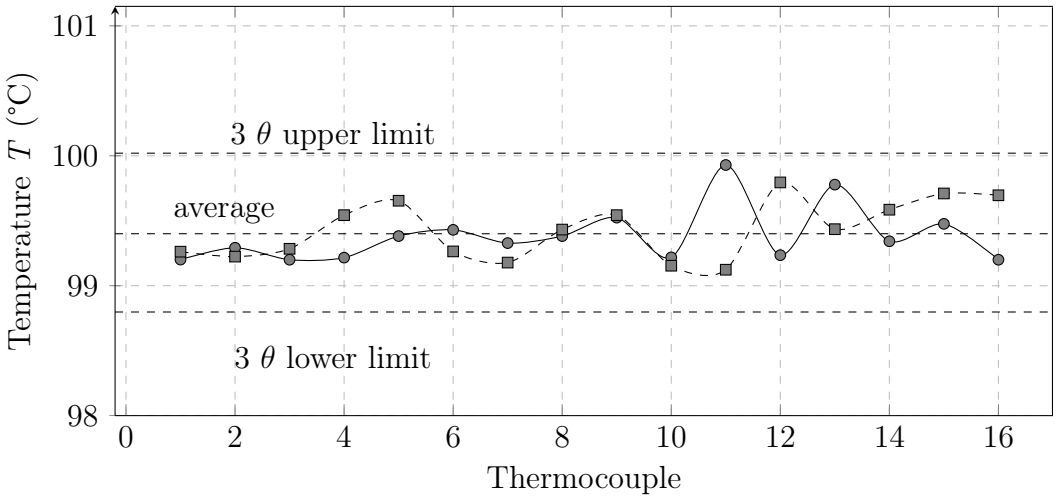

Figure G.2: Thermocouple calibration

Appendix H
Detailed Error Analysis

This appendix contains the derivatives and final calculated arror equations for all model results based on the error analysis in Section 4.5.

H.1 Volumetric Flow Rate

Recalling Equation 4.2 and 4.3 with $G = AV$,

$$\frac{\partial G_e}{\partial V_e} = \frac{G_e}{V_e}$$

$$\frac{\partial G_e}{\partial A_e} = \frac{G_e}{A_e}$$

Thus the final error is

$$\frac{\delta G_e}{G_e} = \sqrt{\left(\frac{\delta V_e}{V_e}\right)^2 + \left(\frac{\delta A_e}{A_e}\right)^2} \tag{H.1}$$

H.2 Temperature

Temperature is simply calculated from the uncertainties presented in Table 4.3. Thus the final error is

$$\frac{\delta T}{T} = \sqrt{\left(\frac{\delta T_{pr}}{T}\right)^2 + \left(\frac{\delta T_{ven}}{T}\right)^2} \tag{H.1}$$

Table H.3 shows the error in temperature measurement at different temperatures.

Table H.1: Error (%) in volumetric flow rate measurement of inlet configurations

		Wind Speed (m/s)			
Configuration	Wet or Dry	0	2.3	3.5	4.8
Open-Ended	Wet	4.29	3.30	3.00	3.21
	Dry	3.00	3.90	4.05	4.14
Dome	Wet	3.54	3.03	3.00	3.00
	Dry	3.00	3.00	3.03	3.15
DSI	Wet	3.90	4.32	5.01	5.43
	Dry	3.00	3.45	3.99	4.47
TFI	Wet	3.60	4.44	5.04	5.34
	Dry	3.01	4.05	4.65	5.04

Table H.2: Error (%) in volumetric flow rate measurement of outlet configurations

		Wind Speed (m/s)			
Configuration	Wet or Dry	0	2.3	3.5	4.8
Open-Ended	Wet	5.70	5.10	4.20	4.02
	Dry	3.00	3.15	3.30	3.72
Dome	Wet	4.65	4.53	4.38	4.05
	Dry	3.00	3.03	3.15	3.60
Whirlybird	Wet	5.55	4.92	4.80	4.95
	Dry	3.00	3.54	3.75	3.81
TFO	Wet	5.64	4.20	3.75	3.36
	Dry	3.00	3.84	4.80	5.10

H.3 Loss Coefficient

Recalling Equation 5.1,

$$k_{ILC} = \frac{2((p_i - p_e) + (z_i - z_e)(\rho_i - \rho_e)g + (\frac{{V_i}^2 - {V_e}^2}{2}) + \sum_{i=1}^{n} k_L \rho_p {V_p}^2)}{\rho_i({V_i}^2)}$$

The derivatives are

Table H.3: Error (%) in temperature measurement of inlet configurations

Configuration	Measurement Location	Wind Speed (m/s)			
		0	2.3	3.5	4.8
Open-Ended	1	3.97	4.40	4.45	3.86
	2	4.53	4.38	4.18	3.91
	3	4.50	4.22	3.94	3.85
	4	4.63	4.09	3.89	3.83
Dome	1	4.20	4.57	3.59	4.60
	2	5.34	5.33	4.98	4.43
	3	5.21	4.42	4.38	4.17
	4	5.26	4.28	4.22	4.02
DSI	1	4.09	3.58	3.51	3.42
	2	5.53	5.24	5.06	4.89
	3	5.39	5.20	5.14	4.94
	4	5.49	5.06	5.18	3.66
TFI	1	4.46	4.22	4.20	4.28
	2	5.42	5.64	5.19	5.31
	3	5.35	5.53	5.33	5.35
	4	5.27	5.55	5.33	5.30

$$\frac{\delta k_{ILC}}{\delta p_i} = \frac{k_{ILC}}{p_i}$$

$$\frac{\delta k_{ILC}}{\delta p_e} = \frac{k_{ILC}}{p_e}$$

$$\frac{\delta k_{ILC}}{\delta \rho_e} = \frac{k_{ILC}}{\rho_e}$$

$$\frac{\delta k_{ILC}}{\delta V_e} = \frac{2k_{ILC}}{V_e}$$

$$\frac{\delta k_{ILC}}{\delta \rho_{p1}} = \frac{k_{ILC}}{\rho_{p1}}$$

$$\frac{\delta k_{ILC}}{\delta V_{p1}} = \frac{2k_{ILC}}{V_{p1}}$$

$$\frac{\delta k_{ILC}}{\delta \rho_{p2}} = \frac{k_{ILC}}{\rho_{p2}}$$

Table H.4: Error (%) in temperature measurement of outlet configurations

Configuration	Measurement Location	Wind Speed (m/s)			
		0	2.3	3.5	4.8
Open-Ended	1	3.54	4.92	4.95	4.39
	2	4.50	4.23	3.80	3.30
	3	4.58	4.23	3.83	3.32
	4	5.73	5.61	5.24	5.43
Dome	1	4.40	4.12	3.99	3.94
	2	5.00	3.92	4.53	4.43
	3	5.27	5.04	5.09	4.58
	4	5.68	5.93	5.91	5.92
Whirlybird	1	4.30	4.10	4.03	4.09
	2	4.21	4.13	4.01	4.09
	3	4.33	4.13	4.04	4.11
	4	4.94	4.66	4.36	3.87
TFO	1	4.48	4.05	3.87	3.75
	2	4.51	4.13	3.73	3.54
	3	4.58	4.11	3.66	3.39
	4	5.03	4.66	4.60	4.29

$$\frac{\delta k_{ILC}}{\delta V_{p2}} = \frac{2k_{ILC}}{V_{p2}}$$

$$\frac{\delta k_{ILC}}{\delta \rho_i} = -\frac{k_{ILC}}{2\rho_i}$$

$$\frac{\delta k_{ILC}}{\delta V_i} = -\frac{k_{ILC}}{4V_i}$$

Thus the final error is

$$\frac{\delta k_{ILC}}{k_{ILC}} = \sqrt{\left(\frac{\delta p_i}{p_i}\right)^2 + \left(\frac{\delta p_e}{p_e}\right)^2 + \frac{1}{4}\left(\frac{\delta \rho_i}{\rho_i}\right)^2 + \left(\frac{\delta \rho_e}{\rho_e}\right)^2 + \frac{1}{16}\left(\frac{\delta V_i}{V_i}\right)^2 + 4\left(\frac{\delta V_e}{V_e}\right)^2 + \left(\frac{\delta \rho_{p1}}{\rho_{p1}}\right)^2 + \left(\frac{\delta \rho_{p2}}{\rho_{p2}}\right)^2 + 4\left(\frac{\delta V_{p1}}{V_{p1}}\right)^2 + 4\left(\frac{\delta V_{p2}}{V_{p2}}\right)^2} \quad \text{(H.1)}$$

Table H.5: Error (%) of inlet loss coefficient for inlet configurations on wet PDEC

Wind Speed	0 m/s	2.3 m/s	3.5 m/s	4.8m/s
Open-ended	17.70	38.98	66.67	N/A
Dome	27.68	82.89	N/A	N/A
DSI	21.19	17.98	15.49	14.68
TFI	26.68	17.39	15.44	14.85

Table H.6: Error (%) of inlet loss coefficient for inlet configurations on dry PDEC

Wind Speed	0 m/s	2.3 m/s	3.5 m/s	4.8m/s
DSI	N/A	17.98	15.49	14.68
TFI	N/A	17.39	15.44	14.85

Table H.7: Error (%) of outlet loss coefficient for outlet configurations on hot solar chimney

Wind Speed	0 m/s	2.3 m/s	3.5 m/s	4.8m/s
Open-ended	15.19	16.87	22.08	25.11
Dome	18.48	19.11	20.35	24.01
Whirlybird	15.52	17.43	18.03	17.29
TFO	15.31	22.08	30.85	60.17

Table H.8: Error (%) of outlet loss coefficient for *Whirlybird* on hot solar chimney

Wind Speed	0 m/s	2.3 m/s	3.5 m/s	4.8m/s
Whirlybird	N/A	38.36	29.97	28.34

The greatest errors were found in the loss coefficient calculations.

Appendix I
SCAPDEC System in South Africa

Climatic conditions in cities in South Africa vary with seasonal change. Cities experience different climatic conditions in part to its location relative to land and water mass, and its height above sea level. A city that is high above sea level, like Johannesburg, will have a lower atmospheric pressure than a city that is situated next to the sea, like Cape Town. In a PDEC shaft evaporation happens faster at a lower atmospheric pressure. This is because the surface of evaporation experiences less exertion keeping the molecules from launching. Evaporation is further dependent on ambient temperature and relative humidity. If the relative humidity is high the air is closer to saturation and cannot take on much more water vapour.

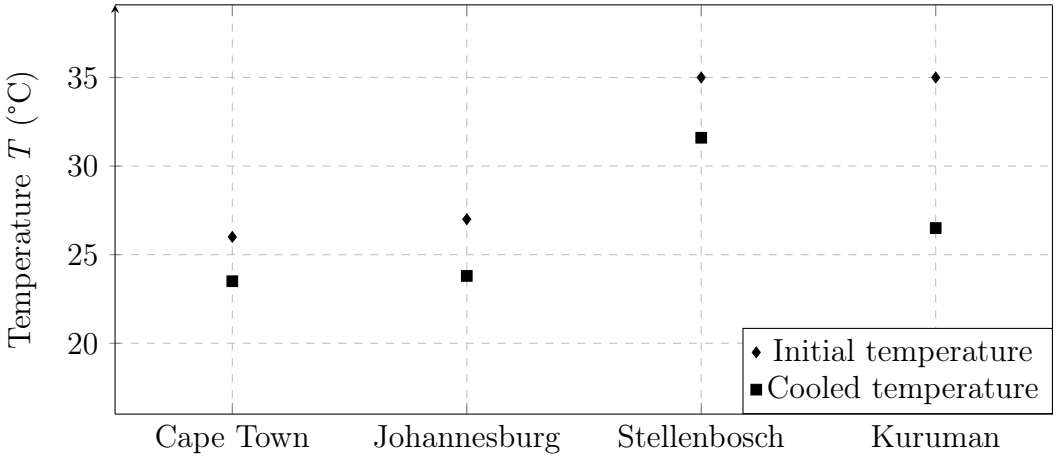

Figure I.1: Temperature comparison of some South African cities and towns with evaporative cartridge model [L = 1 m, 5 concentric pads]

Figures I.1 to I.3 show the temperature, volumetric flow rate and relative humidity expected from the evaporative cartridge built in Section 4, for some cities and towns. The results show, where applicable, the initial and cooled

conditions as theorised with the one-dimensional model. The initial conditions were taken as an average summer day (Kruger and Shongwe (2004)).

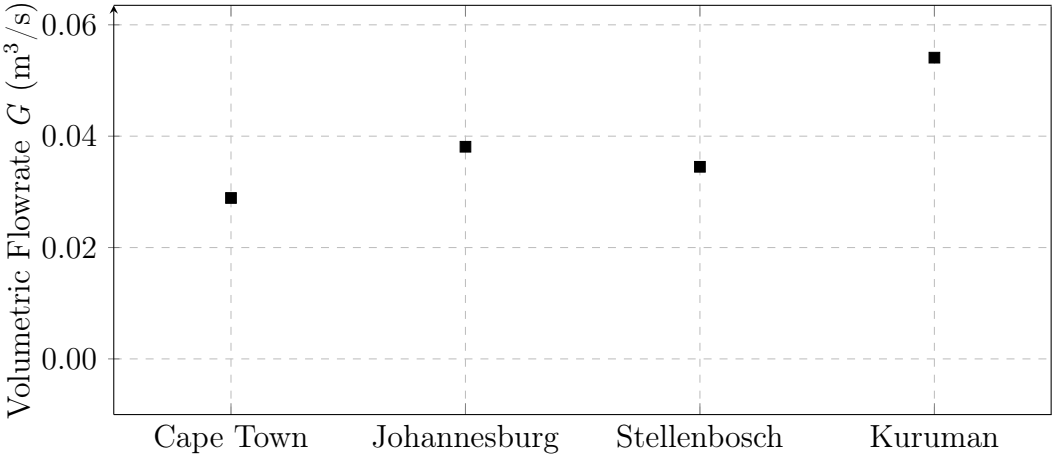

Figure I.2: Volumetric flow rate comparison of South African cities and towns with evaporative cartridge model [L = 1 m, 5 concentric pads]

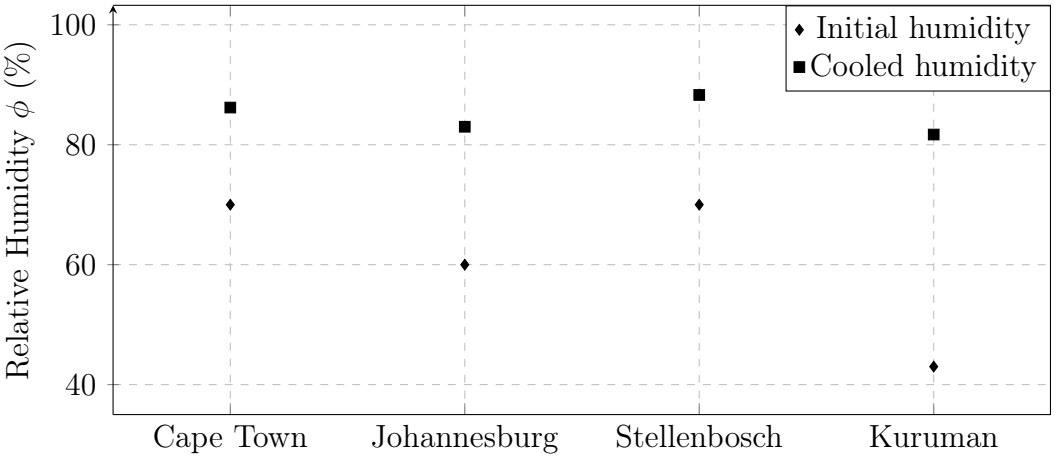

Figure I.3: Humidity comparison of South African cities and towns with evaporative cartridge model [L = 1 m, 5 concentric pads]

Appendix J

Velocity Profile in PDEC and Solar Chimney

A velocity profile shows the magnitude of air velocity at a certain point in tube or pipe flow. A flow vector with magnitude and direction perpendicular to the pipe inlet and outlet is therefore taken as the velocity profile.

J.1 Experimental and Theoretical Velocity Profile in PDEC

Figure J.1 shows the experimentally determined and theoretical CFD velocity profile versus the one-seventh law as a function of radius for the Open-ended inlet configuration.

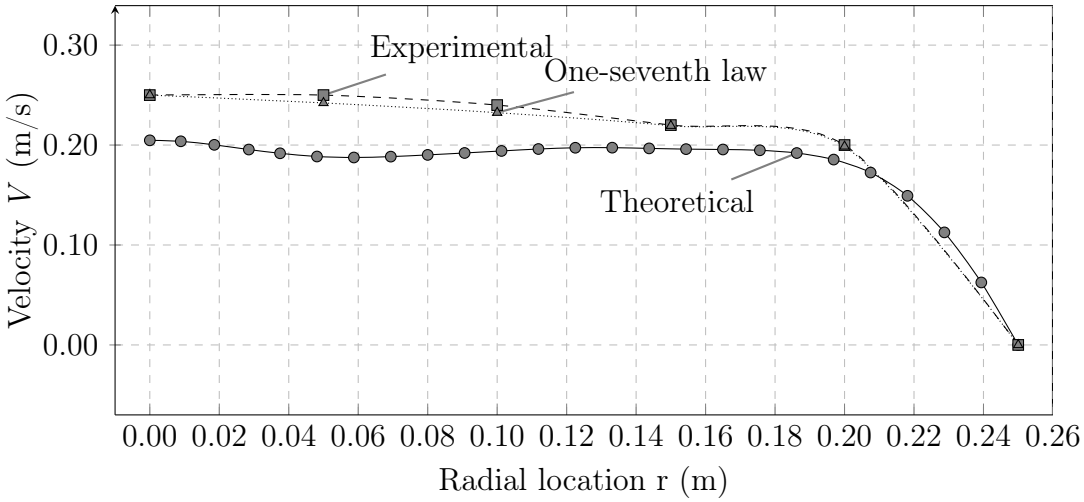

Figure J.1: Velocity profile in wet PDEC shaft at V_w=0 m/s for Open-ended inlet [T_{amb} = 27°C, ϕ = 50 %]

J.2 Velocity profiles for PDEC

The profiles for different wind speeds for a dry and wet PDEC, for the DSI and TFI configuration, is shown in Figures J.2 to J.5. A positive velocity corresponds with air flowing down the PDEC shaft.

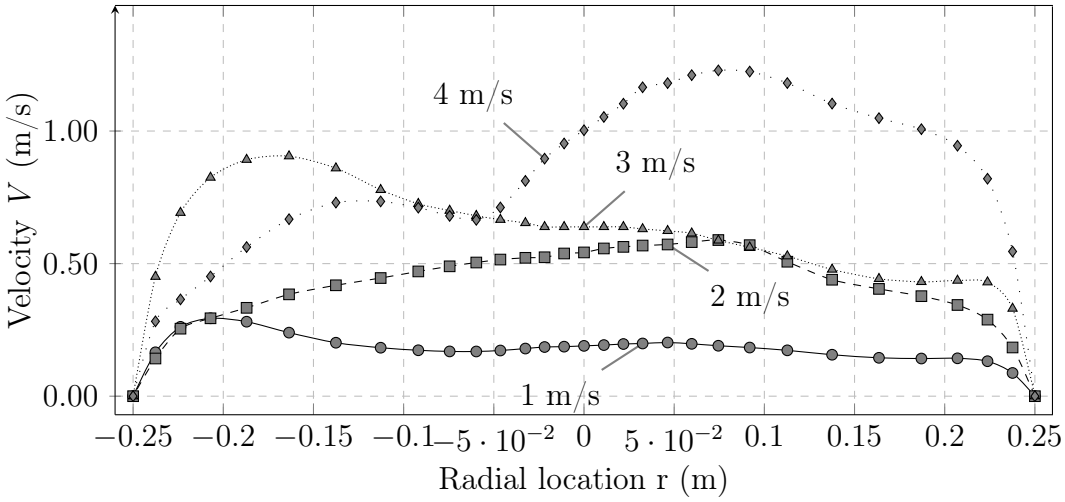

Figure J.2: Velocity profile in dry PDEC shaft at different wind speeds for DSI inlet configuration [T_{amb} = 27°C, ϕ = 45.8%]

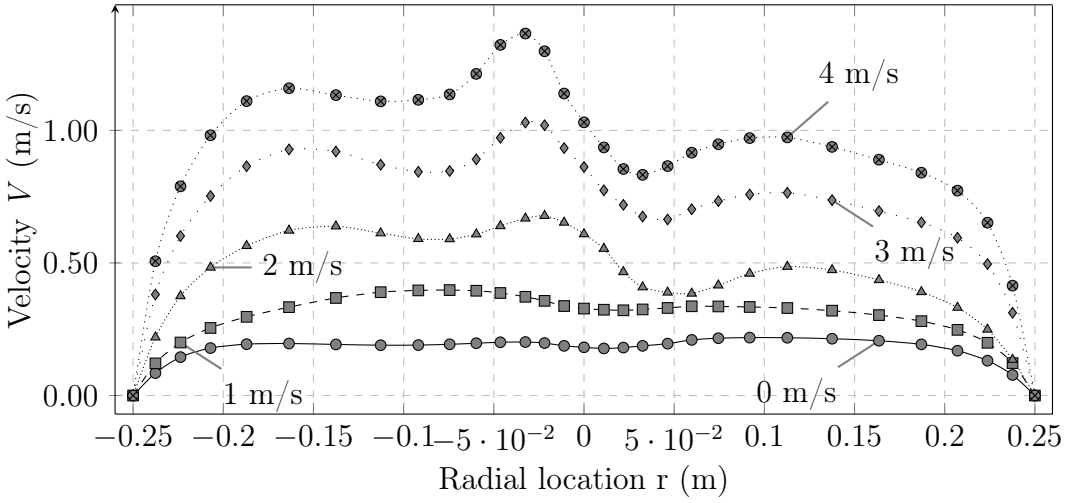

Figure J.3: Velocity profile in wet PDEC shaft at different wind speeds for DSI inlet configuration [T_{amb} = 27°C, ϕ = 45.8%]

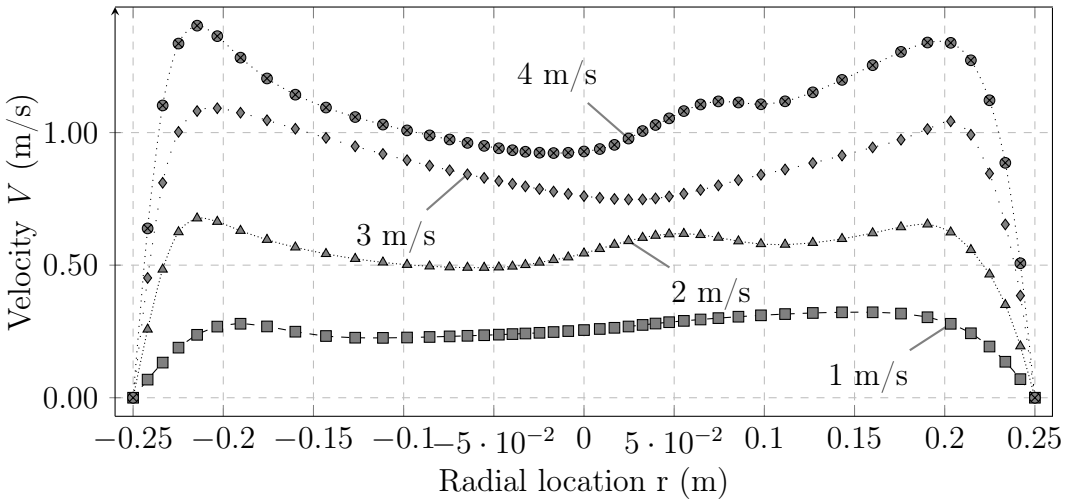

Figure J.4: Velocity profile in dry PDEC shaft at different wind speeds for TFI inlet configuration [T_{amb} = 27°C, ϕ = 45.8%]

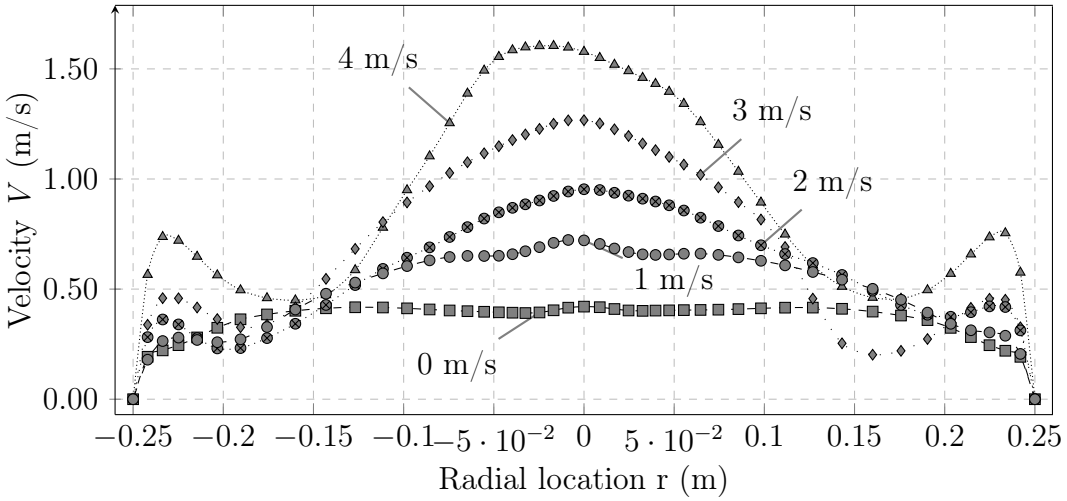

Figure J.5: Velocity profile in wet PDEC shaft at different wind speeds for TFI inlet configuration [T_{amb} = 27°C, ϕ = 45.8%]

J.3 Velocity profiles for solar chimney

The velocity profiles for different wind speeds for a solar chimney with an Open-ended outlet is shown in Figures J.6. The Open-ended outlet is investigated to determine the effects that wind has on an outlet if no configuration is installed. A positive velocity is taken as air flowing up the solar chimney.

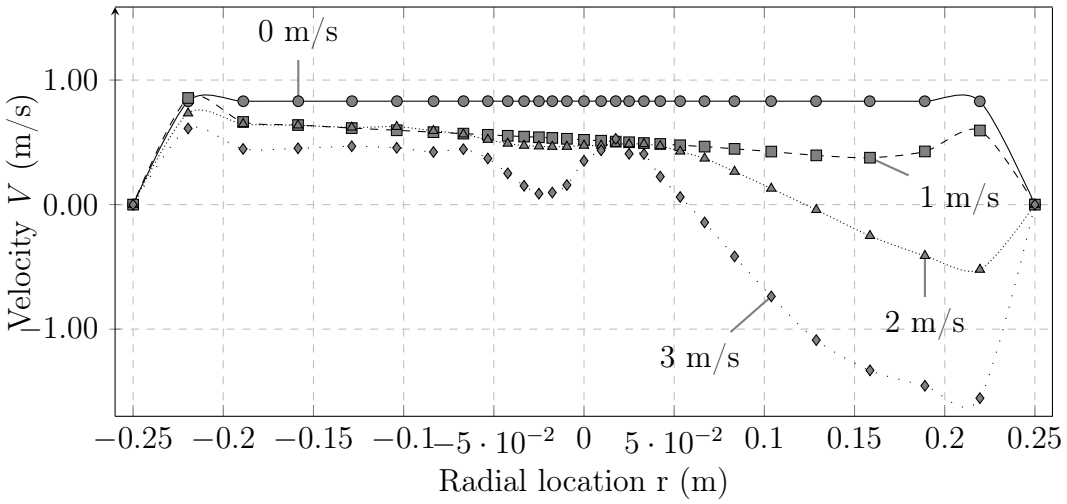

Figure J.6: Velocity profile in solar chimney at different wind speeds for Open ended outlet configuration [T_{amb} = 16°C, $\phi = 50\%$]

Figures J.7 to J.10 show the velocity profiles of the TFO and *Whirlybird* configurations. The velocity profiles for the Dome outlet is not shown, as the profiles followed similar flow patterns as the Open-ended outlet.

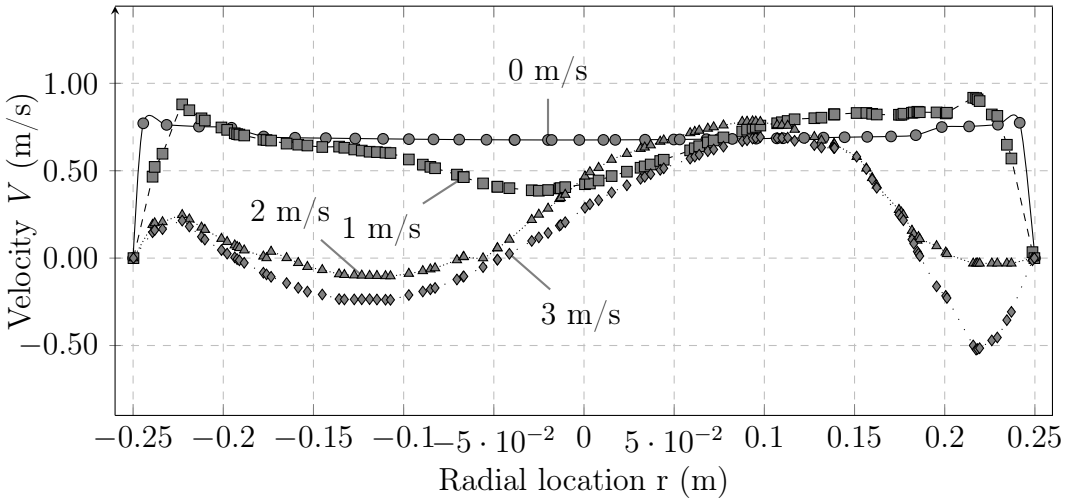

Figure J.7: Velocity profile in hot solar chimney at different wind speeds for TFO configuration [T_{amb} = 16°C, $\phi = 50\%$]

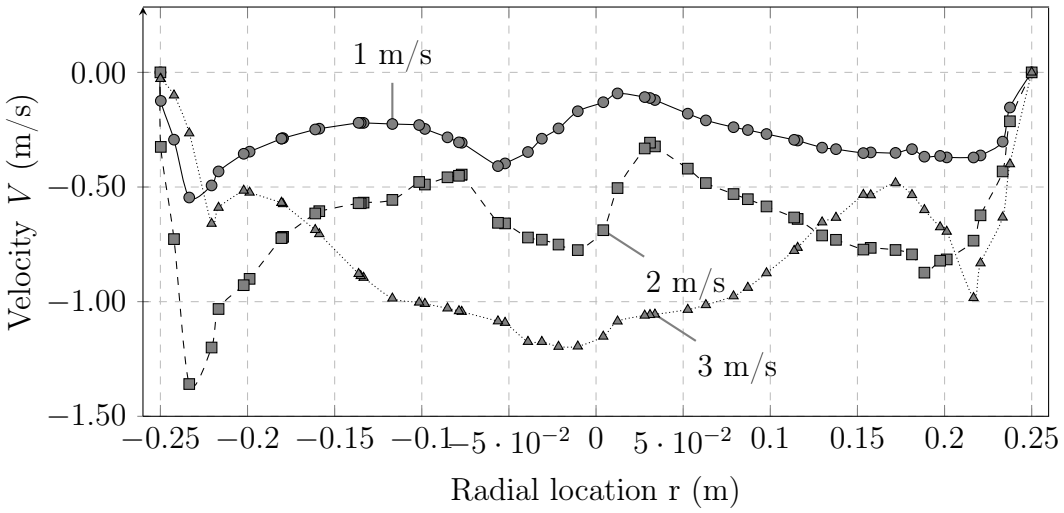

Figure J.8: Velocity profile in cold solar chimney at different wind speeds for TFO configuration [T_{amb} = 16°C, ϕ = 50%]

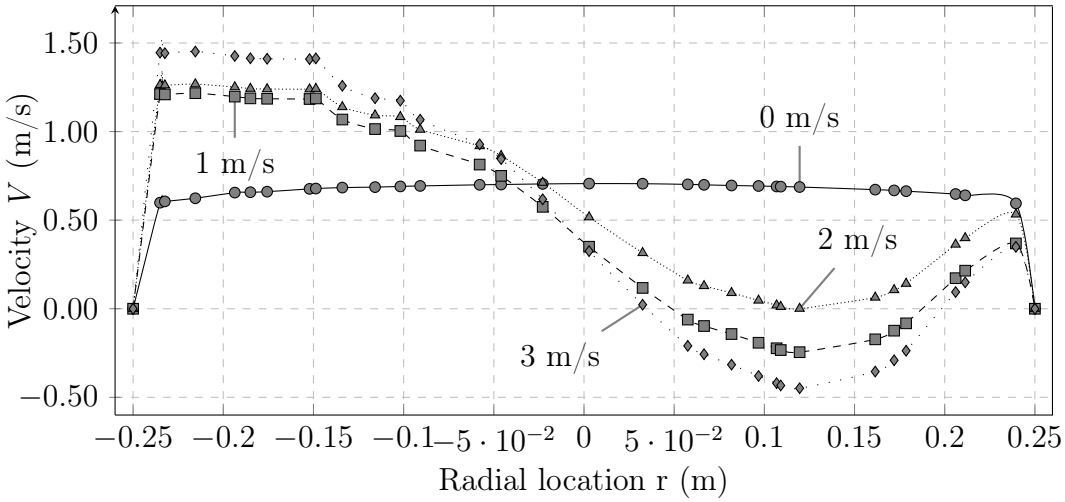

Figure J.9: Velocity profile in hot solar chimney at different wind speeds for *Whirlybird* configuration [T_{amb} = 16°C, ϕ = 50%]

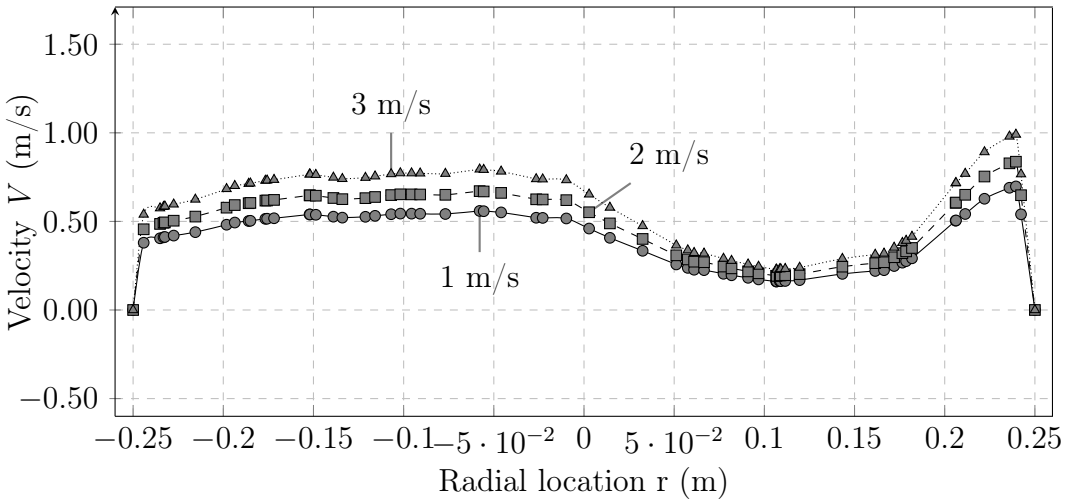

Figure J.10: Velocity profile in cold solar chimney at different wind speeds for *Whirlybird* configuration [T_{amb} = 16°C, $\phi = 50\%$]

Appendix K

Theoretical Velocity and Temperature Comparison in Still and Windy Conditions

A comparison of the CFD velocity and temperature distributions for still and windy conditions with a hot solar chimney and Open-ended outlet are shown in Figure K.1. The figures show the variable contours on a vertical two-dimensional plane in the three-dimensional flow field. As discussed in Section 3.3, the flow field consists of a PDEC shaft or solar chimney and an overhead domain were wind is modelled. In the figure wind blows from right to left over the solar chimney. From the velocity contours it is evident that for V_w=0 m/s the hot air from the solar chimney was able to escape freely at the top of the chimney. The contours at V_w=3 m/s shows that air has to escape at the side furthest from the incoming wind. The temperature contours for V_w=0 m/s and V_w=3 m/s shows that the highest temperature in the chimney is 297 K and 302 K respectively. It is therefore evident that the volume flow rate through the chimney is less at higher wind speeds and the air spends more time in the chimney where heat is added.

Figure K.2 shows a comparison of the CFD temperature distribution for still and windy conditions for a TFO configuration on a hot solar chimney. In the figure wind blows from right to left over the solar chimney. It is evident that the hot air rising in the solar chimney struggles to escape at the chimney top with increasing wind speed.

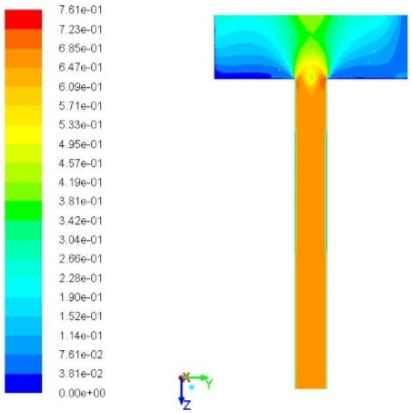

(a) Velocity contours at V_w=0 m/s

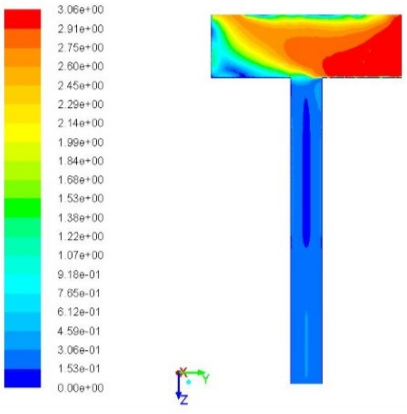

(b) Velocity contours at V_w=3 m/s

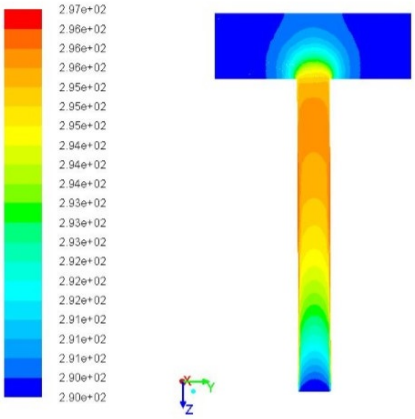

(c) Temperature contours at V_w=0 m/s

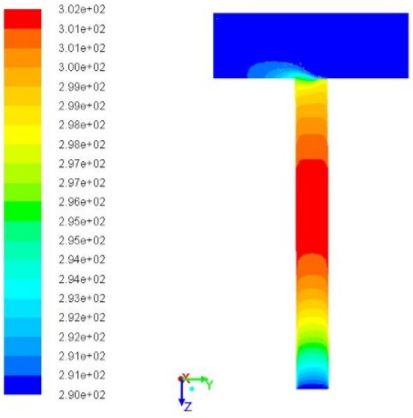

(d) Temperature contours at V_w=3 m/s

Figure K.1: Comparison of CFD velocity and temperature contours at still (V_w=0 m/s) and windy (V_w=3 m/s) conditions in a hot solar chimney [T_{amb} = 17°C]

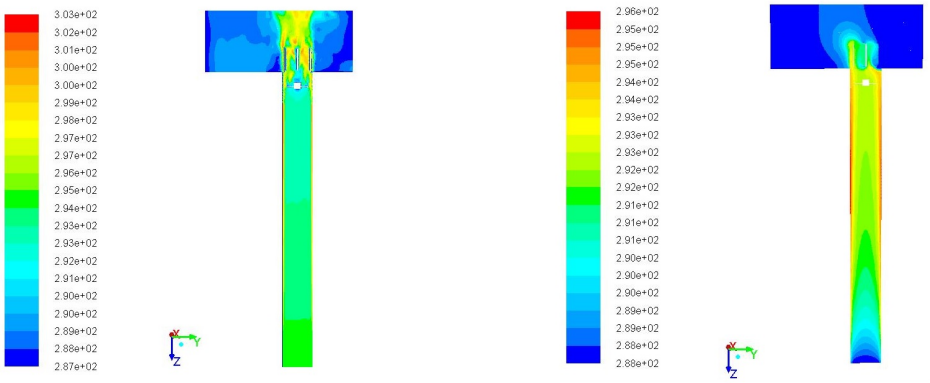

(a) Temperature contours at V_w=0 m/s (b) Temperature contours at V_w=2.8 m/s

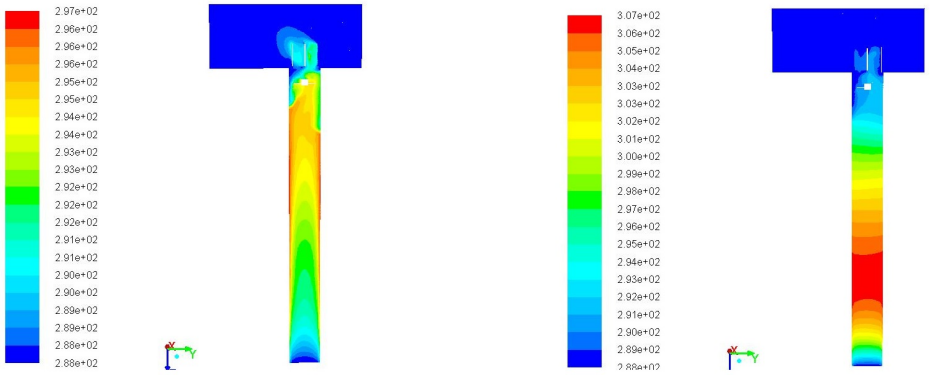

(c) Temperature contours at V_w=3.5 m/s(d) Temperature contours at V_w=4.8 m/s

Figure K.2: Comparison of CFD temperature contours at still (V_w=0 m/s) and windy (V_w=2.8 m/s, V_w=3.5 m/s and V_w=4.8 m/s) conditions for the TFO configuration and a hot solar chimney [T_{amb} = 15°C]

List of References

Allard, F. and Ghiaus, C. (2005). Natural ventilation in the urban environment. *Earthscan*.

Axley, J.W. (2001). Application of natural ventilation for us commercial buildings–climate suitability, design strategies & methods, modeling studies. *Prepared for US DOE & NIST*.

Bahrami, M. (2009). *Fluid Mechanics, Fluid statics*. Ph.D. thesis, Simon Fraser University.

Banerjee, S. (1961). On confidence interval for two-means problem based on separate estimates of variances and tabulated values of t-table. *Sankhyā: The Indian Journal of Statistics, Series A*, pp. 359–378.

Batty, J. and Folkman, S. (1983*a*). *Food Engineering Fundamentals*. Wiley: New York.

Batty, J. and Folkman, S. (1983*b*). *Food Engineering Fundamentals*. Wiley: New York.

Bell, S. (2001). *A beginner's guide to uncertainty of measurement*. National Physical Laboratory Teddington, Middlesex.

Botha, D. (2010). *Solar Chimney Augmented Passive Downdraught Evaporative Cooling System*. Master's thesis, Stellenbosch University.

Cengel, Y. (2006). *Heat and mass transfer: A practical approach*. McGraw -Hill: New York.

Chalfoun, N. (1997). Design and application of natural down-draft evaporative cooling devices. In: *PROCEEDINGS OF THE NATIONAL PASSIVE SOLAR CONFERENCE*, vol. 22, pp. 143–148. AMERICAN SOLAR ENERGY SOCIETY INC.

Chen, N.H. (1979). An explicit equation for friction factor in pipe. *Industrial & Engineering Chemistry Fundamentals*, vol. 18, no. 3, pp. 296–297.

Cunningham, W.A., Mignon, G. and Thompson, T.L. (1987). Establish feasibility for providing passive cooling with solar updraft and evaporative downdraft chimneys. Tech. Rep., Arizona Univ., Tucson, AZ (United States). Environmental Research Lab.

dos S Bernardes, M., Voß, A. and Weinrebe, G. (2003). Thermal and technical analyses of solar chimneys. *Solar Energy*, vol. 75, no. 6, pp. 511–524.

Dou, H.-S., Khoo, B.C., and Tsai, H.M. (2005). Critical condition for flow transition in a full- developed annulus flow. Tech. Rep., Department of Mechanical Engineering and Temasek Laboratory, National University of Singapore,, Singapore 119260.

Elzaidabi, A. (2008 September). *Low Energy, Wind Catcher Assited Indirect - Evaporative Cooling System for Building Applications*. Ph.D. thesis, University of Nottingham.

Emmerich, S.J., Dols, W.S. and Axley, J.W. (2001). *Natural ventilation review and plan for design and analysis tools*. US Department of Commerce, Technology Administration, National Institute of Standards and Technology.

Etheridge, D. (2011). *Natural ventilation of buildings: theory, measurement and design*. John Wiley & Sons.

EURAMET (2011). Calibration of thermocouples. *Calibration Guid, EURAMET cg-8 version 2.1*.

Fluent, A. (2010). 12.1 user manual. *ANSYS Inc*.

Fortran (2014). Fortran 90. `http://www.fortran.org/`. Accessed: 2012-09-15.

Gauché, P. (2010). Presentation on prerequisites to large scale rollout of csp in southern africa: models, plants and resources. *Solar Thermal Energy Research Group, University of Stellenbosch*.

Gontikaki, M., Trcka, M., Hensen, J. and Hoes, P. (2010). Optimization of a solar chimney design to enhance natural ventilation in a multi-storey office building.

Gullman, S. (2010). *Development of evaporation models for CFD*. Master's thesis, Chalmers University of Technology.

Hagemann, K. (2008 July). *Mesoscale Wind Atlas of South Africa*. Ph.D. thesis, University of Cape Town, Department of Environmental and Geographical Science.

Hanley, A., Sauer, H. and Sherman, M. (1995). Addendum to thermal environmental conditions for human occupancy. *ANSI/ASHRAE 55a-1995*, pp. 1–5.

Herbst, L. and Lalk, J. (2014). A case study of climate variability effects on wind resources in south africa. *Journal of Energy in Southern Africa*, vol. 25, no. 3, pp. 02–10.

Holm, D. and Engelbrecht, F. (2005). Practical choice of thermal comfort scale and range in naturally ventilated buildings in south africa: technical paper. *Journal of the South African Institution of Civil Engineering= Joernaal van die Suid-Afrikaanse Instituut van Siviele Ingenieurswese*, vol. 47, no. 2, pp. p–9.

Ibrahim, E., Shao, L. and Riffat, S.B. (2003). Performance of porous ceramic evaporators for building cooling application. *Energy and Buildings*, vol. 35, no. 9, pp. 941–949.

Iqbal, M. (1983). *An introduction to solar radiation*. Elsevier.

Kruger, A. and Shongwe, S. (2004). Temperature trends in south africa: 1960–2003. *International Journal of Climatology*, vol. 24, no. 15, pp. 1929–1945.

Lagoudas, D. and Haisler, W. (2002). Introduction to conservation principles and applications in continuum mechanics. Aerospace Engineering Department Texas AM University.

Larson, T. (2006 June). *Natural Ventilation Driven by Wind and Temperature Difference*. Ph.D. thesis, Aalborg University, Department of Civil Engineering, Group of Architectural Engineers.

le Grange, F. (2009). *Mathematical modelling and verification of a passive downdraught evaporative cooling tower*. Master's thesis, Stellenbosch University.

Li, Z. (2005). Cfd simulations for water evaporation and airflow movement in swimming baths. *VENTInet*, , no. 14, pp. 10–11.

Luding, S. (2004). Molecular dynamics simulations of granular materials. In: Hinrichsen, H. and Wolf, D. (eds.), *The Physics of Granular Media*, pp. 299–324. Wiley-VCH, Weinheim.

Luo, Q. (2006). *Investigation on air-conditioning energy consumption of a typical building complex*. Ph.D. thesis, Nanhua University: China.

Martinez, D.F. (2000). Thermal simulation of passive downdraught evaporative cooling (pdec) in non-domestic buildings.

O Sullivan, C.T. (1990). Newton's law of cooling-a critical assessment. *Am. J. Phys*, vol. 58, no. 12, pp. 956–960.

Pearlmutter, D., Erel, E., Etzion, Y. and Meir, I. (1996). Refining the use of evaporation in an experimental down-draft cool tower. *Energy and Building*, vol. 23, pp. 191–197.

Recktenwald, G. (2002 April). Fully-developed flow in a pipe: A cfd solution. Tech. Rep., Mechanical Engineering Department,Portland State University, Portland, OR, 97201.

Sreenivas, K. and Prasad, A.K. (2000). Vortex-dynamics model for entrainment in jets and plumes. *Physics of Fluids (1994-present)*, vol. 12, no. 8, pp. 2101–2107.

Sundell, J. (2002). *Sustainable built environment. Vol. 1. Health and Comfort in Buildings*. Ph.D. thesis, Technical university of Denmark: Lyngby.

Swiegers, J. (2012). *Inlet and Outlet Shape Optimisation of Natural Circulation Building Ventilation System*. Master's thesis, Stellenbosch University.

Swiegers, J. (2014). *Provisional Patent, Ventil[l]ation System and Components thereof, Ref: P2839ZA00*. Stellenbosch University.

White, F. (2005). *Fluid Mechanics, 5th ed.* McGraw -Hill: New York.

WHO (2009). *Dengue: guidelines for diagnosis, treatment, prevention and control:World Health Organization and Special Programme for Research and Training in Tropical Diseases and World Health Organization. Department of Control of Neglected Tropical Diseases and World Health Organization. Epidemic and Pandemic Alert*. World Health Organization.

Wong, H. (1997). *Handbook of essential formulae and data on Heat Transfer for Engineers*. Longman: New York.

Yıldırım, G. (2008). Determining operating inlet pressure head incorporating uniformity parameters for multioutlet plastic pipelines. *Journal of irrigation and drainage engineering*, vol. 134, no. 3, pp. 341–348.

Yokota, Y. and Kawabata, N. (2012). A study of the chimney natural exhaust effect for road tunnel fires. *Central Nippon Highway Engineering Tokyo Company Limeted*, pp. 82 – 89.